Split ring resonators : flexible and tunable metamaterials, fano coupling and their applications in sensing

Wen, Xinglin

2016

Wen, X. (2016). Split ring resonators : flexible and tunable metamaterials, fano coupling and their applications in sensing. Doctoral thesis, Nanyang Technological University, Singapore.

https://hdl.handle.net/10356/65937

https://doi.org/10.32657/10356/65937

SPLIT RING RESONATORS: FLEXIBLE AND TUNABLE METAMATERIALS, FANO COUPLING AND THEIR APPLICATIONS IN SENSING

Wen Xinglin

SCHOOL OF PHYSICAL AND MATHEMATICAL SCIENCES

2015

SPLIT RING RESONATORS: FLEXIBLE AND TUNABLE METAMATERIALS, FANO COUPLING AND THEIR APPLICATIONS IN SENSING

Wen Xinglin

School of Physical and Mathematical Sciences

A thesis submitted to the Nanyang Technological University
in fulfillment of the requirement for the degree of
Doctor of Philosophy

2015

Acknowledgments

I would like to take this opportunity to express my deep gratitude to the people who have helped me during my PhD study. The dissertation would have been impossible to complete without their help.

First of all, I want to specially acknowledge my supervisor professor Xiong Qihua for his abundant support and encouragement during my PhD training. I benefited a lot from his great passion and precise attitude to research. His expertise, experience and patient guidance contributed a lot to improve my research abilities.

I would like to express special thanks to my co-supervisor Dr. Wang Shijie. His expertise on thin film growth expedited my project progress greatly. His support on facilities and sample preparation are greatly appreciated.

Thanks to Dr. Zhang Qing for her fruitful discussions and guidance in experiment. She gave me a lot of support on experiment design and theoretical discussions. Her willingness to assist in any moment is greatly appreciated. Thanks to Dr. Li Guangyuan for the theoretical calculations on electromagnetic field. Appreciations to Dr. Zhang Jun and Lu Xin for their help on Raman spectroscopy.

Furthermore, I would like to express my appreciation to the group members for their useful suggestions, discussions and encouragement. They are professor Xu Xinlong, Dr. Li Dehui, Dr. Peng Bo, Dr. Zhou Yong, Dr. Cao Cuong, Dr. Xing jun, Dr. Yu Huakang, Dr. Zhang Chaohua, Dr. Xu Weigao, Dr. Zhao Yanyuan, Chen Renjie, Li Zhenpeng, Zhang Chiyuan, Yuan Yanwen, Zhang Lulu, Liu yang and M. Iqbal Bakti Utama.

Finally, I would like express my deepest love and gratitude to my beloved family. They always gave me unconditional support at any moment. This thesis is dedicated to them.

Abstract

Split ring resonators (SRRs) are widely used as plasmonics and metamaterials components because they have both electric and magnetic responses. The electric property arises from the dipole moment excited by the incident light while the magnetic mode emerges from the circulating current induced along the ring. In this dissertation, by utilizing the SRRs as the basic component, we developed transparent and flexible metamaterials by integrating the SRRs to the polymer. We also demonstrated the tunability of the optical response by combining the SRRs and the phase change material. In addition, the magnetic mode of SRRs was utilized to couple to the electric mode to generate the magnetic mode based Fano resonance, which is distinguished from the conventional electric mode based Fano resonance.

Attributing metamaterials to a flexible substrate can provide the advantages such as transparency, deformability, light-weight and bio-compatibility. In this dissertation, free-standing and transparent metamaterials were fabricated by a nickel sacrificial layer assisted transfer method. The SRRs array can be transferred from a rigid substrate to polydimethylsiloxane (PDMS) without any damage. Both the structure and the optical properties of SRRs array can be maintained after transferring to the PDMS. A convenient surface enhanced Raman scattering (SERS) strategy was demonstrated by covering the PDMS-meta onto the surface with the analytes residing on, which can separate the SERS substrate from the analytes. More importantly, the free standing metamaterials were utilized to investigate the coupling between nano structures and metal film.

Integration of SRR metamaterials to phase change materials can achieve the tunability of the optical response. The properties of metamaterials are fixed once the fabrication completed, it is desired to accomplish active metamaterials to satisfy various applications. By utilizing the phase change property of vanadium dioxide (VO_2), we demonstrated that both the electric and magnetic responses of SRR can be tuned within near infrared range. We can control the resonance wavelength in real

time by controlling the temperature of VO_2. In addition, the tunable resonance of SRR was used to construct a tunable SERS device, which can engineer the SERS intensity by controlling the resonance wavelength.

Another phase change material $Ge_2Sb_2Te_5$ (GST) was utilized to couple to plasmonic structures to achieve tunable perfect absorber. In the conventional Fabry-Pérot (FP) cavity, the minimum thickness required to achieve interference condition should be a quarter wavelength. In this thesis, we demonstrated that an ultrathin lossy phase change film can sustain the interference effects and an unity absorption is attainable. The reflectivity difference of the amorphous and crystalline GST thin films can gave a high optical contrast ratio, highlighting the potential in the applications of optical switch and data storage. Furthermore, a plasmonic structure was added to make the absorption band broader.

The coupling inside the split ring/disk cavity was investigated to reveal the magnetic mode based Fano resonance. Previously the Fano resonance mainly focused on the electric modes interaction. However, the interaction between a magnetic mode and an electric mode also can produce a Fano resonance. The magnetic mode based Fano resonance can generate high magnetism at the resonance wavelength. Herein, we revealed that the quadrupole and octupole magnetic modes of SRR can be coupled to electric dipole to generate a Fano resonance. In addition, the Fano spectra shape and resonance wavelength can be adjusted by changing the disk diameter and the split ring angle. The magnetic mode based Fano resonance was also demonstrated to be promising in the chemical and biological sensing.

Table of Contents

List of Tables

List of Figures

Citations to published work

Majority of Chapter 3 appears as

"Transparent free-standing metamaterials and their applications in surface-enhanced Raman scattering". **X.L. Wen**, G.Y. Li, J. Zhang, Q. Zhang, B. Peng, L.M. Wong, S. Wang and Q.H. Xiong. ***Nanoscale***, 6, 132-139 (2014)

Majority of Chapter 4 appears as

"Near-infrared active metamaterials and their applications in tunable surface-enhanced Raman scattering". **X.L. Wen**, Q. Zhang, J.W. Chai, L.M. Wong, S. Wang, and Q.H Xiong. ***Optics express****,* 22, 2989-2995 (2014)

Majority of Chapter 5 appears as

"Multiple Magnetic Mode-Based Fano Resonance in Split-Ring Resonator/Disk Nanocavities". Q. Zhang, **X.L. Wen**, G.Y. Li, Q.F. Ruan, J.F. Wang, and Q.H. Xiong. ***ACS Nano***, 7, 11071–11078 (2013)

Majority of Chapter 6 appears as

"A large scale perfect absorber and optical switch based on phase change material ($Ge_2Sb_2Te_5$) thin film". **X.L. Wen** and Q.H. Xiong. ***Submitted***

Chapter 1 Introduction

1.1 Plasmonics

Plasmon can be treated as a quasiparticle resulted from the quantization of the plasma oscillations, reminiscent of phonon which is a quasiparticle quantized from the lattice vibration of a crystal. Within a metal, the mobile carriers are conduction electrons, usually plasmon refers to the collective oscillation of the conduction electrons. The coupling of plasmon and photon can generate another quasiparticle termed as polariton.[1] Surface plasmon polariton (SPP) is the electron density wave propagating along the interface between metal and dielectric. Surface plasmon polariton is generated under certain circumstances, in which the external electromagnetic waves resonantly couple with the conduction electrons of the metal surface. Surface plasmon resonance (SPR) is the coherent oscillation of the surface electrons on the interface between the metal and dielectric.[2, 3] Apart from the propagating plasmon, localized surface plasmon resonance has attracted tremendous attention. The plasmon is never propagating as the dimension of metal particle is much smaller than the excitation wavelength, instead, the electron oscillation will be localized within a very small regime around the particle surface.[4-6] More and more understanding of surface plasmon has been gained with the development of the theoretical treatment of the surface plasmon and electromagnetic field simulation method. In addition, nanofabrication methods have been developed rapidly over last decades, with delicately controlled nanostructures with various size, shape and dielectric media. Benefiting from the huge theoretical and experimental progress, a new discipline termed “Plasmonics” started emerging from 1980s and the research on plasmonic exploded in last 20 years.[7] In principle, plasmonics is a new research area to study the plasmon related light-matter interaction. Plasmonics will explore the issues regarding the generation, propagation, detection of plasmon waves, also it will deal with the electromagnetic field confinement, enhancement and manipulation.

In fact, the observation of plasmonics phenomenon can be dated back to the fourth century A.D., one impressive example is the Lycurgus cup which was a Roman goblet presenting different color when view it from reflected light or transmitted light due to the excitation of plasmonic resonance of the metallic particles suspended inside the cup matrix. When the plasmon of metallic particles is in resonant with the incidence light, it will absorb and scatter short wavelength light of the visible spectrum, consequently observers perceive green color when viewing from reflected light while red viewing from the transmitted light. Humankind in that time lived without modern science could make a magic goblet like that but were unable to provide an understanding and explanation of its origin. Over the last century, scientists have gained deeper and deeper insight of the behavior of both bulk metal and metallic particles by applying the classic electromagnetic theory. Now we understand that most metals reflect all the visible light because its intrinsic plasmon frequency is higher than visible light, while for copper and gold, they will absorb part of the visible light due to the presence of the transition band.

As we know, metal plays marginal role in classical optics. However, it has been proved to be a potential optical component with the emergence of plasmonics, especially when its dimension is scaled down to nanometer scale. The development of plasmonics research has been primarily driven by its potential applications in real life. Surface plasmon polariton provides an advantageous platform to construct a plasmonic waveguide.[8-10] In addition, SPP can be used to transport information, as we know optical fibre is a good medium for communication application. However, one drawback is that the dimension of optical devices cannot be scaled as small as the wavelength due to the diffraction limit. This diffraction effect can be overcome by converting the light into SPP waves because the SPP resonance wavelength is always smaller than the incidence light. In this case the nanometer size SPP device is feasible to be integrated to the chip to carry digit information.[11-14] Another dominant application of plasmonics is sensing due to the fact that plasmon resonance wavelength is highly sensitive to the surrounding dielectric environment,[15-19] and there were many plasmonics based sensors have been commercialized. The plasmonic sensors can achieve high sensitivity and good selectivity, with detection limit down to femtomolar concentration or even single molecule level. Last but not least, plasmonic device can be used to enhance the emission, such as the enhancement of Raman signal, fluorescence and luminescence.[20-23]

Two kinds of plasmon are involved in the plasmonics study, namely, the propagating plasmon (SPP) and the localized surface plasmon (LSPR) as Figure 1-1 indicates. For SPP the surface plasmon propagates along the *x* and *y* direction while evanescently confined in z direction. While for LSPR, the electron cloud oscillates around the particle with certain frequency and the electromagnetic field is confined near the particle surface. A hot spot will be generated near the particle under the resonance condition. The following content will briefly illustrate the theory of SPP and LSPR by taking the Maxwell's equations as the start point.

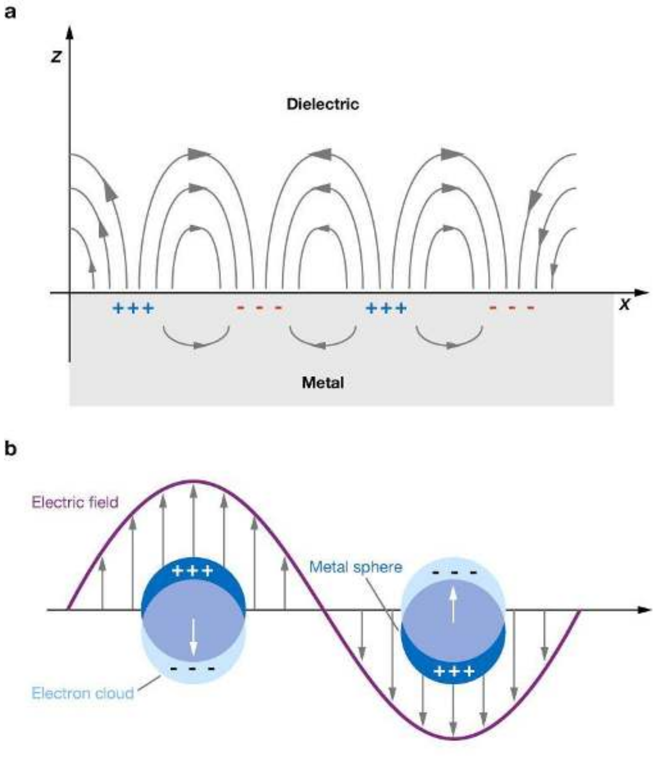

Figure 1- 1 Schematic illustration of surface plasmon. (a) surface plasmon polariton propagating along the metal/dielectric interface. (b) a localized surface plasmon of a metallic sphere.[15]

A typical SPP device configuration is represented in Figure 1-2, a dielectric with dielectric constant ε_d is stacked on a metal with dielectric constant ε_m, the Maxwell equations in this structure can be written as[24]

$$\begin{aligned}
\nabla \times \vec{E}_i &= -\frac{\partial \vec{B}_i}{\partial t} \\
\nabla \times \vec{H}_i &= \frac{\partial \vec{D}_i}{\partial t} \\
\nabla \cdot \vec{D}_i &= \varepsilon_0 \nabla \cdot (\varepsilon_i \vec{E}_i) = 0 \\
\nabla \cdot \vec{B}_i &= \mu_0 \nabla \cdot (\mu_i \vec{H}_i) = 0
\end{aligned} \tag{1-1}$$

Here i means dielectric or metal when it is d or m respectively, ε_0 and μ_0 are permittivity and permeability of vacuum respectively. There are two kinds of solutions to those Maxwell equations, namely, the transverse electric (TE) mode which describes that the electric field is parallel to the *x-y* plane and the transverse magnetic (TM) mode which describes that the magnetic field is parallel to the *x-y* plane. However, for SPP propagating along x-axis, E_z must be non-zero, so that it is must be TM mode if the SPP is excited and the wave vector is on *x-z* plane with $\vec{k} = (k_{xi}, 0, k_{zi})$. The electric field and magnetic field inside dielectric and metal can be expressed as [25]

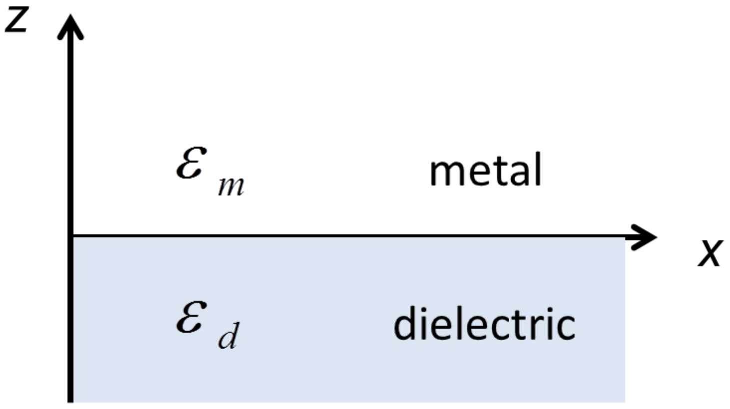

Figure 1- 2 Schematic of metal/dielectric interface.[24]

$$\begin{aligned}
\mathbf{E}_d &= (E_{xd}, 0, E_{zd})\exp[\mathrm{i}(k_{xd}x + k_{zd}z - wt)] \\
\mathbf{H}_d &= (0, H_{yd}, 0)\exp[\mathrm{i}(k_{xd}x + k_{zd}z - wt)] \\
\mathbf{E}_m &= (E_{xm}, 0, E_{zm})\exp[\mathrm{i}(k_{xm}x + k_{zm}z - wt)] \\
\mathbf{H}_m &= (0, H_{ym}, 0)\exp[\mathrm{i}(k_{xm}x + k_{zm}z - wt)]
\end{aligned} \tag{1-2}$$

As we know, both electric and magnetic field are continuous on the interface, which means $E_{xd} = E_{xm}, E_{zd} = E_{zm}$ when z=0, in this case we have $k_{xd} = k_{xm} = k_{spp}$, k_{spp} is the projection of wave vector on x axis. Furthermore, by inserting the expression (1-2) into expression (1-1) we can get

$$\begin{aligned}
k_{zd}H_{yd} + \frac{w}{c}\varepsilon_d E_{xd} = 0 \\
k_{zm}H_{ym} - \frac{w}{c}\varepsilon_m E_{xm} = 0
\end{aligned} \tag{1-3}$$

By combining those two expressions in (1-3) and considering the continuity condition, we can get

$$\frac{k_{zd}}{\varepsilon_d} = -\frac{k_{zm}}{\varepsilon_m} \tag{1-4}$$

From expression (1-4) we can see, if the SPP is excited, the dielectric constant of metal and dielectric must have the opposite sign, in the real case, ε_d is always positive, so we have to choose a metal with negative dielectric constant to realize the SPP. The total wavenumber

$$\begin{aligned}
k_d^2 = k_{xd}^2 + k_{zd}^2 = k_{spp}^2 + k_{zd}^2 = \varepsilon_d(\frac{w}{c})^2 \\
k_m^2 = k_{xm}^2 + k_{zm}^2 = k_{spp}^2 + k_{zm}^2 = \varepsilon_m(\frac{w}{c})^2
\end{aligned} \tag{1-5}$$

By combining expression (1-4) and (1-5) we can obtain the dispersion relation of SPP,

$$k_{spp} = \frac{w}{c}\sqrt{\frac{\varepsilon_m\varepsilon_d}{\varepsilon_m + \varepsilon_d}} \tag{1-6}$$

If we excite the SPP with the same frequency light propagating inside the dielectric, the wavenumber of incidence light is $k_0 = \frac{w}{c}\sqrt{\varepsilon_d}$, obviously $k_0 < k_{spp}$, which indicates that the momentum of incidence light is not enough to excite SPP due to the presence of momentum mismatch. Practically, in order to make the momentum matched and meet the SPP excitation condition, a prism will be added to enhance the momentum of the incidence light or a rough metallic film will be used.

On the other hand LSPR is non-propagating plasmon excited when the nanoparticle is much smaller than the incidence wavelength. LSPR occurs when the conduction electrons of nanostructure are in resonance with the incoming electromagnetic field, in essence, LSPR arises from the scattering issues of sub-wavelength nanostructure within an oscillating electromagnetic field. The interaction between a particle and the oscillating electromagnetic field can be estimated by the *quasi-static approximation* approach when the particle size is much smaller than the incoming wavelength.[4, 26] This method assumes that the volume of the particle is negligible and we can reduce the harmonically oscillation electromagnetic field into a constant field over the whole particle. The problem will be simplified by considering the interaction of a particle in an electrostatic field as Figure 1-3 indicates.

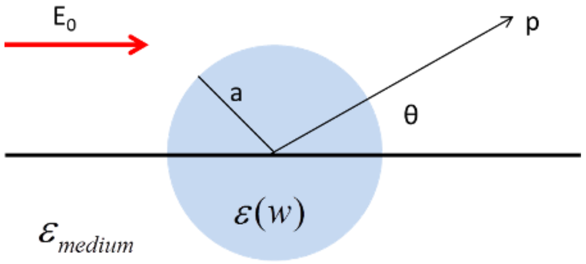

Figure 1- 3 Schematic of a nano sphere in an electrostatic field.[27]

As Figure 1-3 shows, the substance studied is simply represented by a homogeneous metallic sphere with radius a and dielectric constant $\varepsilon(w)$, the surrounding environment of the conductive sphere is isotropic dielectric with dielectric constant ε_m , and the incoming field is parallel to z direction. In the electrostatic approach, the electromagnetic field can be obtained by solve the Laplace equation $\nabla^2\Phi = 0$, where Φ is the electric potential. The general solution of Laplace equation is[15, 27]

$$\Phi(r,\theta) = \sum_{l-=0}^{\infty} [A_l r^l + B_l r^{-(l+1)}] P_l(\cos\theta) \tag{1-7}$$

where $P_l(\cos\theta)$ are the Legendre polynomials of order l, and θ is as indicated in Figure 1-3. Because the potential at the origin point should be finite, the solution inside and outside the sphere can be expressed respectively as

$$\begin{aligned} \Phi_{in}(r,\theta) &= \sum_{l=0}^{\infty} A_l r^l P_l(\cos\theta) \\ \Phi_{out}(r,\theta) &= \sum_{l=0}^{\infty} [B_l r^l + C_l r^{-(l+1)}] P_l(\cos\theta) \end{aligned} \tag{1-8}$$

A_l, B_l, C_l can be determined by considering the boundary condition and then we can come to

$$\begin{aligned} \Phi_{in} &= -\frac{3\varepsilon_m}{\varepsilon + 2\varepsilon_m} E_0 r \cos\theta \\ \Phi_{out} &= -E_0 r \cos\theta + \frac{\varepsilon - \varepsilon_m}{\varepsilon + 2\varepsilon_m} E_0 a^3 \frac{\cos\theta}{r^2} \end{aligned} \tag{1-9}$$

Obviously for the potential outside the sphere, the first term is the applied field, while the second term is the radiation of the induced electric dipole inside the sphere, consider the potential of a dipole is

$$\Phi_{dipole} = \frac{\mathbf{p} \cdot \mathbf{r}}{4\pi\varepsilon_0\varepsilon_m r^3} = \frac{\varepsilon - \varepsilon_m}{\varepsilon + 2\varepsilon_m} E_0 a^3 \frac{\cos\theta}{r^2} \tag{1-10}$$

So we can get the dipole inside the sphere is

$$\mathbf{p} = 4\pi\varepsilon_0\varepsilon_m a^3 \frac{\varepsilon - \varepsilon_m}{\varepsilon + 2\varepsilon_m} \mathbf{E}_0 \tag{1-11}$$

then the polarizability α can be expressed as via the definition $\mathbf{p} = \varepsilon_0\varepsilon_m \alpha \mathbf{E}_0$

$$\alpha = 4\pi a^3 \frac{\varepsilon - \varepsilon_m}{\varepsilon + 2\varepsilon_m} \tag{1-12}$$

It is apparently the polarizability should be maximized to achieve the resonance enhancement, it requires $|\varepsilon + 2\varepsilon_m|$ to be minimum, namely, it requires

$$\mathrm{Re}[\varepsilon(w)] = -2\varepsilon_m \tag{1-13}$$

Based on the Drude mode which describes the dispersive $\varepsilon(w)$ of metallic sphere versus different frequency, once the dielectric constant of surrounding ε_m is changed, the resonance frequency will shift to meet the requirement of expression (1-13), thus LSPR can provide a good platform to detect the refractive index change and widely used in sensing applications.

The electric field $\mathbf{E} = -\nabla\Phi$ can be derived by inserting equation (1-9)

$$\mathbf{E}_{in} = \frac{3\varepsilon_m}{\varepsilon + 2\varepsilon_m}\mathbf{E}_0$$

$$\mathbf{E}_{out} = \mathbf{E}_0 + \frac{3\mathbf{n}(\mathbf{n}\cdot\mathbf{p}) - \mathbf{p}}{4\pi\varepsilon_0\varepsilon_m}\frac{1}{r^3} \tag{1-14}$$

As equation (1-14) shows, both the electric field inside and outside the sphere is enhanced when the nanostructure is in resonance with incoming electromagnetic field, this field enhancement has huge potential application in enhancing Raman signal, fluorescence and luminescence intensity.

The discussion above assumes that the excitation field is absolutely static, while in the real case the excitation field is time-varying and the dipole induced inside the sphere will be oscillating. By combining the time-varying incoming field and the electrostatic method, we can get the oscillating dipole inside the sphere, that is $\mathbf{p} = \varepsilon_0\varepsilon_m\alpha\mathbf{E}_0 e^{-iwt}$. In this case the interaction between the sphere and the incident field can be represented by the interaction of this oscillating dipole with the incident field. The total radiation of an oscillating electric dipole can be written as

$$\begin{aligned} \mathbf{H} &= \frac{ck^2}{4\pi}(\mathbf{n}\times\mathbf{p})\frac{e^{ikr}}{r}(1-\frac{1}{ikr}) \\ \mathbf{E} &= \frac{1}{4\pi\varepsilon_0\varepsilon_m}\{k^2(\mathbf{n}\times\mathbf{p})\times\mathbf{n}\frac{e^{ikr}}{r} + [3\mathbf{n}(\mathbf{n}\cdot\mathbf{p}) - \mathbf{p}](\frac{1}{r^3} - \frac{ik}{r^2})e^{ikr}\} \end{aligned} \tag{1-15}$$

Another interesting consequence of resonant nanoparticle is that it can enhance the efficiency of absorption and scattering. The cross sections of the absorption and scattering can be expressed as[28]

$$\begin{aligned} C_{abs} &= k\,\mathrm{Im}[\alpha] = 4\pi k a^3\,\mathrm{Im}[\frac{\varepsilon-\varepsilon_m}{\varepsilon+2\varepsilon_m}] \\ C_{sca} &= \frac{k^4}{6\pi}|\alpha|^2 = \frac{8\pi}{3}k^4 a^6 \left|\frac{\varepsilon-\varepsilon_m}{\varepsilon+2\varepsilon_m}\right|^2 \end{aligned} \tag{1-16}$$

It is clearly seen that the absorption is proportional to a^3 while scattering cross section is proportional to a^6. In the case when the radius of sphere is much smaller than incidence wavelength, the absorption dominates over the scattering.

Overall, the incoming oscillating field can induce an oscillating dipole inside the nano structure. The total field will be redistributed when this dipole is resonant. In addition, it will enhance the absorption and scattering frequency. In contrast to propagating SPP which is limited by momentum mismatch, LSPR can be excited directly with light illumination, which broadens the application of LSPR devices.

1.2 Metamaterials

Humankind never ceased from creating new materials with the properties beyond the naturally occurred materials. Materials innovation partly motivates the advancement of human society, for example, the invention of bronze, ceramics, metal alloy and the doped silicon was vital in human society progression. Recently metamaterial has attracted tremendous attention due to its ability in engineering and manipulating electromagnetic field. Metamaterial is a kind of artificial material which possesses the properties we cannot find in the naturally occurred material, thus it is termed as “metamaterial”. As we know, the nature materials are composed of atoms or molecules and those atoms are arranged in certain order. The physical and chemical properties of naturally occurred materials are determined by the elements of those atoms or molecules and the bond between them. In analogy to the conventional crystals found in nature, metamaterials are constructed by arranging the artificial “meta atoms” periodically, the “meta atom” is specially designed to have specific optical response. Usually, the optical response of single "meta atom" can be engineered by properly changing the shape, size and materials composition. The properties of this artificial metamaterial can be evaluated by considering the property of those single "meta atom" and the interaction between them. Consequently, the artificial metamaterials can be treated as a homogenous substance and their optical property can be represented by an effective electric permittivity $\varepsilon_{eff}(w)$ and magnetic permeability $\mu_{eff}(w)$.[29-34] In essence, metamaterial is designed for us to engineer the $\varepsilon_{eff}(w)$ and $\mu_{eff}(w)$ as desired to implement the optical properties beyond the naturally occurred materials. In contrast to the natural crystals, the properties of metamaterial are dominantly determined by the structure, configuration and arrangement of the "meta atom" while the material composition of "meta atom" has limited effects.

Before the emergence of metamaterial, photonic crystals have been demonstrated to be effective in manipulating light propagation. Photonic crystal is composed of a periodic dielectric scatter array which can influence the motion of photons. In analogy to the intrinsic energy band formed in a semiconductor because the periodic potential affects the motion of electrons inside the crystals, a band gap will present in a photonic crystal to inhibit the propagation of electromagnetic field with specific wavelength.[35-37] In spite of the fabrication challenge, photonic crystals have been already demonstrated in 3-dimension and many of those photonic crystal devices have been commercialized. In photonic crystal, both the size of scatter elements and the periodicity are of the order of the incidence wavelength.[38, 39] However, for metamaterials the size of "meta atom" usually is smaller than the incidence wavelength and the "meta atom" is a metal instead of dielectric.

Electric permittivity ε and magnetic permeability μ are the parameters to illustrate how the material will be polarized by the incoming electric and magnetic field respectively. Based on the value of permittivity and permeability, the materials can be classified into 4 quadrants as Figure 1-4 indicates, the materials located in each quadrant have their own special properties and characteristics. For most common dielectric, both the permittivity and permeability are positive as quadrant I shows, and they are easily to be polarized by the electromagnetic field and the optical loss is relatively low. Quadrant II includes most of the metals which have negative permittivity while positive permeability, as we discussed it was the negative permittivity makes the metal widely used in plasmonics study. Quadrant IV is indicating the ferrites which have intrinsic magnetism and they have negative permeability. The materials possess negative permittivity and permeability simultaneously are absent in naturally occurred materials, it is interesting to explore this kind of materials because they have huge potential in the application of negative refraction and super resolution lens.

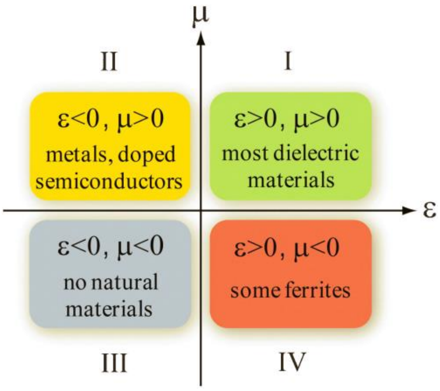

Figure 1- 4 Classification of materials based on the permittivity and permeability.[40]

Metamaterials provide a good platform to implement the double negative materials. Most of the materials used to construct metamaterials have negative permittivity within optical regime, so the key part is to realize negative permeability within optical regime simultaneously.[31, 32, 41-43] In order to achieve a negative permeability, we have to use a meta atom which can be resonant to the magnetic field and generate magnetism. Pendry *et al.* firstly proposed that a split ring resonator (SRR) can generate strong magnetism due to the induced circulating current.[44] Following SRR, many other structures were proposed to generate artificial magnetism such as the fishnet and nano rods.[45-48] One primary motivation of metamaterials is to push the magnetic resonance to higher frequency, making it much higher than the resonance frequency in the naturally occurred magnetic material. The first metamaterial was demonstrated in microwave regime and it was further pushed to terahertz by scaling down the meta atom size.[42, 49, 50] With the fabrication technique revolution from PCB lithography, photolithography to electron beam lithography, people can make the meta atom smaller and smaller even to tens of nanometers and further push the magnetic resonance into near infrared and visible range.[51-54] Theoretical investigation suggests that the resonance frequency will not become higher with the size scaling down, there exists saturation in near infrared –visible range where the metal becomes less ideal and we have to consider the motion of the electrons inside the metal. The theoretical magnetic resonance limit is limited by the intrinsic plasmon frequency of each metal, it was demonstrated silver metamaterial can operate at visible range.[55]

It was believed that realization of 3-dimentional metamaterial was the key step in the transition from scientific research to practical application. People have made enormous effort on 3D metamaterials research, firstly the printed circuit boards were stacked together to form a bulk metamaterials operating in gigahertz. However, it is very challenging to fabricate 3D metamaterials operating in optical regime due to that the size is quite small. Na Liu *et al.* reported an infrared 3D metamaterials by stacking the elements layer by layer using electron beam lithography.[56] It was also reported that a near infrared metamaterial was fabricated by a nano printing method.[57] Overall, there is still a long way to make a 3D metamaterials into real devices because the fabrication is very challenging and the area of the structure is quite small. In addition, the absorptive loss is quite high of the metallic elements in 3D metamaterials. Jumping out from 3D metamaterials, people shift the attention to the 2D metasurfaces, it becomes more and more clear that 2D metasurfaces is most promising to be the first generation metamaterials based devices.[58-60] The elements used to construct metasurface are plasmonics structures whose optical response is determined by the plasmon resonance. As we discussed above, a Lorentz oscillator will present inside the plasmonic structure when it is exposed to a time-varying electromagnetic field. When all the plasmonic atoms are put together periodically to form an array, the optical response will be significantly modified with respect to the individual plasmonic atom due to the interaction between adjacent particles. When the separation of meta atom is of the order to incidence wavelength, a surface lattice resonance will appear due to the interference of the diffractive far-field.[61-63] However, when the separation is smaller than the resonance wavelength, the scattered wavefront can be tailored by varying the meta atom shape. Both resonance amplitude and phase can be modified by changing the separation and particle size, facilitating the application of this metasurface in lasers and phase gradient devices. [64-67]

1.3 Surface enhanced Raman scattering

Scattering describes the light or other electromagnetic radiation that is scattered by a substance, which is a common phenomenon in nature. The reason why we can observe a blue sky is that the blue light is more efficiently scattered by the particles in air, which is a Rayleigh scattering[68]. For Rayleigh scattering, the incident light and the scattered light have the same frequency, it is the result of the electric polarizability induced inside a particle[69]. Physically, a time-varying electromagnetic field can drive the electrons of a particle to oscillate with the same frequency and induce an oscillating dipole. The scattered light we observed is the radiation of this oscillating dipole and the photon energy of this radiation is same as the incident photon. When light is scattered by a molecule, majority of the interactions are elastic scattering known as Rayleigh scattering, while there exists a small fraction of inelastic scattering with the energy difference between the scattered light and incident light, which is termed as Raman scattering.[70] Raman scattering was firstly discovered by Indian scientist C. V. Raman so that this radiation was named after his name.[71-73] The Rayleigh scattering and Raman scattering can be described by the diagram in Figure 1-5.

In the case of Rayleigh scattering, the molecule in ground state is excited to a virtual state by absorbing an incident photon and then relaxes to the original ground state by emitting a photon with the same energy as the incident photon. Raman scattering consists of two kinds of processes, namely, Stokes and anti-Stokes Raman scattering. For Stokes Raman scattering, the molecule in ground state is excited to a virtual state and then relaxes to a higher energy vibrational state by emitting a photon with energy smaller than the incident photon, while in the anti-Stokes Raman scattering process, the molecule in an excited vibrational state is excited to a virtual state and then return to the ground vibrational state so that the emitted photon has the higher energy than the incident photon.

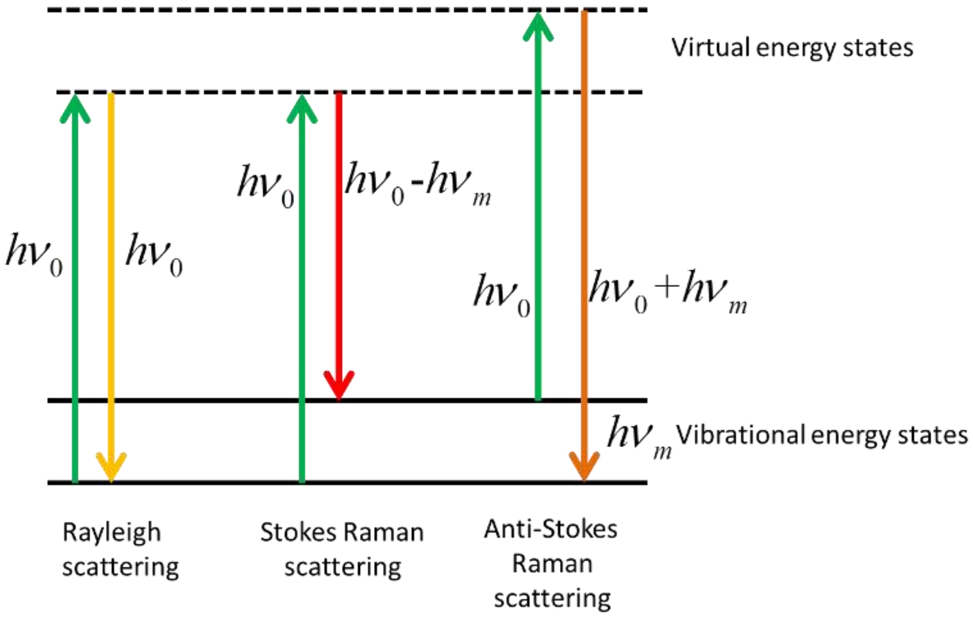

Figure 1- 5 Energy diagram for Rayleigh scattering and Raman scattering.

The ratio of Stokes Raman scattering to anti-Stokes Raman scattering depends on the population of initial molecules states. Based on thermal dynamics, the higher energy vibrational state is less populated than the ground vibrational state so that the probability of Stokes transition is larger than anti-Stokes transition. Apparently, the relative intensity between Stokes and anti-Stokes can be tuned by changing the temperature, essentially changing the relative population between higher and lower vibrational states. From the view of classical description, the incident photon can induce an oscillating polarization in a molecule or crystal, Raman scattering is active only when the polarization can couple to other polarizations such as vibrational, rotational or electronic excitations and consequently the emitted photon will loss or gain energy. If the oscillating polarization cannot couple to those vibrational, rotational and electronic excitations, the molecule will return the state it starts from and the Rayleigh scattering undergoes.

From figure 1-5 we can see the energy difference between the incident photon and the scattered photon is identical no matter in Stokes or anti-Stokes Raman scattering. In addition, the energy difference reflected in Raman scattering is independent on the incident laser wavelength. This vibrational energy reflected in Raman scattering usually can be treated as the chemical *fingerprint* of the specific molecule or crystal so that Raman scattering was widely used in substance identification and analysis in complementary to infrared spectroscopy.[74-78] Raman scattering measurement is feasible in any form of materials no matter gas, liquid or solid.[79] However, the Raman scattering cross section is quite small (10^{-31} cm^2/molecule $< \sigma < 10^{-29}$ cm^2/molecule), which suggests that we have to utilize enormous molecules within the laser spot to produce considerable Raman signal. It will be challenging if we want to detect or analyze a low concentration material or even a single molecule because the Raman signal is too weak to be detected by a normal spectrometer.

Surface enhanced Raman spectroscopy (SERS) is such a technique to enhance the Raman signal dramatically, enabling the detection of small amount of molecules or even a single molecule.[20, 80-83] The observation of SERS phenomenon can be traced back to 1974 when M. Fleischman studied the Raman scattering of pyridine absorbed on electrochemically roughed silver electrodes, intuitively they attributed the enhanced Raman signal to increased amount of molecules absorbed on the electrodes due to the roughness.[84] L. Jeanmaire and P. Van Duyne pointed out that the real Raman scattering cross section in measurement far exceeded the cross section enhancement resulted from the increased molecules absorbed, which leaded people to think that there was another mechanism behind to enhance the Raman signal and consequently discovered SERS.[85] Quickly in 1978 Martin Moskovits proposed that the surface plasmon excited on rough electrodes was responsible for the dramatic Raman signal enhancement.[86] Based on the Moskovits's assumption, structures which can sustain a surface plasmon were capable of supporting SERS effects. Over the past

30 years, people exploited numerous SERS active structures such as colloids, arrays, nanowires to obtain high enhancement factor and investigated the principle behind SERS.[87-92]

The mechanism of SERS is still in debate. Until now, there are two main theory recognized by the SERS community, known as electromagnetic theory and chemical theory. The electromagnetic theory argues that the Raman enhancement emerges from the near field enlargement of a particle.[93-97] As we discussed above, the electrons inside a metallic particle will displace with respect to the ion core when it is exposed to a time-varying electromagnetic field and an oscillating dipole is formed. When the dimension of the particle is much smaller than the incident wavelength, we can eliminate the spatial retardation effects and the other high order multipoles were negligible except the oscillating electric dipole. The induced oscillating dipole will radiate electromagnetic field and redistribute the field outside the particle so that the near field will be dramatically enhanced when the induced dipole is in resonance with the incident excitation. Raman scattering we discuss in this thesis is spontaneous Raman scattering and it is a linear process, the scattered field can be expressed as

$$I = \left|E_{Raman}\right|^2 = N\sigma_R \left|E_{excitation}\right|^2 \tag{1-17}$$

here N is the amount of molecules involved of the Raman scattering process, σ_R is the Raman cross section. When an incident electromagnetic field with magnitude E_0 strikes on a nanoparticle, the total near field outside the particle will be enhanced to gE_0 after adding the radiation field from the resonant particle E_s. In the case the SERS probe (Molecule in figure 1-6) is in close proximity to the particle, it is the field with magnitude gE_0 excites the molecule but not E_0, so the real excitation field $E_{excitation}$ will be gE_0. In the same manner with the incident field, the Raman scattering field E_R from the molecule will be enlarged to $g^{'}E_R$ which is really detected in the measurement.

After those two field enhancement process, expression (1-17) can be rewritten as

$$I = \left|g^{'}E_{Raman}\right|^2 = N\sigma_R \left|g^{'}\right|^2 \left|E_{excitation}\right|^2 = N\sigma_R \left|gg^{'}\right|^2 \left|E_0\right|^2 \tag{1-18}$$

we can see the Raman signal intensity is enhanced by a factor $\left|gg^{'}\right|^{2}$ by comparing the Raman intensity without the presence of metal particle. When the Raman shift frequency is small, namely, the frequency of E_0 and E_R are approximately equal, in this case the field enhancement of incident field and Raman scattering field are almost identical ($g \approx g^{'}$). Expression (1-18) suggests that the SERS enhancement factor is proportional to the fourth power ($\left|g\right|^{4}$) of the field enhancement.

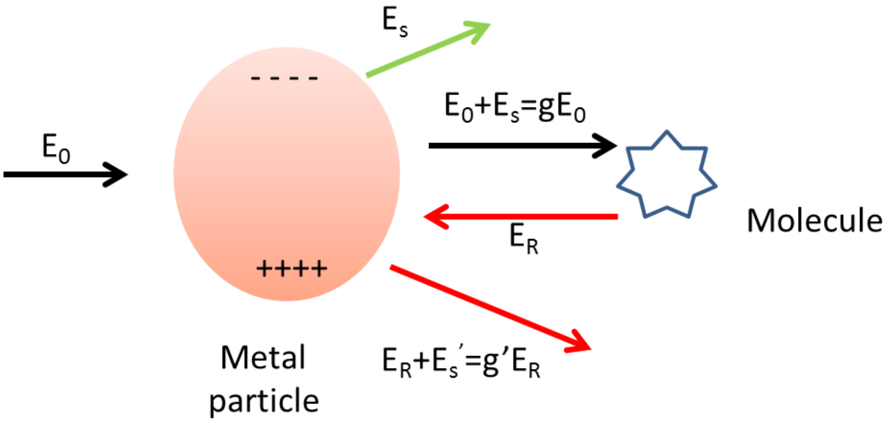

Figure 1- 6 Schematic illustration of electromagnetic mechanism of SERS.

Electromagnetic theory offers a reasonable explanation of the dramatic Raman signal enhancement, for instance, a 100 times field enhancement can bring 10^8 times SERS enhancement. It was well known that the field enhancement is in maximum at the localized plasmon resonance frequency. In order to optimize the SERS enhancement factor, we have to make the incident light frequency and the Raman Scattered light frequency match the LSPR frequency of the particle. In the case when the Raman shift frequency is relatively large, there exists a trade-off in optimizing both g and $g^{'}$. If we make the incident light resonant with the particle perfectly, we can obtain a highest g, however, the Raman scattered light frequency is far from the LSPR frequency and $g^{'}$ is relatively low. It is the same situation if we desire to maximize $g^{'}$. Consequently SERS enhancement factor is not always proportional to the fourth power of the field enhancement factor.[98, 99]

In practical applications, a method to optimize the SERS enhancement factor is to tune the incident light wavelength, alternatively, another approach is to tune the

LSPR frequency by tuning the size of the particle. To some extent, SERS is a branch of the nanoscience which is highly correlated to the advancement of the nano fabrication and characterization technique. It is required to make the size of the SERS active particle much smaller than wavelength, usually around tens to hundreds of nanometers. If the size of the nanoparticle is comparable to the incident light wavelength, the multipole inside the particle will be excited. It was also demonstrated for some specific structures like the nanowire, the high order resonance can give a higher SERS enhancement due to the higher field confinement at the end of the nanowire.[100] Apart from the surface plasmon resonant excitation, it is necessary to point out lightning rod effect also contribute to the electromagnetic SERS enhancement. Lightning rod effect which describes that the field will be confined near the sharp tip of the metallic purely arises from the geometric effect of the structure.[101, 102] Generally, the structure with many sharp features can enhance the Raman signal further.

Despite electromagnetic SERS enhancement contribute to the main part of the signal enhancement, it cannot explain the SERS magnitude completely. We have to consider chemical enhancement when the molecules are in contact with the metallic particles.[103, 104] In the scenario SERS molecules are in contact with the metal, there exists charge transfer between them and the property of the molecule is modified. σ_R in expression (1-17) refers to the Raman cross section of the pure molecule, however, σ_R will be modified when the surrounding of the molecule change. In the presence of charge transfer, σ_{SERS} is larger than σ_R and the Raman intensity is enhanced naturally. Theoretical simulation indicates that the maximum enhancement because of the increased cross section is on the order of 100, which is much smaller than the electromagnetic enhancement.

SERS on individual particle is a good platform to understand the mechanism, but for practical application, assembling sample is used to achieve higher signal. People usually utilize aggregated particles, arrays or clusters to construct a SERS platform, the reason is that the coupling between two adjacent elements gives rise to a giant field enhancement comparing with an isolated particle.[105] For example, this kind of coupling can be represented by the interaction of the dimer. When the dimer is illuminated by an electromagnetic field with polarization parallel to the axis, an electric dipole will be induced inside each particle. As the two particles are brought together, the incident field and the radiation of another particle will simultaneously serve as the excitation to induce the dipole in another particle, which leads to the giant field enhancement in the gap between the dimer due to the increased polarization. If the gap between the particles is quite narrow (~1 nm), the hot spot formed is extremely strong, enabling the detection down to a single molecule.[82, 83, 106] However, the field cannot be always enhanced by reducing the gap further because it will reach the quantum regime and the field intensity in between the gap will saturate.[107] Another highly performed SERS platform is tip enhanced Raman scattering in which the cavity is formed between a sharp tip and a particle and a very intense hot spot is obtainable.[108] It has been proven the tip enhanced Raman scattering is feasible to detect a single molecule.[109]

As we know, any material supporting surface plasmon has the potential to be the SERS materials candidate. Gold and silver are the most used SERS materials because their surface plasmon resonance is located between visible to near infrared regime and the LSPR resonance can match most of the excitation laser wavelength and the Raman shift of the analytes. In addition, gold is stable in the atmosphere and can serve as a reproducible SERS template. Recently, it is desired to implement the SERS effects in the ultraviolet (UV) regime because there are many biomolecules whose vibrational band is in UV regime. The UV resonance frequency has been demonstrated in many metals such as aluminum, nickel, indium and those metals hold the significant promise of the application in UV SERS.[110, 111]

1.4 Motivation

Metamaterials and plasmonics have attracted tremendous consideration within the last decade and numerous applications have been demonstrated such as light manipulation, invisible cloak, sensing and energy harvesting. Most of the metamaterial and plasmonic structures were fabricated on a non-transparent and rigid substrate, which limited their applications in practical situation. It is desired to integrate metamaterial and plasmonic structures onto some novel substrates to improve their functionalities. First of all, the integration of metamaterials and plasmonic structures to a flexible substrate can provide the advantages such as transparency, deformability, light-weight and biocompatibility. It is meaningful to explore the fabrication method to prepare metamaterials and plasmonic structures on a flexible polymer. More importantly, it is of great importance to develop the applications of the flexible metamaterials and plasmonic structures. Secondly, it will be of great significance to attribute metamaterials and plasmonic structure to a phase change material and we expect a tunable response. In addition, the tunable metamaterials hold great potential in sensing application.

Fano resonance has been demonstrated to possess high sensitivity in sensing due to the sharp spectra. Previously Fano resonance mainly arised from the interaction between the electric modes. However, it is significant to explore the Fano resonance emerging from the interaction between magnetic mode and electric mode. It is expected that the magnetic mode based Fano resonance can generate huge magnetism with optical excitation. In addition, it is promising in the application of negative refractive index materials.

1.5 Organization of this thesis

Based on the motivations discussed in section 1.4, the rest of the dissertation is arranged as follows.

In chapter 2, the fabrication of the metamaterials and plasmonic structures are discussed in details. We mainly rely on electron beam lithography to fabricate nano structures. The whole electron beam lithography process is introduced in sequence. The thin film deposition technique *i.e.* thermal evaporation and sputtering are also presented. Apart from the fabrication, the characterization methods are introduced.

Scanning electron microscopy is used to identify the nano structure morphology. Microspectrophotometer and a UV/vis/Near IR spectrometer are used to measure the reflection and transmission to characterize the optical properties. Raman spectroscopy system is also introduced at the end of chapter 2.

In chapter 3, the fabrication method to transfer metamaterials from rigid substrate to polymer is presented. The SiO_2 and nickel sacrificial layer transfer method are compared. The SERS application of the free standing and transparent metamaterials is performed. At last, the coupling between metamaterials and metal film is investigated experimentally and theoretically.

In chapter 4, the active metamaterials and plasmonic devices are introduced firstly. Then the growth of vanadium dioxide is presented to prepare high quality of vanadium dioxide thin film. The optical response of metamaterials fabricated on VO_2 film was measured to demonstrate the resonance tunability. At last, a tunable SERS device is presented by utilizing the tunable metamaterial device.

In chapter 5, the basic of Fano resonance and magnetic mode based Fano resonance serve as the introduction. Next, the split ring/disk is discussed and fabricated. Then the high order magnetic mode based Fano resonance is demonstrated experimentally and the simulation is conducted to confirm our interpretation. Then the sensing application of magnetic based Fano resonance is conducted.

In chapter 6, the absorption performance of ultrathin $Ge_2Sb_2Te_5$ film absorber is measured. Then the phase change is introduced to engineer the absorption performance. At last, the plasmonic structure is combined to the thin film absorber to broaden the absorption band.

The summary and future work is presented in chapter 7.

Chapter 2 Fabrication and Characterization

2.1 Nano device fabrication

2.1.1 Electron beam lithography

Nanofabrication technology has been playing critical role in the emergence of nanoscience. As we know, in semiconductor industry Moor's law describes that the number of transistors on an integrated circuit will double every 18-24 months, which eventually demands miniaturization of the elements down to nanometer scale within a complex circuit system. Commonly nanofabrication technique aims to obtain fine structure with the feature between 1 to 100 nm. Over the past decades, a revolutionary progress has been made in the nanofabrication technique, making it readily possible to fabricate the structure down to several nanometers. Many conventional and unconventional fabrication methods were proposed and tested in the exploration of nanofabrication skill. Here conventional methods mainly refer to the technique based on lithography which origins from the conventional microelectronics such as electron beam lithography (EBL),[112] focused ion beam lithography (FIB)[113] and optical projection lithography.[114] Those lithographic methods share the same fundamental principle that the pattern is firstly formed on the resist and then transferred to a rigid substrate by etching, re-growth or lift off procedure (figure 2-1).[115] All these lithographic methods are known as a "top-down" method and widely used in the semiconductor industry. Apart from those conventional approaches, many unconventional methods were invented to meet the various requirements in practical application, which include nanoimprint methods, near field optical lithography,[116] laser interference lithography[117] and a typical "bottom-up" approach nanosphere self-assembly[118, 119], *etc*. Each method has its own advantages and disadvantages when it comes to the real application and consideration of the effects such as the feature resolution, cost, time consuming, large scale production and so on. In this thesis the fabrication method we use is EBL for the lab application with high resolution but limited in the pattern scale.

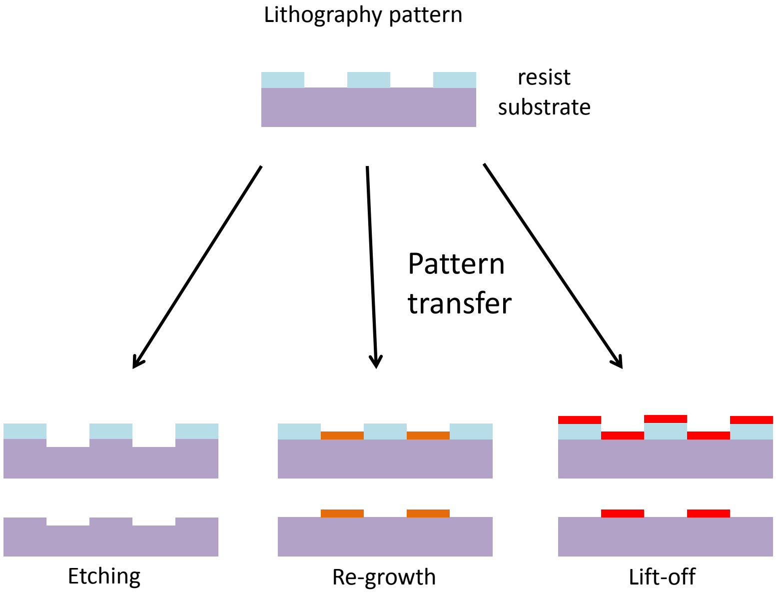

Figure 2- 1 Schematic illustration of lithography process. The pattern can be transfer from resist to rigid substrate by etching, re-growth and lift-off procedure.[115]

Electron beam lithography is highly recommended in the fabrication of tiny structure due to its ultrahigh resolution. In industrial standard process, EBL is used together with other pattern transfer methods to improve the productivity. Firstly, EBL is used to pattern tiny structure on a mask, subsequently optical projection lithography is utilized to reproduce the pattern on the mask to achieve mass production.[120] In the lab research, the main purpose of EBL is to pursue high resolution and accuracy. Because the main process involved during the EBL process is the interaction between electron beam and the resist, naturally we should consider those three factors as following to improve the resolution and accuracy. The first factor is the electron beam itself, how small a feature we can achieve is primarily decided by the diameter of the incident electron beam. Secondly, we should consider the interaction between the electron beam and the resist, such as the motion of the electron after striking the resist and the proximity effects. The third factor we should consider is the choice of the resist, the sensitivity and stability to electron beam, the molecule weight, *etc.*, should be evaluated carefully.

For a standard EBL system, the electrons were generated with a thermal field emission and then converged to a Gaussian shape beam by a column of components including magnetic lens, beam blanker and the beam deflector as shown in figure 2-2.[121] Although many other beam shape were explored, the Gaussian beam is the best choice to attain the highest resolution and can write a pattern with feature size below 10 nm.[122] The diameter of the Gaussian beam can be scaled down to 2-7 nm and it is affected by many factors such as the electron source, condenser lens, diffraction effect and the Coulomb interaction.[123] When the emission current is quite small, the Coulomb interaction is negligible and the beam diameter is small enough to achieve high resolution. If we want to improve the throughput, the emission current should be higher, so that the Coulomb interaction becomes more and more apparent and the electron beam intends to diverge. In short, the high throughput and high resolution is contradictory. In addition, a higher acceleration voltage can introduce a smaller beam and improve the resolution. However, a higher voltage will lead to a longer mean path and make the proximity effect more severe.

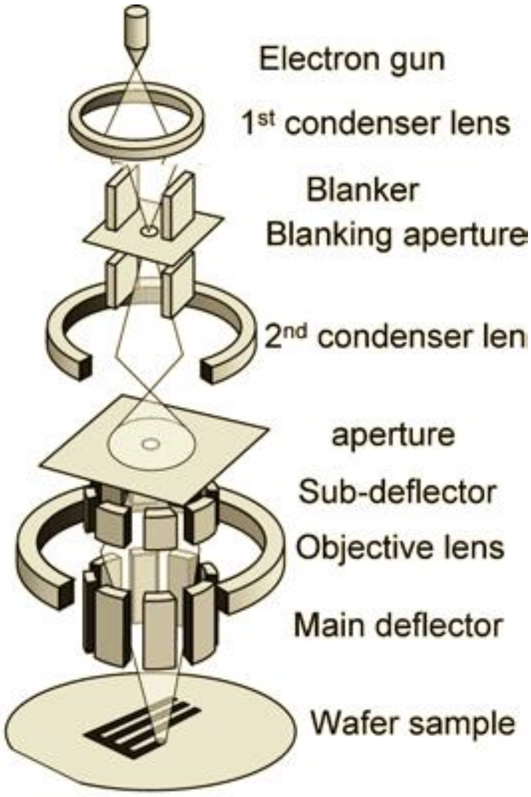

Figure 2- 2 Schematic illustration of the electron beam lithography system.[121]

The electron beam pattern is formed by scanning the electron beam on a resist based on the computational design. It is critical to understand the interaction between the incident electron beam and the organic polymer. The principle of EBL is that the resist is changed physically or chemically due to the electron exposure. For positive resist, the electron beam will cut the long chain and convert the big molecule to pieces of small molecules. On the contrary, electron beam will cross-link the negative resist molecules together to form a bigger molecule. The small molecules will be dissolved in the developing solution so that the exposed area will be removed for positive resist while the unexposed will be removed for negative resist. The interaction between electrons and resist can be simply resolved by considering the energy of the electrons dissipating into the molecules to implement the cutting or cross-linking. The amount of molecules which have been cut or cross-linked is proportional to the total energy transferred to the resist and the shape of the pattern written by EBL is defined by the spatial distribution of the dissipating energy. Apart from the incident electron, the scattered and the secondary electron will slightly expose the adjacent resist regime where is not desired to be exposed so that the real exposed pattern is different from the pattern as designed, which is known as *proximity effect*.[124] The proximity effect can be understood by considering that we expose a point with an electron beam, the result is that a circle with a diameter larger than the beam diameter will be effectively exposed, so the proximity effect refers to the additional exposed part. Proximity effect is a major factor which affects the patter accuracy. Some methods to correct the proximity effect have been developed.[125, 126] The first one is to modify the design patterns to make it slightly different from the desired pattern and the exposed pattern including the proximity effect is the desired pattern.[127] Another method is to expose an additional background dose to correct the proximity effect energy distribution, which is known as GHOST method.[128]

The choice of resist is very important in order to achieve high resolution, a resist with high sensitivity will be useful to improve the throughout, while it is proven that a less sensitive resist can introduce a higher resolution. Poly(methyl methacrylate) (PMMA) is a typical positive resist widely used in EBL with the sensitivity around

50-500 $\mu C/\mathrm{cm}^2$ and a feature size with 3-5 nm is attainable by using PMMA.[129] In order to improve the resolution, resist with smaller molecule weight like Hydrogen silsesquioxane (HSQ) is also widely utilized.[130]

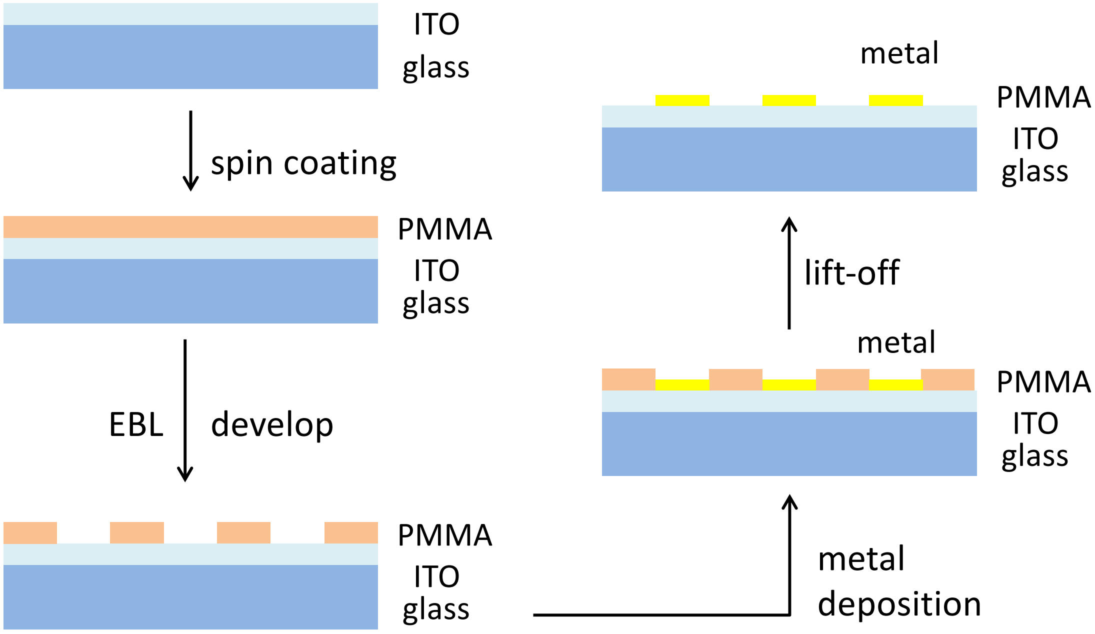

Figure 2- 3 Schematic flow of a standard EBL fabrication process on ITO glass.

In this thesis, a JEOL-7001F field emission scanning electron microscopy equipped with a nanometer pattern generation system (NPGS) was used as an electron beam lithography system. The fabrication process is indicated in figure 2-3. The original substrate was a commercial ITO glass which has conductive surface to eliminate the charge effect. After cleaning the substrate with the ultrasonication and oxygen plasma treatment, PMMA A4 (Microchem, USA) was spin-coated on the top with the spin rate of 4000 rpm for 1 minute and it gave the thickness of PMMA around 200 nm. After baking for 18 minutes at 180 °C, the chip was ready for the EBL. The pattern we wanted write was firstly designed in a computer with the designCAD software and then transferred to NPGS system to generate a corresponding run file. The acceleration voltage we used was 30 kV and the emission current was around 70 μA. The work distance was fixed at 15 mm and the magnification we used was $\times 1600$. After electron beam exposure, the chip was immersed in developing solution MIBK/IPA (Microchem, mixed with the volume ration 1:3) for 90 seconds and then rinsed with IPA, followed by a blow-dry procedure with nitrogen gas. The metal was deposited with a thermal evaporator (Elite, Singapore), subsequently a standard lift-off process was engaged by immersing the chip in acetone. Finally, the designed pattern was transferred to the metal film after removing the unexposed part.

2.1.2 Thermal evaporation

The mechanical, electrical and optical properties of thin film are totally different from the bulk materials, most of the electric semiconductor devices and the optical coating are relying on the formation of a thin film sequence. It is desired to deposit high purity and good uniformity thin film on a wafer scale. The methods to deposit a thin film can be classified into two kinds which are chemical vapor deposition (CVD) and physical vapor deposition (PVD). A chemical reaction is involved in all CVD methods to create the desired materials. Normally, the material used is a compound consisting of the desired material and the volatile precursor, a decomposition reaction will remove the precursor and the left desired material will resides on the substrate in the chamber. The byproducts produced in the reaction must be removed by a gas flow. Based on the different kinds of CVD configuration, there are many methods to trigger the chemical reaction such as heating, plasma, *etc.* It is important to note that the CVD approach does not require high vacuum, it can be done in reduced or normal atmosphere pressure. However, physical vapor deposition is accomplished by a physical reaction in which the morphology change is enabled. In the standard PVD process, a target material with very high purity is vaporized and then transport for a distance until it encounters the substrate. The vapored materials will condensed again on the substrate to form a uniform thin film. The PVD system requires a very high vacuum to exclude the collision between the vapored materials and the air molecule so that it can reach the substrate successfully. Base on the different PVD configurations, there are many different ways to vaporized the bulk material, for instance, the Joule heating (thermal evaporation), electrons heating (electron beam deposition), laser irradiation (pulsed laser deposition) and plasma (sputtering). In this thesis, all the thin film deposition is accomplished by either thermal evaporation or sputtering.

The first demonstration of evaporated deposition can be traced back to 1857 when Faraday.M. prepared a thin film with an metallic wire.[131] Later on, Nahrwold and Kundt implanted the thin film deposition by thermally heating the bulk material, which was probably the first demonstration of thermal evaporation.[132] At that period time, it was very difficult to maintain a decent vacuum and all the applications of thermal deposition were limited inside the laboratory. The formation of thin film facilitated the study of the properties of the thin film with the thickness down to nanometer dimension. A typical thermal evaporator system consists of a vacuum system and a chamber. The vacuum system is heart of the whole system, normally it is working in two levels. First level is the rough pumping with a mechanical pump and it can achieve 10^{-2} Torr vacuum. The Turbo pump or Cryo pump will start working when the vacuum reach a critical value and the chamber will be further pumped down to 10^{-7}-10^{-8} Torr. The configuration inside the chamber is schematically shown in figure 2-4.

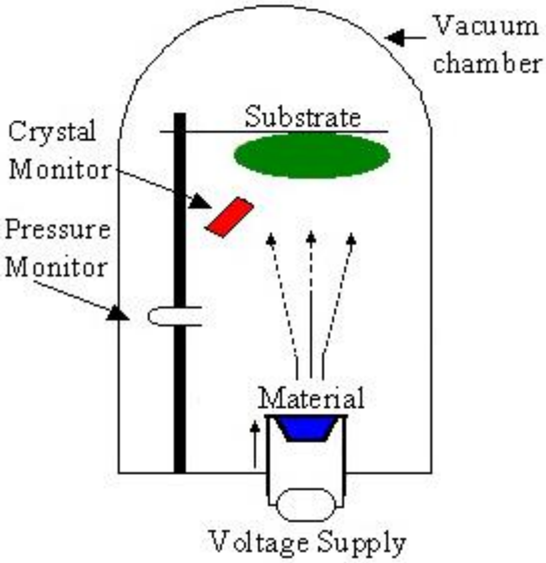

Figure 2- 4 Schematic configuration of the vacuum chamber.

The bulk materials with high purity are put in the bottom and there is a power supply setup to apply large current on the evaporation source to generate Joule heat to melt the materials on it. The sample holder is located on the top and face to the evaporation source with a reasonable distance. Usually a crystal sensor and a pressure monitor are installed inside the chamber to monitor the deposition rate and the vacuum value respectively. It is apparent that the materials start vaporizing when the local temperature is above its melting point and the vapor goes up straightforward and re-condense on the substrate above.

In order to achieve a good thin film deposition process, it is important to divide the whole evaporation process and consider the theory or mechanism behind it. The first step is the vaporization of the bulk material. The transition from a solid state to a gaseous state is a thermodynamics process and the evaporation rate can be estimated by the following expression known as Hertz-Knudsen equation.[133]

$$\frac{dN}{Adt} = \alpha(2\pi mkT)^{-1/2}(p^* - p) \tag{2-1}$$

here *dN /dt* is the total amount of molecules escaping from the solid matter within time *t*. *A* is the total area of the solid surface, α is the evaporation coefficient, *k* and *T* are the Boltzmann's constant and the absolute temperature respectively. p^* refers to the equilibrium vapor pressure at the surface and *p* indicates the hydrostatic pressure on the matter surface. It is clearly shown that the evaporation rate is related to the temperature and the evaporation coefficient which is dependent on the material.

The second step is the transport of the vapor from the source to the substrate, this process requires that the vacuum is high enough to guarantee that the vapor molecule will not suffer too many collisions before reaching the substrate. The mean free path is a parameter to indicate the average travelling distance of the gaseous molecule between every two consecutive collisions and it is expressed by

$$\lambda = kT / \sqrt{2}\pi P d^2 \tag{2-2}$$

here *P* means the pressure and *d* is the diameter of the vapor molecule. For example, the diameter of a gold atom is 0.2 nm, and the normal pressure of the thermal evaporator is 10^{-5} Pa, under these circumstances, the mean free path is approximately about 1200 m. Such a long mean free path suggests that the vapor molecule will head to the substrate directly in a straight line without any collision with other molecule on the route.

The last step of the thermal deposition is the re-condensation on the substrate. The energy of the incident gaseous molecule is around 0.5 eV and they accumulate together to form a film on the substrate. The mechanic properties are affected by the substrate temperature, additionally, the relative position of the source and the substrate influence the uniformity of the film and a shadow effect is most likely to present for a patterned substrate. As indicated in figure 2-5, all the gas molecules travel in a straight direction without any collision and it is impossible for materials to be deposited on region 1 due to the presence of the pattern. Though region 2 is completely covered by the material deposition, its thickness is not uniform. One common method to relieve the shadow effect is to rotate the substrate in a constant rate so that the relative positon between a pattern and the source is changing in real time. It also need to be noted that the shape of the source affect the deposition rate distribution as well. The directionality and the deposition rate distribution on the substrate will be altered when change the point source to a wire, plane, circle or a cylinder source.

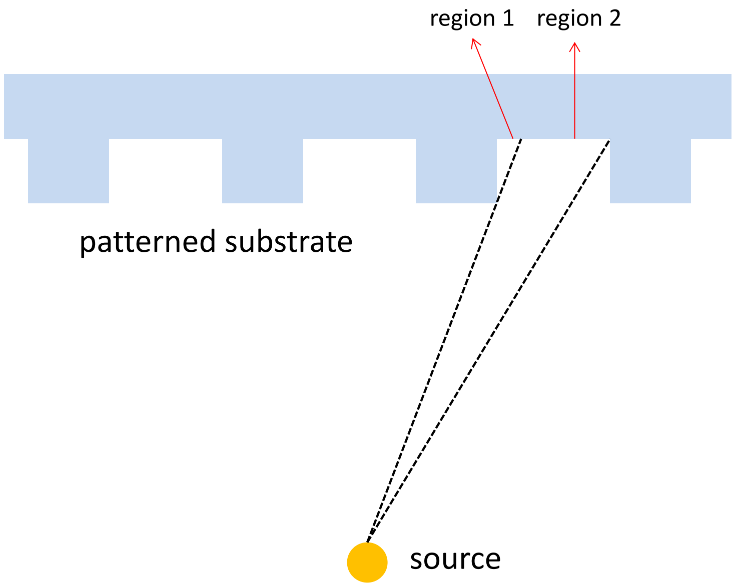

Figure 2- 5 Cartoon illustration of the shadow effect on the patterned substrate.

The overview of our evaporator system is shown in figure 2-6 (a), a Cryo pump with temperature around 10 K maintained by compressing the helium gas was equipped to achieve the vacuum as high as 10^{-8} Torr. Another advantage of the Cryo pump is the high pumping efficiency and it can pump down to 10^{-7} within one hour. A Pirani gauge is installed to monitor the vacuum inside the chamber. A SQM-160 film thickness monitor is utilized to monitor the deposition rate. The principle of the monitor is to use a quartz crystal whose resonant frequency shift is proportional to the materials thickness deposited on it. The deposition rate with accuracy better than 1 Å/sec is attainable by monitoring the resonant shift change. The material parameters such as the material density and the Z factor have to be input for the program before the deposition so that we can measure the deposition rate of each material accurately. Figure 2-6 (b) and (c) show the scenario inside the chamber, there are 4 pairs of electrodes which are controlled by two power sources (power 1 is in charge of the left two, power 2 is in charge of the right two).

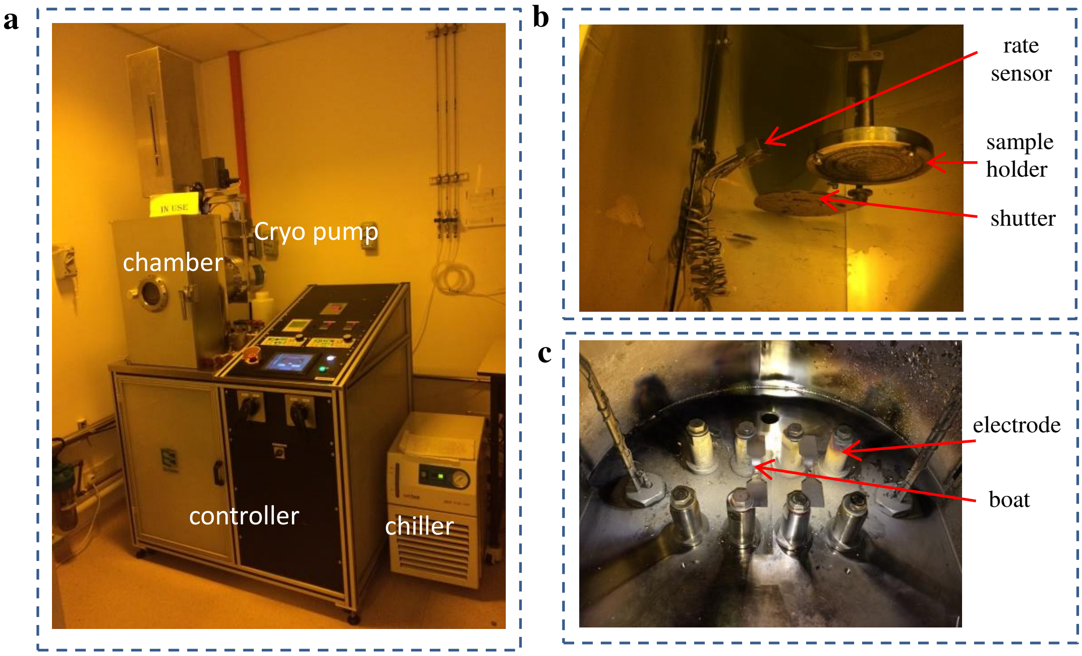

Figure 2- 6 Overview of the thermal evaporator system. (a) image of the whole system (b) the configuration of the sample holder and sensor (c) the setup of the electrode pairs and the boats.

We used a tungsten boat or a rod to connect each pair of electrodes and then a current was applied to melt the metal pellets. Our system enables the deposition of 4 different materials in one process and the isolator was put in between to prevent the material contamination. Usually if we just need to deposit two kinds of materials, we will put the materials on the second and third electrodes as close as possible to reduce the shadow effect. In the thesis, most of the time we just need to deposit one material and an adhesion layer (Cr or Ti). The sample holder is equipped with a shutter to control the deposition and the whole holder can be rotated. A water cooler is applied on both the electrodes and the sample holder to maintain a normal temperature (19 ℃）. Our system is capable of depositing all the commonly used metals, the rate can be adjusted with the minimum 1 Å/sec by adjusting the current correspondingly.

2.1.3 Magnetron sputtering

Sputtering is another typical physical vapor deposition method to accomplish thin film fabrication. It is widely used in industry to directly deposit film on the integrated circuit with excellent uniformity and over large area deposition. All the sputtering processes share the same principle that the material atoms are ejected by exchanging the momentum with other energetic ions when the energetic ions strike on the material target surface. A typical discharge plasma sputtering process can be illustrated by figure 2-7.

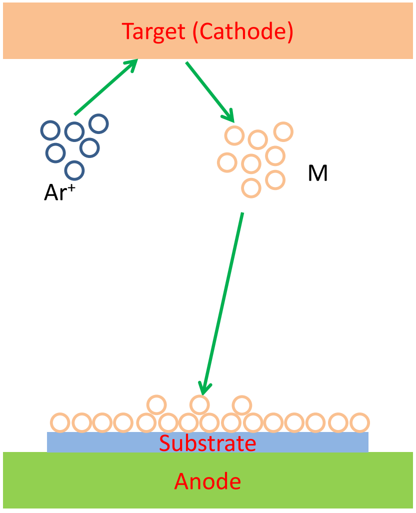

Figure 2- 7 Schematic of the discharge plasma sputtering process.

The substrate is located at the anode side and the target itself serves as a cathode. The sputtering process undergoes in a high vacuum environment and then usually an argon gas was introduced to act as the plasma gas. The argon atom is ionized when the potential in between two electrodes exceeds the threshold. The Ar^+ is attractive to the cathode with a high acceleration and then strikes on the target surface while the electrons from the ionization travel in the opposite direction to the cathode. The motional electrons will collide with the neutral Ar atom and strip the outer electron of the Ar atom to ionize the Ar gas further to produce more Ar^+ and free electrons to repeat the cycle. The energetic Ar^+ with the atomic weight comparable to the material atoms is capable of releasing the atoms from the target surface by exchanging the momentum. The material atoms ejected from the target will travel a distance and finally re-condense on the substrate layer by layer tightly to form a thin film. Sputtering yield refers to the number of atoms released from the target per incident Ar^+ and is dependent on the energy of the Ar^+. It is clear that the deposition rate can be enhanced by increasing the sputtering yield with a higher voltage. Another common method to enhance the sputtering process is to apply an additional magnetic field on the target side. The magnetron sputtering configuration is shown in figure 2-8.

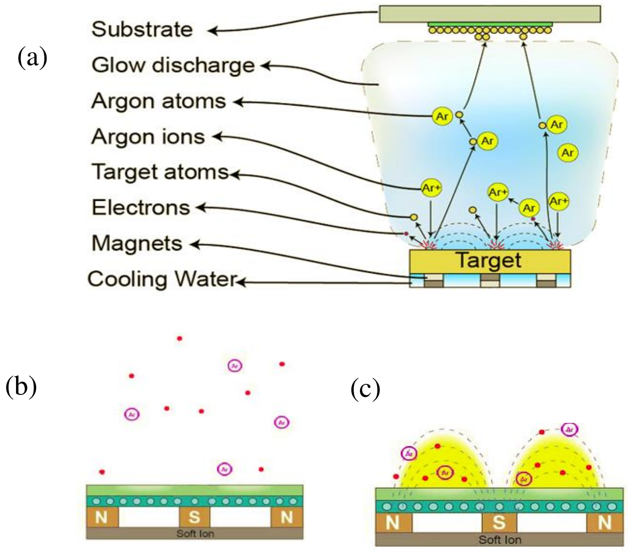

Figure 2- 8 Magnetron sputtering. (a) the overview of the magnetron sputter configuration. (b) and (c) are the motion of electrons and ions in a non-magnetron and magnetron system, respectively. [134]

Figure 2-8 (a) shows the overview of the magnetron sputtering configuration, the only difference from the normal DC sputter is the presence of the magnets on the target side. As figure 2-8 (b) shows, in a non-magnetron sputtering system, although there is a trend that the Ar^+ and electrons are attracted by the cathode and anode respectively, the electrons and Ar^+ propagate at the free space and it is possible for the Ar^+ to hit the substrate to destroy the deposited thin film. Figure 2-8 (c) show that the presence of a strong magnetic field can confined the ions and electrons near the target because a charged particle will do circular motion around the magnetic field axis. The confinement of the Ar^+ near the target can eliminate the collision between ions and the substrate to reduce the substrate damage. In addition, the longer travelling distance of the helical motion of the electrons in the magnetic field produce more intense Ar^+ near the target and enhance the sputtering efficiency as well. The higher deposition rate of the magnetron system can also reduce the impurity introduced during the deposition process. The confinement of the ions and electrons make the plasma possible to be sustained in a low Ar pressure. It is also important to be noted that the sputtered atoms are neutral and will not be affected by the strong magnetic field and behave as the non-magnetron system.

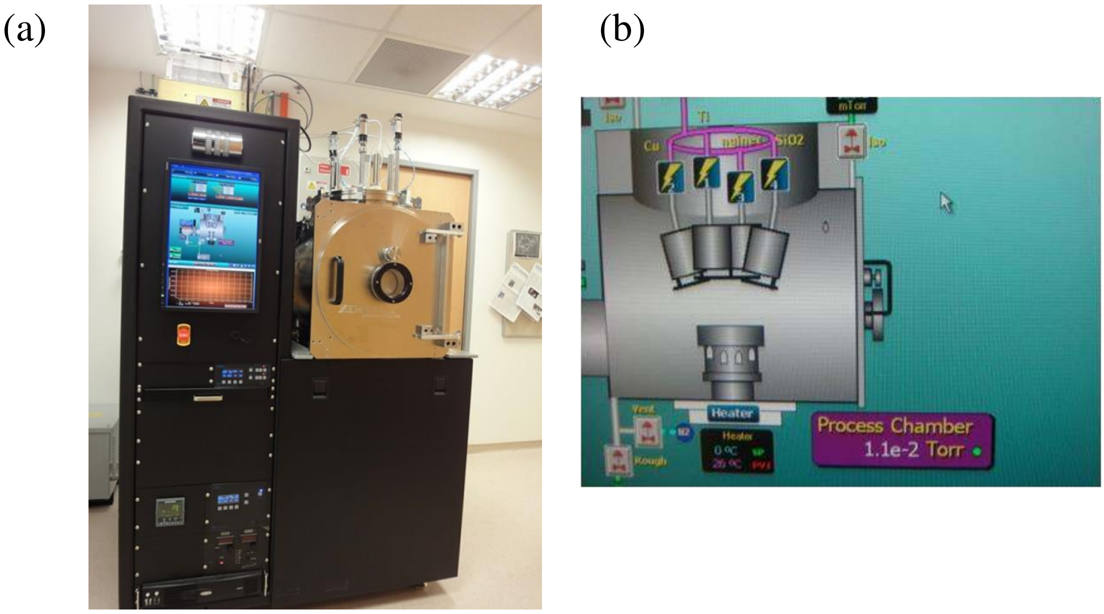

Figure 2- 9 Triaxis magnetron sputtering system from Semicore. (a) the overview of the system (b) the configuration inside the chamber.

The sputter used in this thesis research is a magnetron triaxis sputtering system from Semicore equipment, Inc. as shown in figure 2-9. The system consists of a vacuum system, a chamber, a water cooling system and a controlling system. The vacuum system is equipped with a mechanical pump and a turbo pump. The sample holder is located at the bottom of the chamber with the function of heating and rotating. Three targets are installed above the sample holder with fixed position and the target material is inserted into the cylinder shape target for deposition (figure 2-9(b)). This sputter is capable of depositing a broad range of materials including metals, alloys and dielectrics. Direct current (DC) is applied when depositing a conducting material, while a radio frequency (RF) is necessary when the target materials are electric isolating like the dielectrics and semiconductors. The deposition rate can be alerted by adjusting the applied power and usually it is linearly dependent on the power.

Sputter is capable of depositing a very broad range of materials especially for the high melting point material, which is impossible for the evaporation deposition. In addition, the sputtered material has better adhesion to the substrate and the deposited materials almost have the same composition with the target materials. However, the sputtered sample is not compatible with the lift-off process. In contrast to the re-condensation process in evaporator that the vapor will travel in a straight line to the substrate due to the high vacuum, the ejected material atoms will travel in random directions due to the numerous collisions with the argon ion and argon atom. Consequently, the sidewall is covered by the deposited material to prevent the solution to penetration and lift-off process becomes very challenging. In our lab, we can use the thermal evaporator and sputter complementarily according the purpose of thin film deposition.

2.2 Characterization

2.2.1 Scanning electron microscopy

Scanning electron microscopy is a microscopy technique by scanning the electron beam on the specimen to get the morphologic image. As we know the resolution of the optical microscopy is limited by the diffraction limit and it is impossible to get the resolution down to tens of nanometers. In the nanoscience research, it is a common requirement to take a look at the detail of the morphology of the specimen with dimension of tens of nanometers or even less than 10 nanometers. Besides optical source, electron beam was proven as a good source to construct microscope with resolution down to 1 nm. Based on Louis De Broglie's classic description, the electrons possess the character of particles and wave simultaneously and its wavelength can be defined by $\lambda = h / p$, here h is Planck's constant and p is the momentum of the electron. It is clear see that the wavelength of the moving electron is quite small when the electrons move with high kinetic energy. After adding the correction by including the relativistic effect when calculating the wavelength, the wavelength of the electron is at pm level when it has the energy around 10 keV. The energy of the incident electron in a common SEM system ranges from 0.1 keV to 50 keV, theoretically, we can make the resolution as high as pm. However, the resolution in a real system is around 1 nm due to the limitation of the lens, deflectors and detectors.

The principle of the SEM relies on the interaction of the electrons and the specimen. The interaction of the electrons and the specimen can be simplified by considering the interaction of the electrons and the atoms from the specimen. There are many processes involved when an energetic electron beam strikes on the specimen. Most of electrons are scattered back without energy loss, which are known as back scattered electrons (BSE). The incident electrons can ionize the inner shell of the atom and upper shell electrons jump down to fill the vacancy, as a result, a characteristic X-ray is emitted. Instead of the emission to the out space, the energy of the X-ray can also be transferred to other atomic electron to overcome the work function to produce a Auger electron. At the same time, the energetic incident electrons will kick out some outer electrons of the atom which is known as secondary electron (SE). The maximum energy of the SE is 50 eV, most are around several eV, which makes it convenient to be captured and detected. All those products from the interaction can be utilized to obtain the information of the specimen. For instance, scanning Auger electron microscopy is capable of probing the surface environment and X-ray microscopy is used to study the elemental composition of the specimen. Particularly, the secondary electrons are ejected from the specimen surface within 10 nm depth and they are very sensitive to the specimen morphology. In most of the SEM system, secondary electrons are utilized to image the specimen morphology.

The system we use in this thesis is JEOL 7001F field emission SEM. We usually use 5 keV as the acceleration voltage to avoid the damage to the sample. If the sample is compatible with higher voltage, higher voltage can give higher quality image. Charge effect which refers to the accumulation of the electrons in a nonconductive substrate is a main factor to reduce the quality of the SEM image. The accumulation of electrons on the substrate modifies the interaction between incident electron and specimen and the whole view will be very bright on the computer monitor. It is trivial to capture an image in a conductive substrate such as the ITO coated glass and Si wafer, while for the nonconductive substrate such as a polymer, we should use lower acceleration voltage and shorter scanning time to minimize the charge effect. The 7001F system has the maximum magnification of 1 million and it is capable of taking the image from the top view, tilt view and cross section of the specimen. Figure 2-10 shows two typical SEM images captured from out 7001F system.

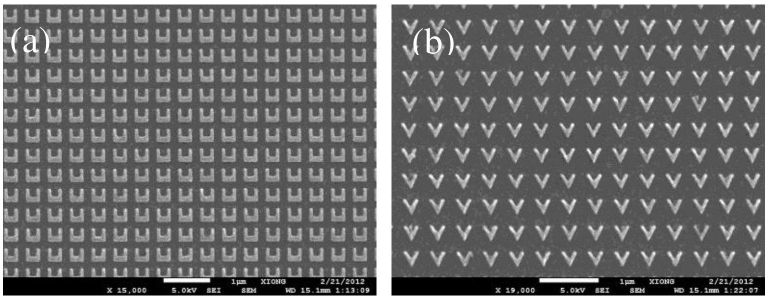

Figure 2- 10 SEM images from 7001F system. (a) U shape resonator array (b) V shape resonator array.

2.2.2 Transmission and reflection microspectroscopy

Spectrum is the plot of the relative intensity of a series of wavelength of electromagnetic wave. Spectroscopy is a science branch to deal with the interaction between a matter and the electromagnetic radiation by analyzing and interpreting the spectrum. One simplest spectroscopy example is the dispersion effect of the white light that it will present colorful light after passing a prism or other thin film. The matter will absorb, reflect or emit the electromagnetic radiation with specific wavelength when the incident radiation is resonant with the matters. In the mechanic physics, the resonance means that the amplitude of an oscillating system is maximized in a certain oscillating frequency. For example, the harmonic oscillator has the largest amplitude when it oscillates at the resonance frequency and it is in the highest energy state. In the quantum mechanics, we treat the atomic or molecular system with some discrete energy levels and the electrons are only allowed to stay at the discrete levels and forbidden in the energy level gap. The transition of electrons between two energy levels will lead the energy absorption or release depending on the energy difference of the initial and the final state. Quantum mechanics also treat the electromagnetic radiation as the wave-particle duality. The light can be treated as a series of particle with the energy which is known as photon. The resonance of the radiation-matter interaction means that the energy of the photon can match the energy difference in two states and can produce a state transition under the selection rule. The quantized energy state of each matter is unique and can be reflected in the spectrum. So, spectroscopy is a powerful method to study the structure, properties of materials. Up to now, a lot of spectroscopy methods have been developed to study the specific materials properties. For instance, the absorption and photoluminescence (PL) spectroscopy can learn the electronic state, the Raman spectroscopy can reveal the vibration of the molecule or lattice, time-resolved spectroscopy is utilized to study the decay rate of an excited state.

Microspectroscopy enables the detection of the spectrum in microscopic area. In the laboratory research or in the industrial application, it is necessary to measure the spectrum of with the size on several microns, such as the behavior of a single bio-molecule, the optical property of the EBL pattern with small area. For the photoluminescence or Raman measurement, it is common to characterize the sample in a small area in the T64000 spectrometer because the diameter of the laser spot is around 1-2 microns and the signal can be collected efficiently. In the case we need to measure the transmission spectrum in a very broad range of wavelength, usually the light source is a lamp and it is not trivial to focus and collect the signal in that small area. In this thesis the equipment we utilized to measure the transmission and reflection is a UV-visible-near infrared microspectrophotometer (CRAIC 20/20 PV$^{\mathrm{TM}}$) from Craic technologies. The overview of this Craic 20 is shown in figure 2-11.

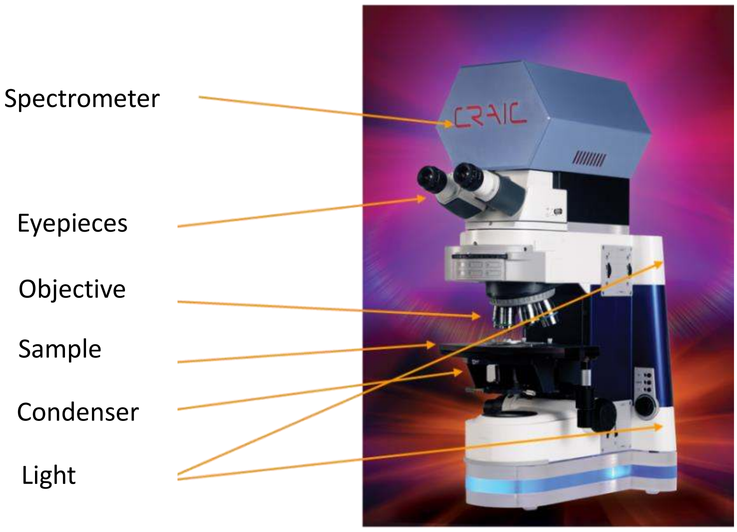

Figure 2- 11 Overview of CRAIC 20 diagram.

Craic 20 is an integrated instrument constructed by building the spectrophotometer into an optical microscope. In this system the microscope is specially designed and its optics components can operate in UV and near infrared range which is impossible for a normal optical microscope. The function of the optical microscope is to amplify the sample image for the convenience to locate the small sample. The objective is specially designed to collect the signal from the sample and focus it onto the aperture of the spectrophotometer, the digit imaging system can display both the image of the sample and the aperture simultaneously and the location of the aperture indicates the area we are measuring (Figure 2-12).

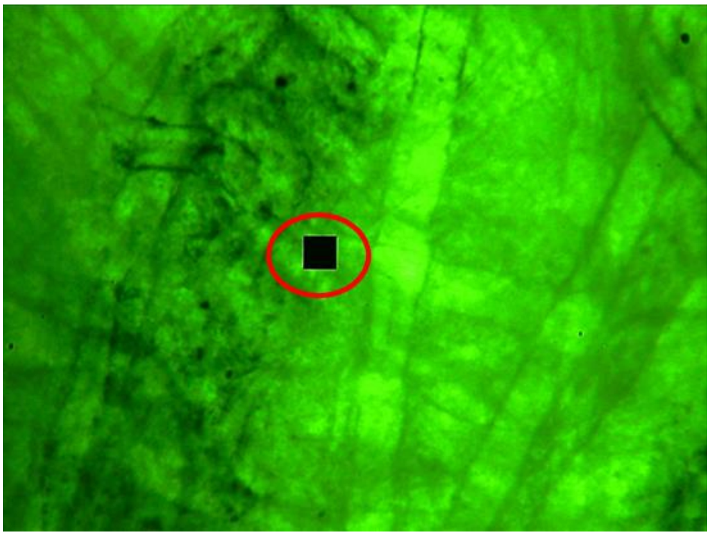

Figure 2- 12 Aperture image on a sample.

There are 6 aperture size in this microspectrophotometer, under 36×reflective objective, the smallest size is 1.7×1.7 microns and the largest size is 33.6×33.6 microns. Craic 20 is capable of measuring the transmission, reflection and the absorbance. When measuring the transmission and the absorbance, the light comes from the bottom lamp and the condenser will focus the light on the sample, subsequently the light transmitted is collected by the objective. While for the reflection measurement, the light comes from the top lamp and strikes on the sample, the reflective light will be collected by the objective. The principle of the transmission and reflection measurement is indicated in figure 2-13.

No matter in the transmission or reflection measurement, the signal light collected by the objective will encounter a grating so that the light with different wavelength will separate. The CCD detector can measure the intensity of light at each wavelength and the relative intensity can be displayed in the software. The CCD in Craic 20 is constructed by combining two different range detectors together, the first detector cover the UV-visible range (300-900 nm) while the second one cover the near infrared range (900-2100 nm).

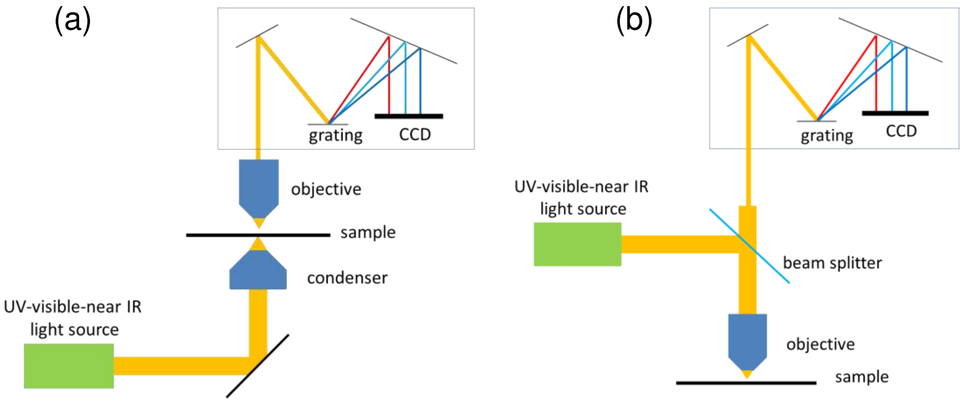

Figure 2- 13 Schematic of the measurement principle in Craic 20 system. (a) light path in transmission or absorbance measurement. (b) light path in reflection measurement. (Numerical Aperture of the objective is 0.5)

In our system, both the transmission and the reflection we obtain are the relative percentage refers to the scanning on the area without the sample as the expression shows

$$C = \frac{S - D}{R - D} \qquad (2\text{-}3)$$

here C means the transmission or reflection, D is the dark scan, S and R are the sample scan and reference scan respectively. Usually the dark scan is proportional to the scanning time and it will reduce the dark signal effect with shorter scanning time. The noise can be reduced significantly if the intensity R and S is much larger than D, otherwise, the spectrum will be presented with a lot of noise. So, it is critical to align the light path well to make the incident intensity as high as possible. The absorbance of the sample can be obtain with the formula

$$A = -\log(I / I_0) \qquad (2\text{-}4)$$

here I_0 is the intensity of radiant energy striking on the sample, I is the intensity of energy emerging from the sample. Actually I and I_0 are the intensity S and R we obtain respectively in expression 2-3 in the transmission measurement mode. The calculated absorbance will be displayed in the software after every measurement.

This Craic 20 microspectrophotometer is nondestructive instrument because the light from the Xenon lamp almost has no damage to the sample. In addition, the measurement efficiency is very high, it just takes several seconds to finish a spectrum measurement. We also can integrate a polarizer into this system to polarize the incident light to accomplish the polarization dependence measurement.

2.2.3 UV/Vis/NIR spectroscopy

It is critical to get the absolute reflection (absorption) of one thin film coating. For example laser mirrors are designed to have zero absorption at one certain wavelength, it is necessary to measure the absolute reflection accurately to qualify the absorption. Also for the application of thin film in energy harvesting, one needs to measure the absolute reflection to qualify the property of the thin film of interest. Though the Craic 20 spectrophotometer we introduced above can measure reflection at microscopic area, the result is relative reflection instead of absolute reflection. Furthermore, all the measurement in Craic 20 is accomplished with normal incidence and the angle resolved measurement is not attainable. Here we introduce a lambda 950 UV/Vis/NIR spectrometer (PerkinElmer) to measure the absolute reflection as the complementary to the Craic 20. This spectrometer is capable of measuring the absorbance, total reflectance (sphere integration) and absolute reflection by utilizing the corresponding accessory. Herein we focus on the measurement of the absolute reflection by installing a universal reflectance accessory (URA).

Figure 2-14 shows the schematic of the optical system. The spectrometer features as a two –monochromator system. The deuterium lamp provides the radiant source in UV range while the tungsten lamp covers the visible-near infrared range. After passing two monochromators, the exiting light exhibits high spectrum purity and low stray component. Subsequently, the beam is separated into a reference beam and a sample beam with identical intensity. The reference beam serves as the signal of the reference measurement so that it is capable of obtaining the absolute reflection. There is a mirror can rotate to select the detector, a photomultiplier tube (PMT) is used to cover UV-visible range while a lead sulfide (PbS) detector is used in near infrared range.

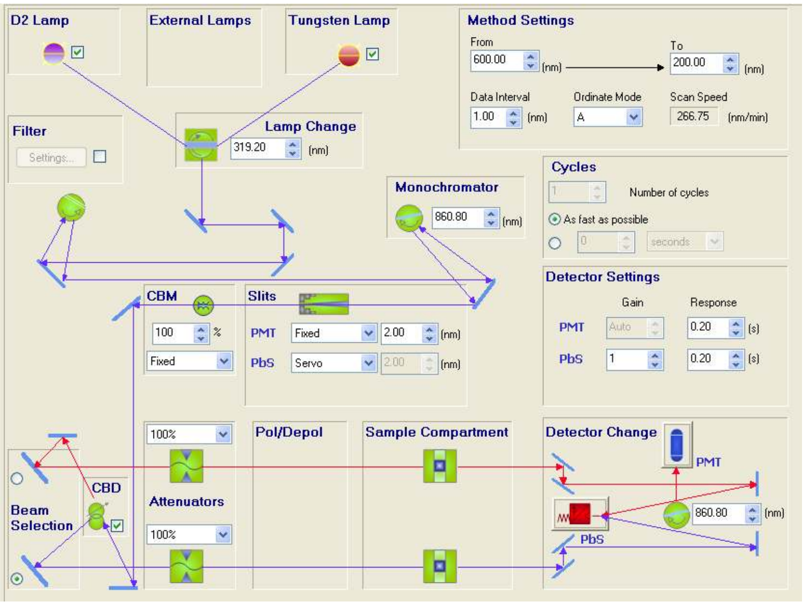

Method Settings
From 600.00 (nm) → To 200.00 (nm)
Data Interval 1.00 (nm)
Ordinate Mode A
Scan Speed 266.75 (nm/min)

Lamp Change 319.20 (nm)

Monochromator 860.80 (nm)

Cycles
1 Number of cycles
● As fast as possible
○ 0 seconds

Detector Settings

	Gain	Response
PMT	Auto	0.20 (s)
PbS	1	0.20 (s)

CBM 100 %
Fixed

Slits
PMT Fixed 2.00 (nm)
PbS Servo 2.00 (nm)

Attenuators 100%
100%

Detector Change 860.80 (nm)

Figure 2- 14 Schematic of the lambda 950 optical system.

The absolute reflection is accomplished as the process shown in figure 2-15. The reference beam is guided to the input mirror and then directed to the detector directly without passing the sample, while the sample beam strikes on the sample by adjusting the angle of the mirror and then the position of the detector will adjusted correspondingly to collect the signal. Clearly, the incident angle with respect to the sample normal line can be changed by rotating the input mirror to implement the angel resolved measurement. In this system, the angle between the incident light and the normal line can be adjusted between 8°-65° with the accuracy of 1°. If we want to measure the reflectance of the same sample at different angle, the reference should be taken individually at every angle. While if we want to measure the reflectance at the same angel of different samples, we just need take the reference for one time. The cross section size of the radiant beam is dependent on the width of the slit. The beam is approximately around 4.5 mm×4.5 mm at the slit width with 5 mm and the width can be reduced further to make the radiant beam smaller. In addition, a common beam mask (CBM) is added to restrict the cross section of the incident beam and it is possible to make the incident spot as small as 1mm×1mm.

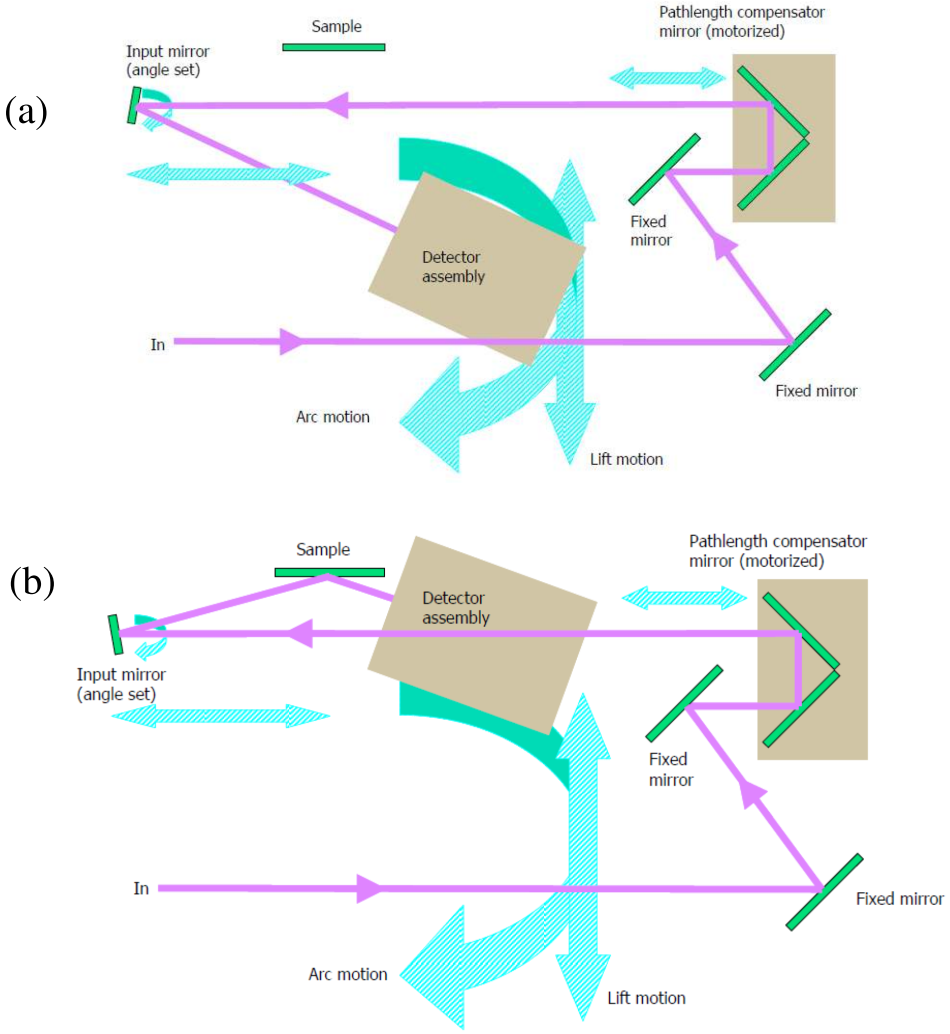

Figure 2- 15 Reference scan and sample scan. (a) reference beam signal is collected by the detector directly (b) the sample beam is directed to the sample and the output signal is collected by detector.

2.2.4 Raman spectroscopy

All the Raman spectroscopy in this thesis was carried out in a commercial micro-Raman spectrometer (Horiba Jobin Yvon T64000) with a backscattering signal collection configuration, which was equipped with a liquid nitrogen cooled charge coupled detector with the detection range from ultraviolet to near infrared. Overview of the Raman spectrometer is shown in figure 2-16 where the main components are labelled. The whole system is installed in an optical table to reduce the vibration and also guarantee the flatness of the external optics. The microscope, the spectrometer are integrated together. If necessary, it is also possible to add a cryostat, pump and a temperature controller to accomplish the low temperature measurement.

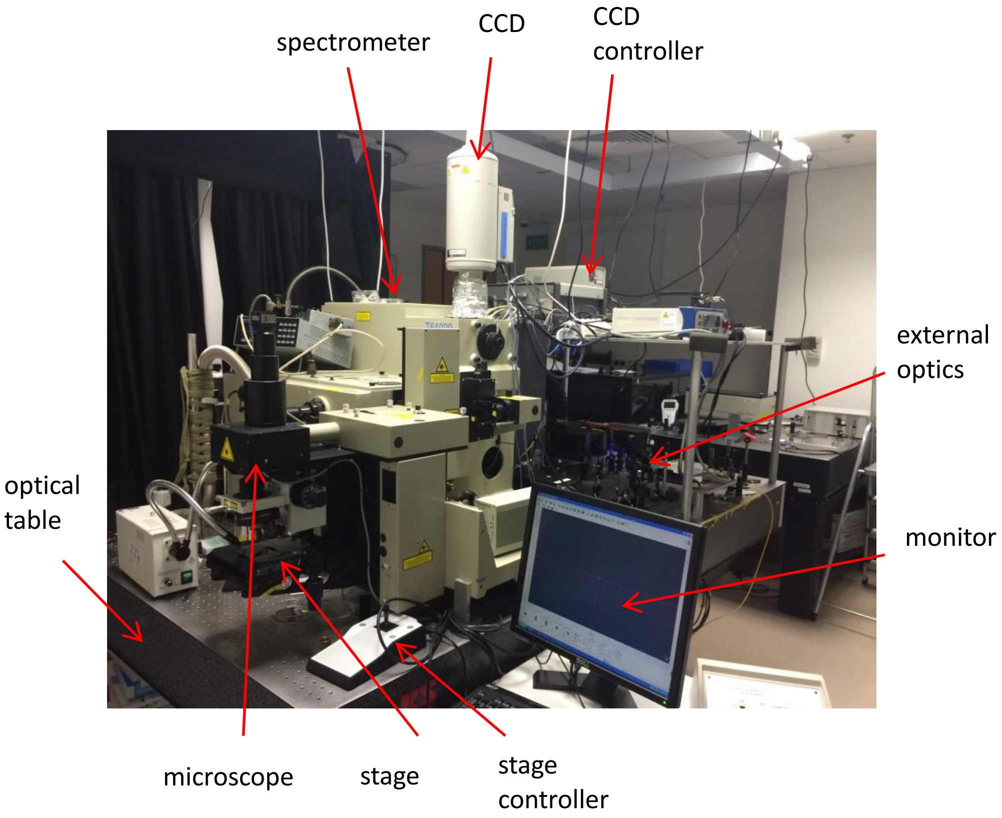

Figure 2- 16 Overview of T64000 Micro-Raman spectrometer.

The optics system of the Horiba-JY T64000 is shown is figure 2-17. One main characteristic of T64000 is that three gratings are equipped to make the subtractive mode available to measure the low frequency Raman. The Raman measurement is accomplished with a single wavelength laser which is well aligned before striking on the sample.

It will be better to make the light beam as small as possible and align the laser beam on an absolute flat surface. Also the power of the laser can be adjusted by adding an attenuator. The laser beam is guided into the microscope after passing through a beam splitter (BS) and subsequently strikes on the sample below the microscope. The diameter of the laser spot is dependent on the objective and usually the diameter of the laser beam is around 1 μm under a 100× objective. The backscattering signal is collected by the objective and then passes through the beam splitter and a pinhole. The function of the pinhole here is to adjust to volume of the light to be collected based on the laser diameter, sample size and also eliminate the stray light. The Horiba-JY T64000 can operate at either single mode or subtractive mode. For a single mode, the backscattered signal is guided to the third grating directly and dispersed to the CCD after passing a notch filter.

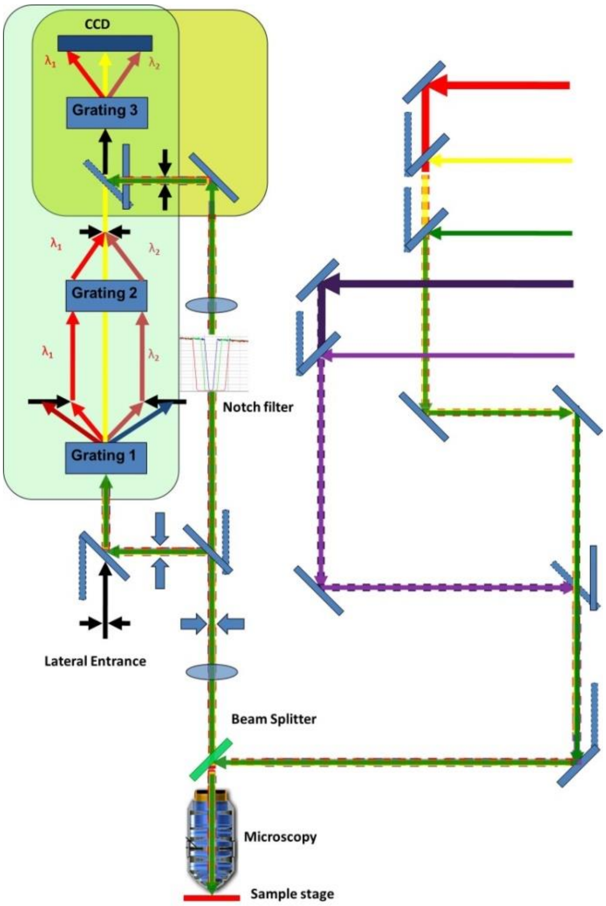

Figure 2- 17 Schematic of the optics system of T64000 Micro-Raman spectrometer.

As we know majority of the scattering between light and a matter is Rayleigh scattering with no energy shift. The notch filter here is used to block the Rayleigh scattering signal, otherwise it is impossible to obtain a clear spectrum, even worse the CCD will be damaged due to the high intensity of the Rayleigh scattering. The conventional method by combining a spectrometer and a notch filter has the detection limitation of 50 cm^{-1}. However, a subtractive mode enables the detection less than 10 cm^{-1}. In the subtractive mode, the scattered signal passes through two additional gratings instead of a notch filter before entering the third grating. The first and second grating known as the double pre-monochromator serve as the notch filter to exclude the unwanted frequency signal. In our lab, more than ten laser lines are available to cover the range from ultraviolet to near IR, in addition, two tunable laser ranges from 700-990 nm (Mattisse Ti-sapphire) and 650-780 nm (Mattisse Dye laser with Rhodamine 6G) are available to provide more choices for our measurement.

Chapter 3 Integration of Metamaterials to Polymer-Flexible Metamaterials (Metaflex)

3.1 Introduction

3.1.1 Flexible metamaterials (Metaflex)

Integration of electronic, photonic and plasmonic components onto a flexible and transparent substrate opens the door for the next generation novel devices which are portable, flexible, stretchable and transparent. Compared with the devices on the rigid substrates like glass or silicon, devices integrated on a flexible matrix provide the advantages such as the transparency, light-weight, deformability, low-cost and biocompatibility. In addition, devices fabricated on a flexible matrix have more freedom to be integrated or combined with other devices. For example, stretchable devices can be integrated to a device with a curve surface just by simply covering the flexible matrix on it and it will adjust the shape automatically, which is not accessible with a rigid substrate. Another reason preventing the integration between two rigid devices is that the rigid substrates are usually non-transparent and present with high electrical and optical losses, subsequently making the connection between two rigid substrates difficult. The biocompatibility is another vital character of the flexible devices. The non-toxic and soft polymer is usually an organic material and compatible with the biomolecules. Cells can grow and reproduce on a polymer, such as PDMS media, which is not possible on rigid inorganic substrates. It is even possible to be integrated to the human tissue or skin to serve as a sensor or monitor, making the flexible devices huge potential in the medical applications. Recently, many research efforts have been dedicated to the flexible devices and many novel devices have been demonstrated with outstanding properties over the rigid devices. For instance, nanopillar-array solar cell device based on PDMS is cost-effective and perform with acceptable efficiency, what's more, the performance can be modified by applying a strain to induce the bending, suggesting the huge potential of this transparent device on the application of energy harvesting,[135] high performance paper like display was demonstrated by fabricating the transistors on the polymer directly and the performance can be maintained even bend the polymer into 1 cm radius, this display provides an avenue towards the electronic system on a plastic,[136] a chemical and biological sensor was implemented by transferring the highly-ordered silicon nanowires onto a plastic, this novel device open the opportunities for the wearable and portable sensors,[137] macroscale active system by integrating of the nanowire array on to a mechanically substrate was utilized to serve as a pressure sensor, the artificial skin enable the application of implantable sensor or monitor.[138]

Attaching a metamaterial on to a flexible, transparent and stretchable substrate is also of significant interest. First of all, the flexible metamaterials enable the implementation of 3D metamaterials. As we know, the implementation of bulk metamaterials is critical in the transition from scientific research to the practical application. One strategy to fabricate 3D metamaterials is to utilize the multiple steps electron beam lithography to stack the metamaterials layer by layer and a dielectric was added in between the gaps. In this electron beam lithography method, it is very challenging to align the meta atoms in the multiple lithography processes and the throughput is very limited and it is also impossible to implement it in large scale. However, the flexible metamaterials provide an opportunity to construct the 3D metamaterials by simply staking the polymer layer by layer.[139] The meta atoms are fabricated on a polymer first and then stack them together to form a bulk metamaterials. Because the polymer is lossless and the thickness can be adjusted, it is possible to make sure that the metamaterials can interact with the adjacent layer to perform as a bulk metamaterials. The feasibility of adjusting the distance between adjacent layers and changing the orientation of each layer make it very convenient to engineer the coupling and modify the properties of the artificial bulk metamaterials. It is even possible to reuse these same layers to assemble in another configuration to change the bulk metamaterials properties totally. Secondly, the flexible and transparent substrate can lower the permittivity thus reduce the dielectric loss. For silicon or glass, majority of the electric flux is concentrated in the substrate due to its high permittivity and the loss is very high. One immediate consequence is that the high loss will lower the sensing frequency. The majority of the electric flux is confined inside the substrate and cannot interact with the analytes located on the air side so that the resonance shift will be reduced. The transparent substrate can redistribute the electric flux and more electric field will be confined in the air side to interact with the attached analytes to attain higher sensitivity, imposing a symmetric electric flux inside and outside the substrate. Thirdly, the integration of flexible and deformable substrate with metamaterials can produce an active metamaterial. The properties of the metamaterials are fixed at the moment when we finish the fabrication on a rigid substrate. However, the properties of the metamaterials fabricated on a flexible substrate or embedded into a flexible and transparent media can be tuned and engineered by changing the coupling distance between two elements by applying a strain. The resonance frequency will shift depending on how much strain applied and it will return the initial state after releasing the strain. The tunable resonance frequency has significant in the surface enhanced Raman scattering and the surface enhanced infrared spectroscopy.[140, 141] In addition, the ability of wrapping promotes its application in food safety monitoring, such as detection minute residue of pesticides, plasticizers or other environmental contaminants or hazards. This is particularly attractive for any food or fruits with non-planar surfaces. This detection method is convenient, non-destructive and can implement the detection *in situ* to monitor the local change simply by monitoring the reflection spectrum or surface enhanced Raman scattering which provide chemical fingerprint information.[142]

3.1.2 Review of the fabrication of Metaflex

In contrast to the fabrication on a rigid and flat substrate, the fabrication of metamaterials structures on a deformable, nonconductive substrate is non-trivial, especially when the feature size is down to tens of nanometers. This is because polymer is usually not compatible with the lithography process due to the fact that resist and solvents involved in the fabrication are likely damage the polymer due to chemical activities. In addition, the softness and non-conductivity surface make it impossible to use electron beam lithography due to the charge effect. Two kinds of methods have been reported in literature to implement the fabrication of Metaflex on to a polymer or plastic, which were the direct patterning and the pattern transfer method.

As same as the direct patterning on a rigid substrate, the direct pattering method requires that the resist is spin-coated on the polymer and then define the structure on the resist with ultraviolet light or electron beam followed by a metal deposition. The fabrication of terahertz metamaterials on a free-standing highly flexible polyimide substrate has been demonstrated by using direct laser writing.[143] In that direct pattering process, the polyimide should be put on a silicon substrate to avoid the deformation during the wring process and then peel off from the silicon substrate after the metal deposition. This method could make the sample as large as 2 inch in diameter. However, the drawback was that it can only be applied to accomplish the terahertz metamaterials with the line width around 4 μm, still quite far away from visible-near infrared range operation which requires feature size down to tens of nanometers. It was reported that the direct electron beam lithography on a plastic polyethylene naphthalate (PEN) was capable of making the line width down to 30 nm and resonance was accessible to 542 nm. The success of this EBL process is because that PEN is a kind of plastic and it is not as soft as polymer. We can deposit an ITO layer on it by sputtering to eliminate the charge effect, making it compatible with the EBL process. Apart from a plastic, we also desire to fabricate the metamaterials on a thinner and more flexible polymer to broaden its application. However, it will become more challenging to fabricated metamaterials on a polymer such as PDMS, mainly because softness make it difficult to define the structure accurately.

Alternatively, transfer method is available to fabricate the metamaterials on a more soft and flexible matrix. All the transfer method share the principle that the tiny metamaterials structure are fabricated on a rigid and flat substrate and then transferred to the desired flexible matrix with a certain strategy. One direct peel-off transfer from the donor substrate to the receiver substrate relies on the fact that the structure has better adhesion to the receiver substrate. For instance, if the nanowires residue on the silicon substrate are more adhesive to the PDMS, we can coat a PDMS layer on the top and the nanowires will be transferred to the PDMS directly after peel-off the PDMS from the silicon substrate.[144] However, this peel-off method is not universal because it is highly limited by the surface property of the donor substrate, structure and the receiver substrate. There is another method which is known as the soft lithography in which structure is replicated by using a mold, stamp or masker. A mold or stamp (usually it is PDMS) was firstly formed by using the lithography method, subsequently make the mold contact with the desired substrate and replicate the pattern on the mold onto the desired substrates. In the photo nanoimprint lithography, a hard mode (usually it is silica) is applied for the UV light to cross link the polymer. In this nanoimprint method, the pattern on the mold or stamp can be transferred to any substrate of interest. The mold and stamp can be reused for the next round fabrication. However, the pattern size of the soft lithography is usually limited in the micrometer range and the process is quite complex. It consists of multiple steps including transfer the pattern from the resist to the PDMS to form a mold and subsequently transfer the pattern on the mold to the desired substrate. The final feature size is determined by the size of the initial pattern on the mold and stamp. The multiple steps required in the soft lithography will reduce the pattern resolution and accuracy. What's more, the effectiveness of this method depends on the pattern materials and the choice of the substrate, which will recede the versatility of this method. Another remarkable transfer method is to utilize a sacrificial layer, in which the structures are fabricated on the top of the sacrificial layer first and then transferred to the receive substrate by removing the sacrificial layer such as by etching or chemical reaction. Pryce and Aydin *et al.* have demonstrated the transfer of near infrared metamaterials from silicon substrate to PDMS by treating the silicon as the sacrificial layer.[140, 141] In their method, the metamaterials are fabricated on the silicon substrate and then coat a PDMS on to top, reactive ion etching (RIE) was applied to etch the silicon wafer from the bottom side and finally the metamaterials will left in the PDMS after all the silicon is removed. The drawback of that method is that RIE is very time-consuming and expensive. In addition, it needs to control the etch rate and time accurately to avoid the over etching or insufficient etching. Furthermore, a chemical (3-mercaptopropyl trimethoxysilane) was necessarily to be added between the gold structure and PDMS to strengthen the bonding between them, otherwise the structure will be removed due to the bonding strength between the structure and silicon substrate.

In this thesis, we demonstrate a transfer method by utilizing nickel (Ni) as a sacrificial layer to transfer the visible-near IR metamaterials to the thin PDMS polymer. The detailed process will be discussed in the next section. Our method can transfer the pattern with attribute size and feature fabricated on the nickel layer and the transfer yield is almost 100% without any pattern damage and distortion. Additionally this method is convenient, simple and cheap because it only needs to immerse our chip into a hydrochloric acid to remove the sacrificial layer and no further surface modification is required, then the pattern will be embedded inside the PDMS automatically. In the next section, we will also explore the sacrificial of silicon dioxide and then compare it to the nickel sacrificial layer.

3.2 Fabrication

Our purpose is to transfer visible-near infrared metamaterials to the PDMS matrix because PDMS has excellent mechanic properties and biocompatibility. In this section, we will explore two kinds of sacrificial materials which are SiO_2 and Ni. For the SiO_2 sacrificial layer, we can transfer the metamaterials to the Poly(methyl methacrylate) (PMMA) substrate smoothly while it is impossible to transfer the same pattern to Polydimethylsiloxane (PDMS) in the same condition. We will compare the different properties of PMMA and PDMS to find out the mechanism behind it. We argue that the presence of the deflection effect arising from the strong bonding strength between PDMS and silicon prevent the etching of the SiO_2 sacrificial layer. Then we propose another sacrificial layer (Ni) to eliminate the deflection effect completely so that can transfer the metamaterials to PDMS successfully.

3.2.1 Transfer pattern by using SiO_2 sacrificial layer

Our first proposal is to use the SiO_2 as the sacrificial layer for three reasons. Firstly, there are many commercial thermally oxidized SiO_2/Si wafers with various thickness of oxide layer and it is convenient to make use of them directly. The second reason is that charge effect will not arise during the EBL writing because the underneath Si layer is conductive enough to remove the electrons accumulating on the surface, so that SiO_2/Si wafer is compatible with EBL process. Lastly, the SiO_2 layer can be removed readily by immersing the chip into the hydrogen fluoride (HF). In this method, the split ring resonator (SRR) arrays are fabricated on the commercial SiO_2/Si wafer directly with a standard EBL process as introduced in the chapter 2. The thickness of SiO_2 layer we use is around 300 nm. After the fabrication of metamaterials on SiO_2/Si wafer, PMMA A9 (Microchem, USA) is spin coated on the top of the substrate with the spin rate of 4000 rpm and then curried on the hotplate with 180℃ for 20 mins. The thickness of PMMA is around 1.5 μm. The whole structure configuration is illustrated in figure 3-1 after coating PMMA. The residual PMMA on the lateral wall should be removed before immersing it into HF solution so that the HF can penetrate into the SiO_2 layer to finish the etching.

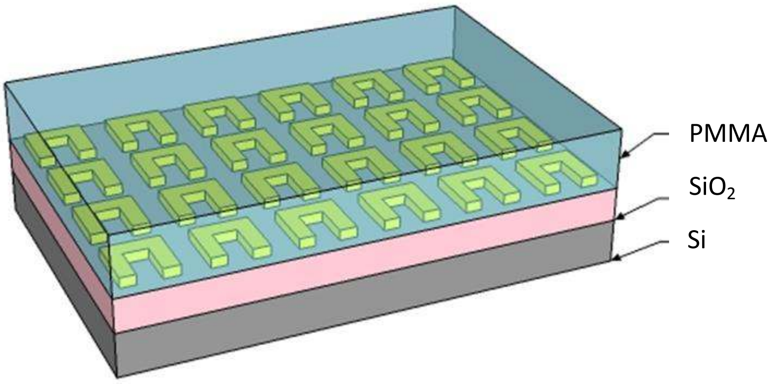

Figure 3- 1 Schematic of the structure after coating a PMMA layer.

The HF solution used is a buffered HF with the same PH value. The chemical reaction between HF and SiO_2 (SiO_2+HF→SiF_4↑+H_2O) is responsible for the etching of the SiO_2. Because SiF_4 is volatile so that we can observe some bubbles produce in between the PMMA and the SiO_2/Si wafer. The time needed for the complete reaction of SiO_2 depends on the area of the SiO_2/Si wafer we used. The PMMA layer will separate from the SiO_2/Si wafer automatically when all the SiO_2 is removed and float on the HF solution. The metamaterial are embedded in the PMMA after checking the PMMA with optical microscope and the SEM as show in figure 3-2. The contrast in the SEM image is not homogeneous and many part is very bright, which arises from the insulating properties of the film. We have to use the lowest acceleration voltage and relatively high scanning speed to capture the SEM image directly from the PMMA layer. As shown in figure 3-2b, the pattern can be transferred completely without any damage.

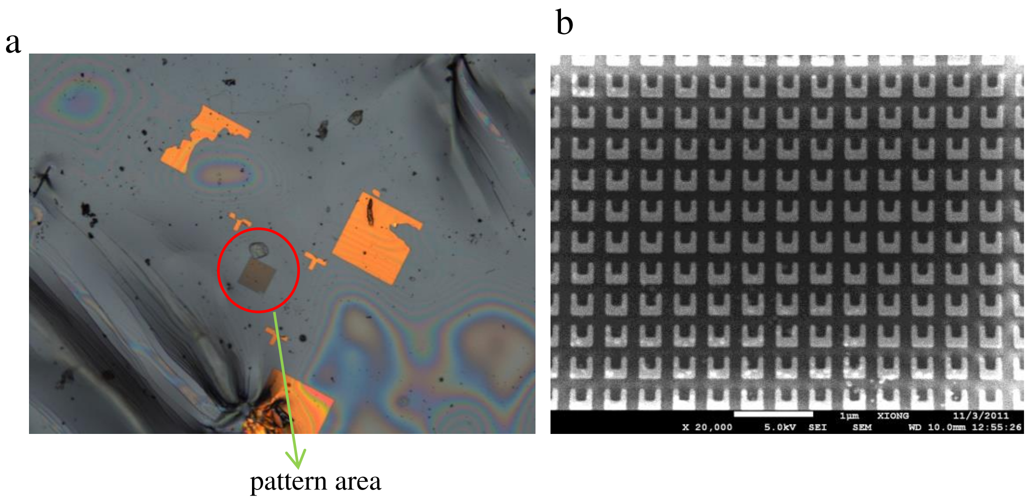

Figure 3- 2 Images of the metamaterial on PMMA (a) optical image of the transferred pattern on PMMA, the red circle indicated the patter area (50 ×50µm) and another three squares are marker. (b) the SEM image of the pattern by zooming in the red circle in (a).

It is good news that we can transfer the metamaterials on to the PMMA. However, PMMA film is brittle and reactive to many other chemicals. It is desired to transfer the metamaterials on to a thin, flexible and compliant PDMS substrate. PDMS has excellent mechanical properties and it is a silicon rubber after curing, which makes it popular to serve as a mold, stamp or mask in the soft lithography. In general, PDMS is non-toxic, non-reactive, non-flammable and transparent. In addition, its biocompatibility makes it attractive in biological applications such as the cell culture and the bio-sensor.

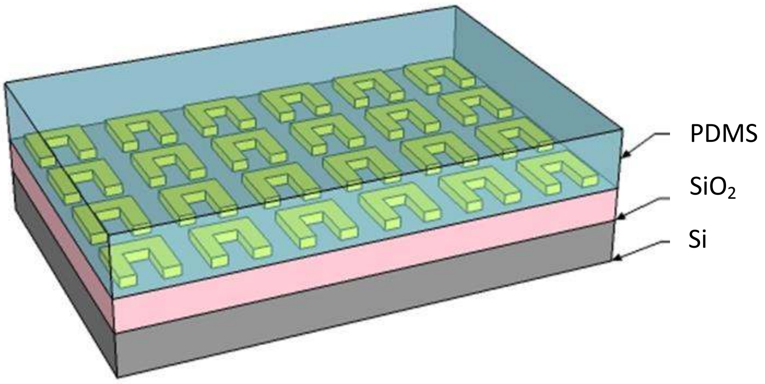

Figure 3- 3 Schematic of the structure after coating a PDMS layer.

PDMS precursor was prepared by mixing the curing agent and Sylgard 184 silicon elastomer with a weight ratio of 1:10, the precursor was spin coated on the top of the substrate after stirring and degassing completely, followed by a curing treatment in the oven for 2 hours at 100℃. The mechanical property can be adjusted by changing the ratio between the curing agent and the silicon elastomer. The thickness can be controlled from hundreds of micrometers to sub 5 μm by adjusting the spin rate and duration. We propose to use the SiO_2 as the sacrificial layer to release the metamaterials pattern from the rigid substrate to PDMS as same as PMMA (figure 3-3). However, this method did not work for PDMS though we just replaced the PMMA layer with a PDMS layer and all other condition and process were kept the same. What we observed was that only a small fraction of SiO_2 on the edge can be etched and the SiO_2 at the central area remained there even after immersing it in HF for many days.

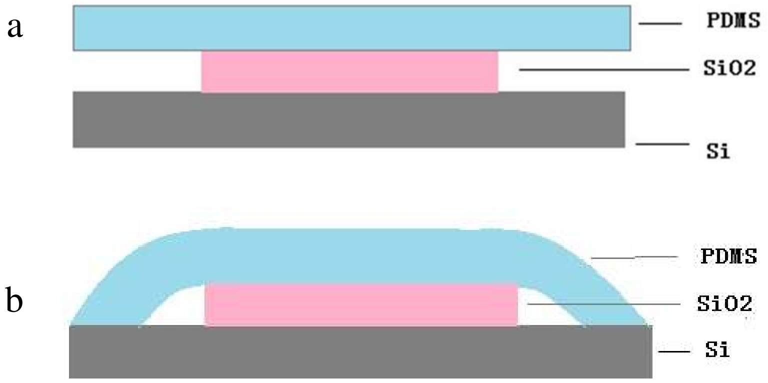

Figure 3- 4 Deflection effect during the PDMS release. (a) schematic of the scenario when the SiO_2 on the edge is etched and a gap is created between PDMS and Si. (b) the suspending PDMS on the edge region will collapse and then contact to the Si substrate tightly to prevent the HF penetration further.

Our assumption was that the HF cannot penetrate into the central area to remove SiO_2 further even for a 0.5 ×0.5 cm substrate. We argue that this penetration problem arises from the deflection effect in which a gap was created once the SiO_2 on the edge was removed and the PDMS was prone to collapse to contact the underneath Si layer to prevent the HF penetrating further (figure 3-4).[145] Figure 3-4b shows that the central SiO_2 is isolated from the outside environment and the chip is impossible to be etched completely. The reason why the deflection is so prominent for PMDS while absent for PMMA is because of the strong bonding strength between PDMS and Si.[146] The silicon element in the PDMS can bind to the Si substrate to form the Si-O-Si bonding which is quite strong. It is the firm contact between PDMS and Si gives rise to the deflection effect.

There are three methods to eliminate the deflection effects. Firstly, we can use a thicker sacrificial layer to create a bigger gap between the polymer and the substrate, making it more difficult for the polymer to contact with the substrate to stop the etching. Secondly, we also can add an intermediate layer on the sacrificial layer to absorb the solution and then guide the solution into the sacrificial layer to finalize the etching. The most effective way is to choose another sacrificial layer material. Herein, we will explore nickel as a sacrificial layer to eliminate the deflection effect completely.

3.2.2 Transfer pattern by using Ni sacrificial layer

Here we propose to use Ni as a sacrificial layer because the Ni layer will separate from the SiO_2 layer automatically in the presence of the water.[147] The fabrication process flow is shown in figure 3-5. 300 nm Ni layer was deposited on the commercial SiO_2/Si substrate (with 300 nm oxide layer) by thermal evaporation

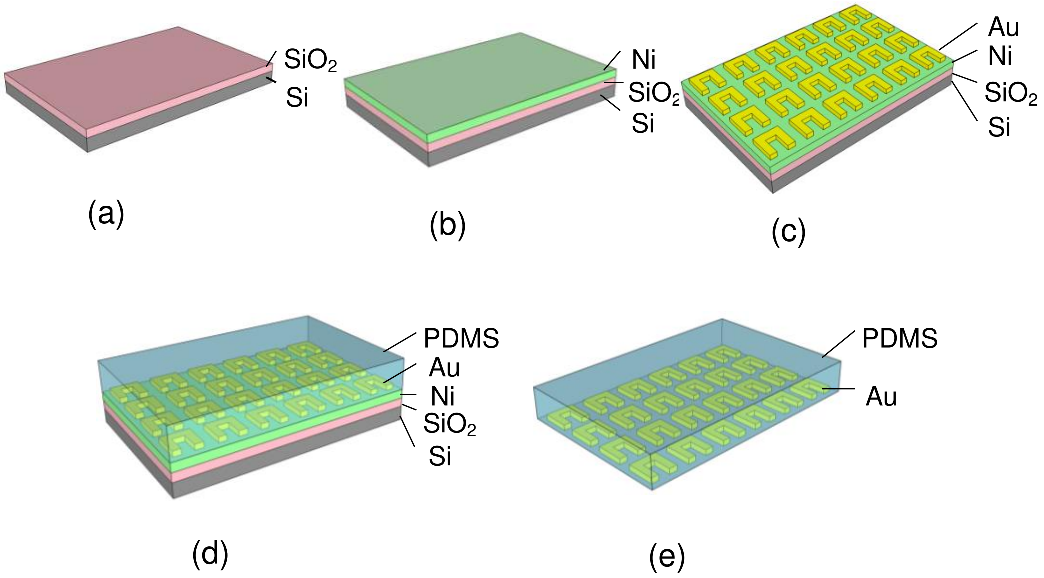

Figure 3- 5 Illustration of the transfer process based on Ni sacrificial layer. (a) commercial SiO_2/Si substrate with 300 nm oxide layer. (b) deposition of 300 nm Ni on SiO_2/Si substrate by thermal evaporator. (c) the direct fabrication of metamaterials on Ni (d) coating of a PDMS on the top of the chip (e)PDMS is released from the rigid substrate and the metamaterials are embedded in PDMS.

(figure 3-5b), subsequently the pattern was written on the Ni directly because Ni is conductive and compatible with the EBL process. After the EBL patterning, 30 nm Au with 2 nm Cr as adhesion layer were deposited to form the metamaterial structure and the metamaterials structure was obtained after a standard lift-off procedure (figure 3-5c). PDMS layer (prepared as described in previous section) was coated on the top of the chip (figure 3-5d) and then immersed into HCl solution (dilute the 37% commercial HCl with water by the volume ratio of 1:4) to etch the sacrificial layer Ni. The reaction $HCl + Ni \rightarrow NiCl_3 + H_2\uparrow$ was responsible for the etching of Ni layer. PDMS will release completely from the substrate and the metamaterials were embedded in the PDMS (figure 3-5e). The deflection effect was absent in this case and the Ni can be removed with several hours for one 1 ×1 cm chip.

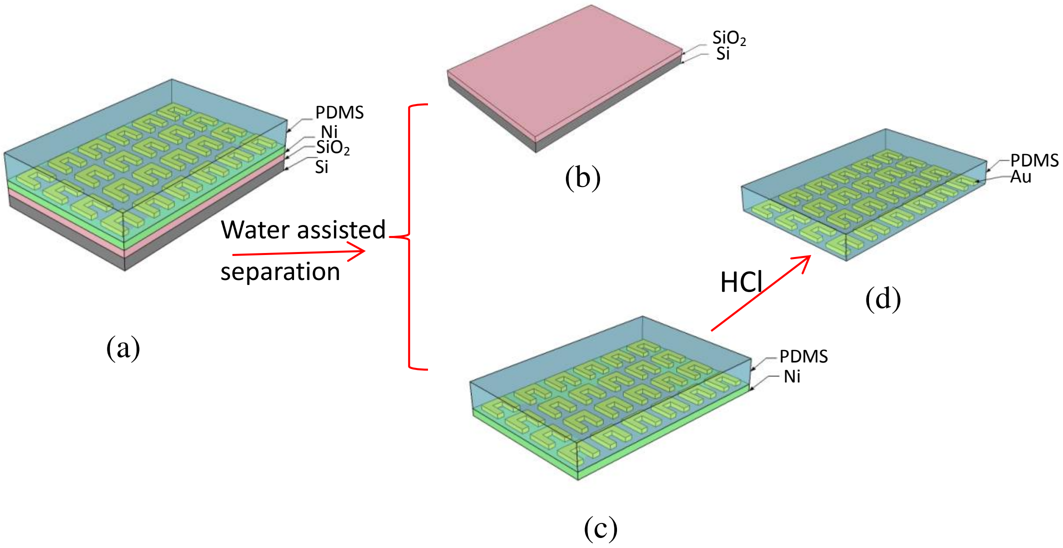

Figure 3- 6 Water assisted separation process. (a) the rigid substrate with PDMS coated and it separates into (b) and (c) automatically in the presence of water. (d) the PDMS-metamaterial after removing Ni layer.

The reason why the deflection effect is absent in this method can be illustrated in figure 3-6. The Ni layer will separate from the SiO_2 layer automatically in presence of water so that the deflection effect is absent here because PDMS has no chance to contact SiO_2/Si substrate. As a result, the Ni layer can react with HCl thoroughly. It was assumed that a nickel silicate or nickel oxide layer was formed during the evaporation process to explain why the Ni will separate from SiO_2 in the water environment.[147] Nickel hydroxide ($Ni(OH)_2$) was generated when nickel silicate or nickel oxide encounters water. Both $Ni(OH)_2$ and SiO_2 are hydrophilic so that water can penetrate along the interface efficiently and destroy the contact between Ni and SiO_2, separating Ni layer from SiO_2 surface automatically.

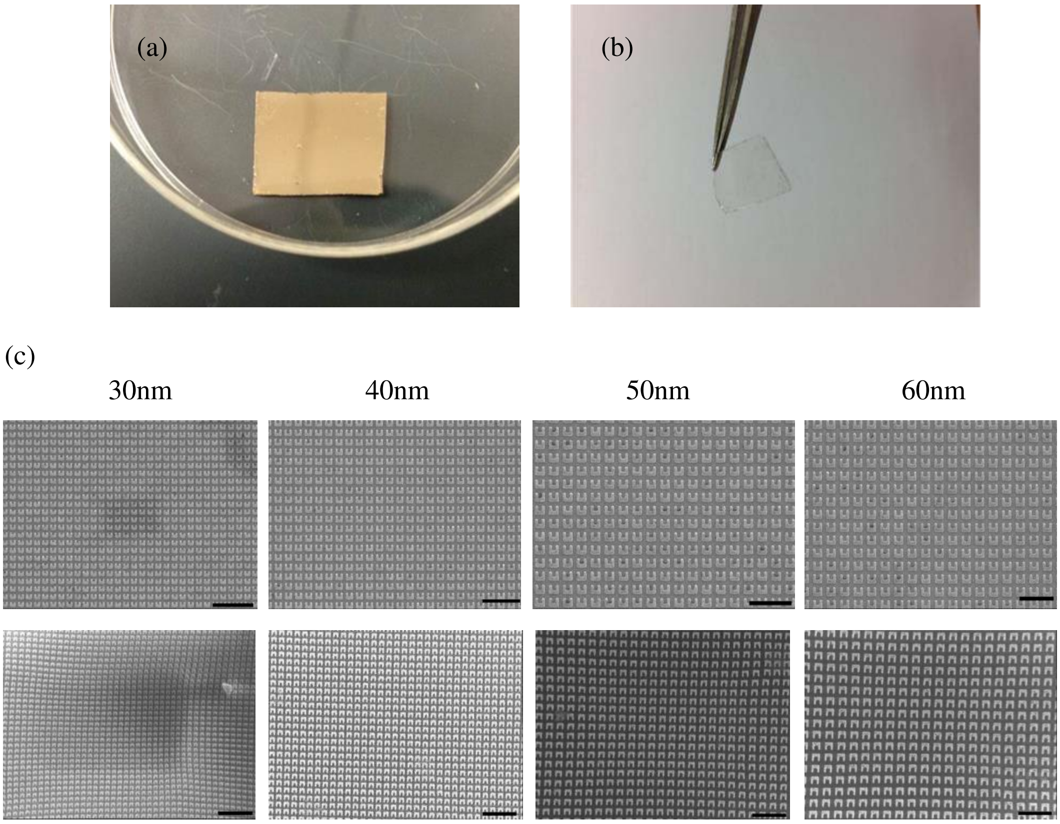

Figure 3- 7 Comparison before and after transfer. (a) optical image of the chip coated with PDMS layer which is corresponding to figure 3-5b (b) the flexible and transparent PDMS after releasing from the rigid substrate (c) SEM image of the pattern before and after transfer, the upper row is the pattern on the $Ni/SiO_2/Si$ substrate and the under row is the same pattern on PDMS after transfer, each column means the different size of the arm bar of the SRR. The scale bar in this picture is 1 μm.

Figure 3-7 shows the comparison of the substrate and pattern before and after transfer process. Figure 3-7b shows that the PDMS can be released from the $Ni/SiO_2/Si$ completely and PDMS is quite thin and flexible. We examined the structure on the $Ni/SiO_2/Si$ substrate and on the PDMS and shown in figure 3-7c in upper row and under row, respectively. We can see that the SRR arrays can be transferred from rigid substrate to PDMS completely without any damage and break. The structure shape and size can be maintained after the transfer process. The image distortion in the PDMS (under row) is attributed to the charge effect of non-conductive PDMS during SEM process. Therefore, the distortion is not from the shape changing of the structure.

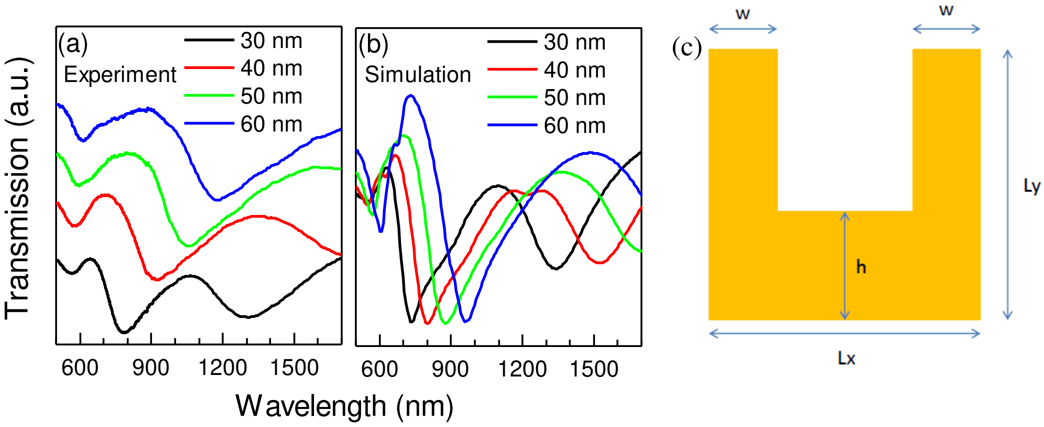

Figure 3- 8 Transmission of SRR. (a) experimental transmission of SRR embedded in PDMS. (b) simulated transmission of SRR embedded in PDMS. (c) the dimension of the SRR, Lx=Ly=4w, h=1.6w.

Apart from the structure, we also checked the optical properties of the structure after transfer. The transmission of the SRR arrays embedded in PDMS was measured with Craic 20 microspectrophotometer because PDMS is transparent. As shown in figure 3-8a, both the electric and magnetic mode can be observed and they red shifted with increasing size. The resonance of the SRR arrays embedded in PDMS was also red shifted compared with the SRR arrays on the glass because of the larger refractive index of PDMS. In the meantime, the PDMS residing in the SRR gap will introduce large capacitance and rendered the magnetic resonance red shift. We also conducted the simulation of the transmission spectrum with FDTD as shown in figure 3-8b. The shift trend agreed what we observed in experiment and the slight deviation of the resonance frequency of each size was attributed to the slight deviation of the real structure dimension and the size we used in the simulation. Overall, the optical properties can be maintained after transferred to PDMS, which indicates the success of our transfer method.

3.3 Application of Metaflex

3.3.1 Application in chemical Sensing

Metamaterials have been proven to be a good medium in the sensing application because the resonance frequency are sensitive to the local environment as we discussed in chapter 1.[47] For instance, terahertz metamaterials were utilized for thin film sensing[148] and the dielectric layer sensing.[149] In addition, metamaterial fabricated on plastic is very promising in biological and chemical sensing, with the advantages of deformability and transparency.[51]

Regarding sensing application, PDMS substrate provides several advantages over a rigid substrate. First of all, PDMS is transparent and it will not impose any negative effect when taking the optical measurement. Secondly, PDMS is bio-friendly and it even can serve as the platform for a living cell, highlighting the great potential in bio-sensing. SRR resonator is presented with two resonant modes, *i.e.* electric mode and magnetic mode. For the electric mode based sensing, it shares with the same principle with other typical nanostructures whose resonance will shift once the local refractive index changed. However, the magnetic mode emerges from the circulating current along the SRR, the mode can be simplified with a *LC* oscillator and the resonance frequency can by represented by $w_{LC}=(LC)^{-1/2}$, here L is the conductance along SRR and C is the capacitance in the gap. The substance absorbed in between the gap will introduce the change of capacitance and thus make the resonance wavelength shifted. Therefore, both the electric and magnetic mode of the same SRR can be utilized to detect molecules and the sensitivity can be compared to investigate the sensing mechanism for different modes.

As a demonstration, we choose 2-naphthalenethiol molecule as the probed substance because a monolayer on the order of 1 nm thickness can be formed on the

Au surface due to the strong bonding between thiol-group and Au. 2-naphthalenethiol powder (Sigma-Aldrich) was dissolved in ethanol with the concentration of 5 mM/L and then the PDMS-metamaterials were soaked in the solution for 12 hours to make sure that a homogenous monolayer can be formed on the metamaterials surface. Subsequently, the PDMS chip was rinsed with ethanol for 1 min to remove the 2-naphthalenethiol molecules which were not bound to the metamaterials surface. The chip was then blow dried with nitrogen gas. A cartoon is shown in figure 3-9 to illustrate the formation of a monolayer 2-naphthalenethiol on SRR surface.

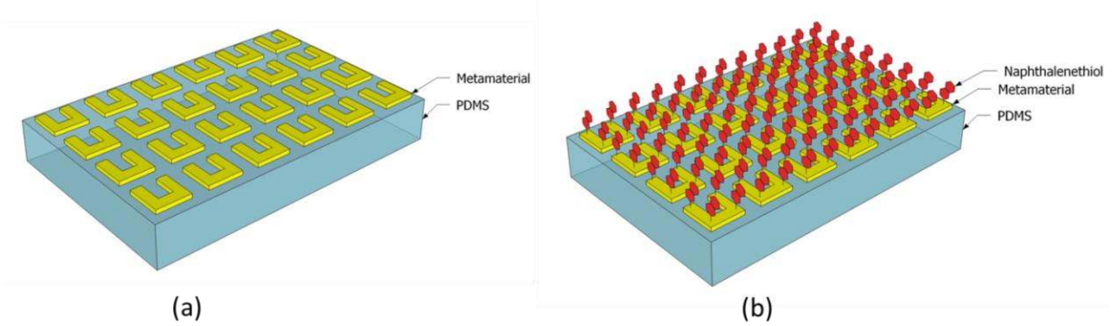

Figure 3- 9 Formation of a 2-naphthalenethiol monolayer on the SRR surface. (a) the metamaterials embedded in PMDS (b) a monolayer of 2-naphthalenethiol is attached to SRR surface due to the thiol-Au bonding.

We evaluated the sensitivity by monitoring the transmission spectrum with and without the 2-naphthalenethiol attachment. The transmission was measured on Craic 20 and we measured four patterns with different feature size as shown in figure 3-10. We observed that both the electric and magnetic resonance frequency were red shifted when a monolayer 2-naphthalenethiol molecules were attached no matter what feature size we use. The resonance wavelength shift was around 30 nm even for a monolayer attachment, illustrating that the sensitivity was very promising for the application in biological and chemical sensing.

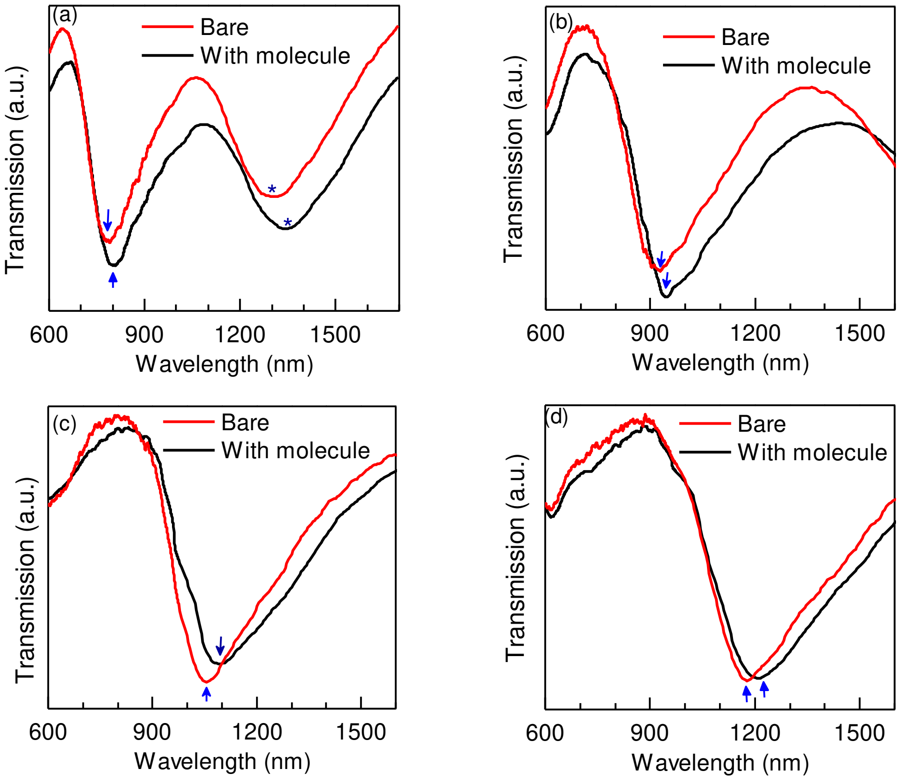

Figure 3-10 Transmission of PDMS-metamaterials with and without 2-naphthalenethiol attachment. (a), (b), (c) and (d) are corresponding the width size w= 30, 40, 50, 60 nm. Note: the arrows indicate the electric resonance and the stars mean the magnetic resonance.

3.3.2 Application in SERS

Starting from the first electrochemically roughed silver electrodes SERS substrate, many SERS substrates and configurations have been invented during the past 30 years. The primary goal of SERS study is to optimize the enhance factor (EF) as much as we can to enhance the detection sensitivity even down to a single molecule diagnosis. However, the SERS substrate should also concern the contact issue between the analyte and the SERS substrate. The substrate effects and the surface chemistry of the absorbate will also affect the SERS detection. For instance, some analyte are difficult to be attached to the SERS substrate due to the surface chemistry. In addition, the contact between the analyte and the SERS substrate will contaminate the substrate and make it irreproducible for the next detection. It is desired to invent a SERS substrate which can prevent the probed substance from contacting the metal structure directly but still can maintain the enhancement factor in a high value.

Numerous SERS substrates such as the roughed surface, assembled nanoparticles are presented in the contact mode in which the analytes is absorbed on the metal surface. The advantage of the direct contact is that it can provide the highest electric field enhancement. The direct contact will be preferred if we just care about the enhancement factor. As we know, the localized field decays dramatically outside the nanosphere so that the enhancement will be higher when the absorbate is closer to the metal sphere surface. However, it is not necessary to make the analyte directly contacted to the metal surface because the electric field is high enough to provide Raman enhancement in a volume and the enhancement still can be prominent in the presence of a gap between the analyte and the metal surface. The SERS enhancement is proportional to E^4 (if $w \approx w'$) and the field E outside the nanosphere decays with r^{-3}, by considering the total amount of the analyte absorbed on the surface in proportional to the surface area in the factor r^2, so the Raman intensity decay can be expressed as $I = (1 + a/r)^{-10}$, where I is the Raman intensity, a indicates the distance between the analyte and the metal surface, r is the radius of the whole structure including the volume of the analytes, suggesting that SERS is a long range effect.[150] It was shown that a transition metal layer was deposited on the plasmonic structure to modify the surface reactivity.[151, 152] The transition metal can serve as a catalyst and the SERS can trace the catalytic reaction. The transition metal layer should be thin enough to guarantee that the analytes are still within the field enhancement volume. Though the additional transition metal can separate the analytes from the underneath plasmonic structure, the molecules still contact the transition metal directly.

Many other non-contact SERS substrates are demonstrated to accomplish some specific applications. Tip enhanced Raman scattering (TERS) is a kind of non-contact mode in which the analyte resides on any substrate and then move the tip close to the analyte serve as a Raman amplifier to obtain SERS effect. The drawback of TERS is that volume of strong electromagnetic field around the tip is very small and the total Raman signal is very week, making it only feasible to the molecule with large Raman cross section. Besides TERS, shell-isolated nanoparticle-enhanced Raman spectroscopy (SHINERS) also can separate the probed substance from the metal particle while at the meantime provide considerable enhancement factor.[92] SHINERS was realized by adding a spacer shell (silica or alumina) outside the metal particle to prevent the contact between analyte and the metal particle. In SHINERS, each shell coated particle serve as a tip in TERS and make the total Raman signal much larger than TERS. However, the particle in SHINERS is in solution phase, rendering it not convenient to apply it onto any surface as desired. The nanoparticles embedded in PDMS were also reported to serve as a SERS substrate which can separate the analyte from the nanoparticle.[153] The drawback in this method they used is that it is very difficult to control the size and the particle density so that they cannot tune the resonance frequency at will.

Herein, we demonstrated our metamaterials embedded in PDMS polymer as a convenient, simple and effective SERS substrate which can separate the probed substance from the metamaterials just by simply covering the PDMS metamaterials on to the surface we want to detect. Our PDMS metamaterials SERS substrate is regular, highly-controlled, well-defined and reproducible because the size, pattern density, resonance frequency can be changed at will based on EBL writing. In addition, the PDMS metamaterials SERS substrate is reusable, the SERS substrate can be released from the surface and then applied to another surface for detection relying on the fact the metamaterial itself never contact the probed substance at all.

For demonstration of the application of the free standing metamaterials on SERS, we still use the 2-naphthalenethiol molecule for the convenience that the thiol-Au bonding can facilitate the monolayer formation on the Au surface and we can count the amount of the molecules for the quantitative analysis. We designed several SERS configuration as shown in figure 3-11. All the Raman spectra was taken at the Horiba-JY T64000 micro Raman spectrometer, we used a solid state laser with the excitation wavelength of 785 nm and the excitation power was fixed at 2.6 mW and a 50× objective was utilized. The reason why we used the 785 nm as the excitation source was that the electric resonance wavelength of 30 nm width SRR was around 784 nm as shown in figure 3-8a.

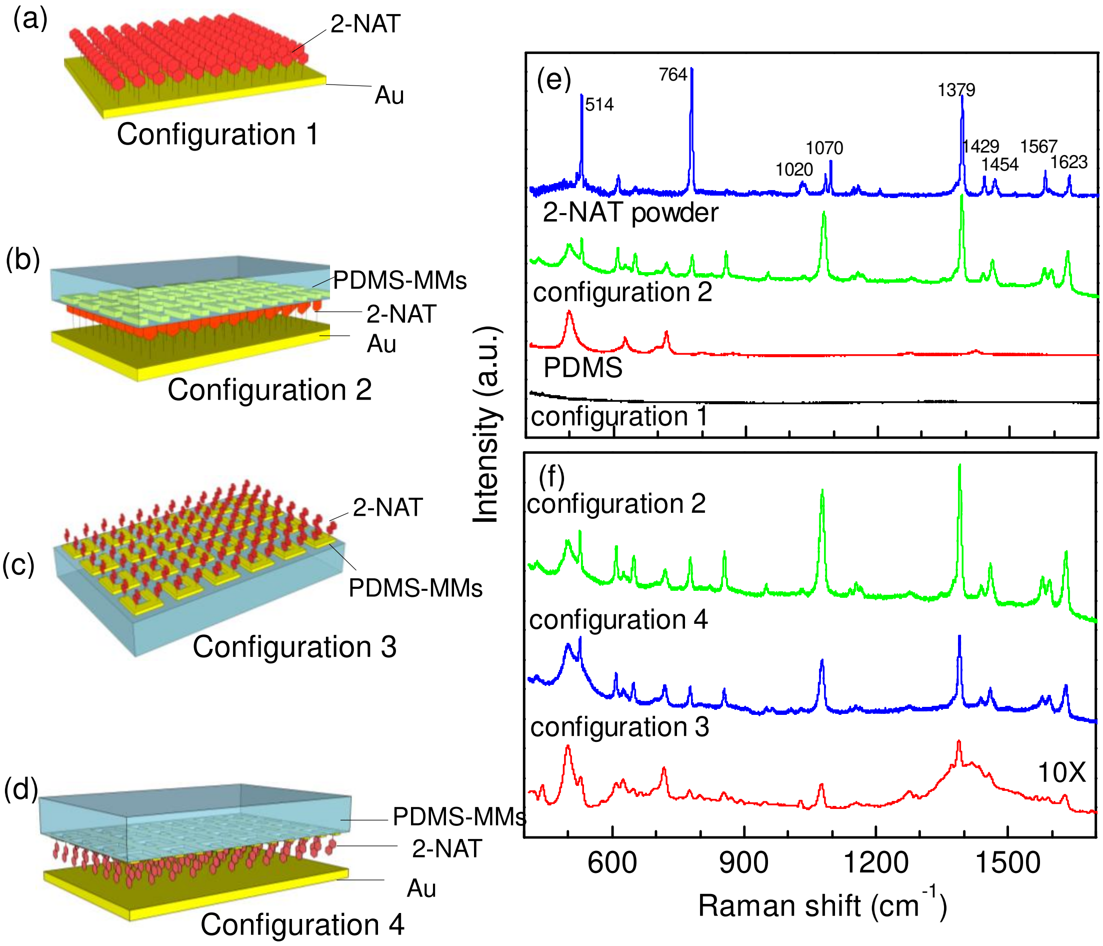

Figure 3- 11 Free standing metamaterials SERS configurations. (a) a monolayer 2-naphthalenethiol molecules on Au (60 nm), 2-NAT is the abbreviation of 2-naphthalenethiol (b) a PDMS-metamaterials covers on the top of Au film with 2-NAT attached (c) a monolayer of 2-NAT is attached to SRR top surface (d) the PDMS-metamaterials with 2-NAT attached on the SRR surface covers on a clean Au film (e) Raman spectra of the powder, PDMS, configuration 1 and 2. (f) Raman spectra of the configuration 2,3,4. Noted: all the Raman spectra was taken at the same excitation power; the vertical scale in figure e and f is different.

As we discussed in the chapter 1, making the excitation laser wavelength closer to resonance wavelength can give the optimum field enhancement as well as the highest Raman signal enhancement. In our experiment, all the samples used are the 30 nm width SRR with the electric resonance wavelength at 784 nm to match the laser wavelength. First of all, we taken the Raman spectrum of the 2-naphthalenethiol powder to obtain the characteristic Raman peaks which is shown in the blue line in figure 3-11e. A strong peak at 1379 cm^{-1} is due to the ring stretching mode, the peak at 1022 cm^{-1} is from the C-H bonding and both the peak of 764 cm^{-1} and 514 cm^{-1} emerge from the ring deformation modes.[154] We also measured the Raman spectra of pure PDMS as shown in the red line in figure 3-11e to exclude the background signal. The peaks of 489 and 710 cm-1 comes from the Si-O-Si stretching and symmetric Si-C stretching vibration modes respectively.[155] These two PDMS peaks will be always presented in the measurement when the PMDS is involved and we can ignore them. 60 nm Au film was deposited on Si wafer by thermal evaporator to serve as the Au film in figure 3-11 and the 2-naphthalenethiol monolayer was prepared as same as the description in the last section. For the configuration 1 in which a monolayer was formed on an Au film and we shine the laser on it to measure the Raman signal, we cannot observe any Raman peaks as shown in the black line in figure 2-11e. The total Raman cross section of the monolayer is very small because of the small amount of the molecules and Raman signal cannot be observed without the surface enhancement, however, the Au film is too flat to sustain a localized surface plasmon and no SERS effects can be achieved. Then we cover the PDMS-metamaterials onto the Au film with a monolayer of 2-naphthalenethiol attached to form a sandwich structure, the PDMS can be absorbed on the Au surface tightly due to the van der Waals interaction so that the metamaterials embedded in the PDMS can stay close to the molecules on the Au film. After covering the PDMS metamaterials on the Au film top, we focus the laser beam on the pattern area of the PDMS to finish the measurement. We can ignore the effect of the PDMS during the Raman measurement because PDMS is totally transparent and very thin. The Raman spectra of configuration 2 is shown in the green line in figure 3-11e. We can observed all the characteristic Raman vibration modes corresponding to the 2-naphthalenethiol powder to confirm that the Raman signal was indeed from the 2-naphathalenethiol monolayer on the Au film. The dramatic Raman enhancement in configuration 2 comparing to configuration 1 suggests that the PDMS metamaterials play a critical role in the Raman enhancement. Based on the geometry of the configuration 2, we hypothesize that there may exit two ways to enhance the Raman signal, the first is that the metamaterials themselves can generate hot spots which are capable of enhancing the Raman signal when the molecules are in proximity to the SRR surface, another mechanism is that the coupling between the metamaterials and the underneath Au film can confine the electromagnetic field in between the gap where the 2-naphthalenethiol molecules are located, which may be also responsible for the huge Raman enhancement. In order to confirm these two assumptions, we designed two more configurations to conduct the SERS measurement. As shown in figure 3-11c, a monolayer of 2-naphthalenethiol is formed on the SRR surface (also shown in figure 3-9b) and the Raman measurement was conducted to evaluate our first hypothesis above. The Raman spectra of configuration 3 is shown in red line in figure 3-11f, we can observed the characteristic modes of 2-naphthalenethiol and conclude that the metamaterials themselves embedded in the PDMS can give the SERS effect though the enhancement factor is not that high. As we discussed in the SERS section in chapter 1, the Raman enhancement of an isolated plasmonic element is much weaker than elements in coupling state which can increase the electromagnetic field intensity for several order. In our SRR arrays, the coupling between two adjacent SRR can be ignored because of the large interval distance so that the Raman enhancement in configuration 3 arises from the superposition of the single SRR element. In order to evaluate the second hypothesis above, we construct the configuration 4 by covering the chip in configuration 3 on to the bare Au surface. We can see that configuration 2 and 4 are quite similar while the only difference is the location of the molecules. The 2-naphthalenethiol molecules are residing on the whole Au surface in configuration 1 while the molecules reside only on the SRR top surface and no molecules will be present outside the SRR top surface in configuration 4 because the 2-naphthalenethiol molecules cannot be attached to the PDMS surface.

The Raman spectra corresponding to configuration 4 is shown in the blue line in figure 3-11f. The much higher Raman signal of configuration 4 comparing with configuration 3 clearly indicate that the coupling between the SRR and the underneath Au film can further enhance the Raman signal dramatically. We will discuss the coupling effect in more details in the next section by conducting the electromagnetic simulation. The enhancement factor of each configuration can be estimated by the equation $EF = \frac{I_{SERS}}{N_{SERS}} \bullet \frac{N_{powder}}{I_{powder}}$, where I_{SERS} and I_{powder} are the Raman intensity of the SERS and powder respectively, while N_{SERS} and N_{powder} are amount of molecules within the laser beam when measuring the Raman of SERS configuration and powder. The amount of the molecules N_{SERS} involved to contribute to I_{SERS} can be estimated by considering the diameter of the 2-naphalenethiol molecule and the diameter of the laser beam and the amount of the molecules N_{powder} involved to contribute to I_{powder} can be obtained by dividing the total volume of the power with the volume of a single 2-naphthalenethiol molecule. Here, the area of the molecule is 0.42 nm^2, the height of the powder sample is 2.34 mm, the density of the powder is 1.550g/cm^3 and the molecule mass is 160.24g/mol. I_{SERS} and I_{powder} is obtained by considering the Raman intensity, herein we take the ring-ring stretching Raman mode at 1379 cm^{-1} to estimate the enhancement factor. The intensity corresponding to powder, configuration 2, 3, 4 are 13023, 11100, 236 and 5840 a.u. respectively. The estimated enhancement factors of configurations 1 to 4 are 0, 4.9×10^{-6}, 3.4×10^{-5} and 8.6×10^{-6} respectively. By comparing configuration 2 and 4, we can see that the Raman intensity of configuration 2 is larger than configuration 4 in figure 3-11f while the configuration 2 has lower enhancement factor, which is attributed the smaller amount of the molecules involved in configuration 4. By considering the different location of the molecules in configuration 2 and 4, we can conclude that the molecules located in between the gap between SRR and Au film contribute more to the SERS signal than the molecules located outside the gap.

From the configuration in figure 3-11 we can see the metamaterials themselves can provide considerable Raman enhancement even though in the absence of the coupling to the substrate, so that it is possible to apply this PDMS metamaterials onto an arbitrary substrate to obtain the SERS signal besides an Au film. For the demonstration, we covered the free standing metamaterials onto a Si wafer to detect the molecules residing on Si substrate. Here we taken benzyl butyl phthalate (BBP) ($C_{19}H_{20}O_4$) as an example, BBP is a kind of plasticizer usually contained in the children toys even sometimes in the food and it is harmful to human health.

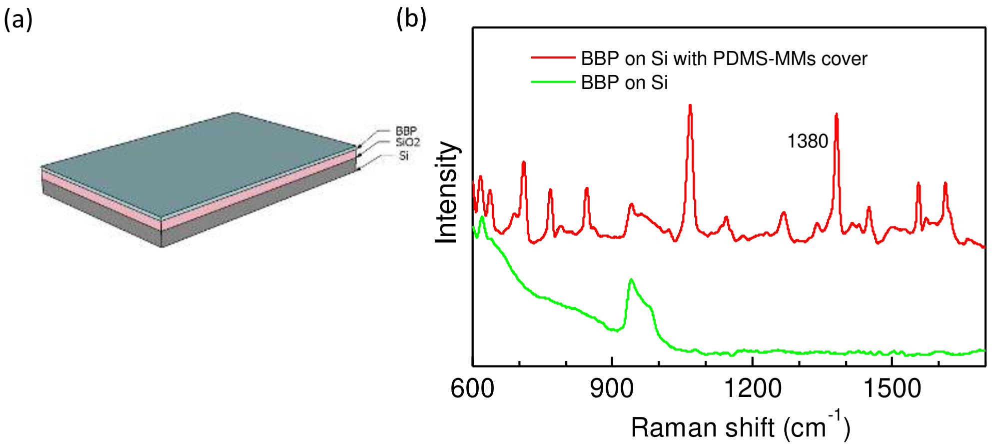

Figure 3- 12 Detection of BBP on the Si substrate. (a) the formation of a BBP layer on Si substrate (b) the Raman signal of the BBP molecules with and without PDMS metamaterials covering on the top.

As shown in figure 3-12a, we dropped the BBP with the concentration of 0.1 mM/L onto the Si substrate with a thin silicon dioxide layer and a layer of BBP will be formed after the solvent evaporated. The Raman measurement was conducted directly on the chip (figure3-12a) and no signal can be observed as shown in the green line in figure 3-12b. Subsequently, we covered the PDMS metamaterials on the silicon chip with the procedure as same as the configuration 2 in figure 3-11 and then we focused the laser spot on the pattern area to measure the Raman signal. The Raman spectra with PDMS metamaterials covering on the top is shown in the red line in figure 3-12b, we can clearly see the spectra of the BBP, the characteristic mode of

1380 cm^{-1} is due to the ring-ring stretching vibrational mode. We assume that the Raman enhancement purely emerges from the hot spots of the metamaterials themselves. In contrary to the Au film we studied above, the SiO_2/Si substrate has no effects on the enhancement factor because the substrate silicon dioxide is a kind of dielectric and there is no coupling between metamaterials and the substrate. The fact the SERS even can be achieved without the coupling to a metallic substrate suggest that we can apply our PDMS onto an arbitrary substrate to detect the molecule residing on the substrate. For instance, we can paste our PDMS metamaterials onto an apple or orange surface and then measure the Raman signal to complete the diagnosis of the harmful substance on them, which will make our free standing metamaterials SERS substrate can be broadly used in food safety.

3.3.3 Application in studying the coupling properties

As we discussed in the last section, the coupling between the metamaterials and the Au film underneath is responsible for dramatic Raman enhancement. In fact, the nanoparticle coupled to a metallic system has attracted a lot of attention due to the ultrahigh field confinement in between the gap and the rich optical properties of the interaction. As interpreted by Leveque *et al*, the incidence laser can excite the localized plasmon mode of the nanoparticles and the delocalized surface plasmon polariton of the metallic film as well. The coupling between the localized and delocalized surface plasmon mode can concentrate the electromagnetic field in between the gap.[156] Several geometries have been designed to investigate the coupling properties such as the gap distance dependence, the limit enhancement probe.[107, 157]

Usually the nanoparticles were synthesized in colloidal and then dispensed onto a metallic film and the distance between the nanoparticles and the metallic film can be controlled by the length of the molecules absorbed on the metallic film. Herein, our free standing metamaterials provide an excellent platform to investigate the coupling scenario by simply covering the PDMS metamaterials on to Au film, making this method convenient, reproducible and easy to handle.

The simulation results are shown in figure 3-13, we conduct the simulation of two configurations as shown in figure 3-13a and 3-13b with and without the Au film respectively. In the simulation, we assume that the metamaterials are not embedded PDMS completely, instead the SRR top surface is raised 5 nm above the PDMS surface as indicated in figure 3-13a. Figure 3-13(a-1) and (a-2) show that hot spots can be generated near the SRR surface especially around the corner, which is responsible for the Raman enhancement in figure 3-11c.

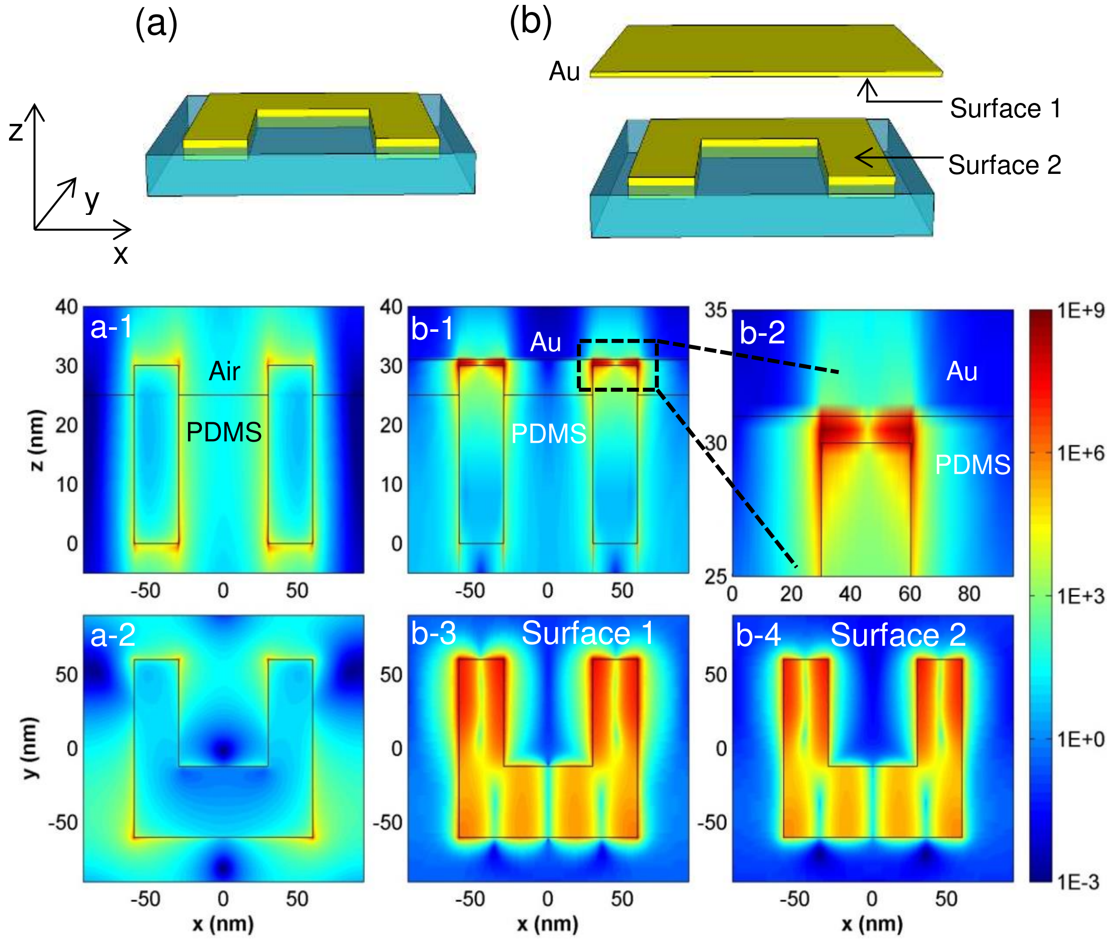

Figure 3- 13 FDTD electric field simulation. (a) Schematic of the SRR metamaterials embedded in PDMS and the SRR is out of the PDM surface for 5 nm. (b) Schematic of the Au film couple to the PDMS metamaterials. (a-1) E field distribution of the SRR in configuration (a) in a cross section view. (a-2) E field distribution of the SRR in configuration (a) in a top view. (b-1) cross section view of E field distribution of the coupled system in configuration (b). (b-2) the zoom in view inside the gap. (b-3)

top view of the E field distribution on Au film (surface 1). (b-4) top view of the E field distribution on SRR surface (surface 2). Note: the value in the color bar is corresponding $|E|^4$; the gap between Au film and SRR we set in simulation is 1 nm.

In order to understand the coupling mechanism, we conduct the electromagnetic field simulation by FDTD method and then compare the field enhancement in the simulation with the Raman enhancement factor we obtain in the SERS measurement. It is important to point out that the hot spots are still presented inside the PDMS substrate, which is due to that the PDMS has low permittivity and lossless, so that PDMS imposes negligible effect on the distribution of the E field. While for the silicon substrate, all the energy will dissipate in the substrate and the hot spot is impossible to be sustained inside the substrate. Figure 3-13(b-1) and (b-2) show that the electromagnetic field is confined in the gap very intensely. Figure 3-13(b-3) and (b-4) show the top view of field intensity of the gap. We then calculate the average field enhancement based on the 2-naphalenethiol molecule location in different configurations in figure 3-11. For configuration 3 and 4 in figure 3-11, the molecules are located on the SRR surface, so that we need to integrate the field on SRR surface on a-2 and b-4 in figure 3-13, respectively. While for configuration 2, the molecules are located on Au film, in this case to integrate the whole area in figure 3-13(b-3). The experimental and simulated enhancement factors are summarized in table 1. In the simulation, we assume that the enhancement factor is proportional to $|E_{SERS}|^4 / |E_{incidence}|^4$ in the case that the incidence frequency, resonance frequency and Raman scattering frequency are perfect matched. However, it is impossible to make those three frequencies perfectly matched and the enhancement will not follow $|E_{SERS}|^4 / |E_{incidence}|^4$ strictly, so that we will obtain the deviation between experimental and simulation data. The trend of the enhancement factor in the simulation agrees well with the experimental measurement.

Table 1 Calculated and experimental enhancement factor for different configurations.

system	Calculation enhancement	Experimental enhancement factor

	factor $\left\|E_{SERS}\right\|^4 / \left\|E_{incidence}\right\|^4$	$EF = \frac{I_{SERS}}{N_{SERS}} \cdot \frac{N_{powder}}{I_{powder}}$
Configuration 2	2.9×10^5	4.9×10^6 [a]
Configuration 3	1.0×10^3	3.4×10^5 [b]
Configuration 4	1.8×10^6	8.6×10^6 [b]

[a] the integration region is the Au film surface

[b] the integration region is the SRR top surface

Besides metamaterials, we can also embed other structures of interest into PDMS and cover to other substrates at will to investigate the interaction between the plasmonic elements and the metallic substrate. The free standing metamaterials provide a versatile method for the investigation of the interaction between the plasmonic or metamaterials and the substrate.

3.4 Summary

In this chapter, firstly we introduce some background of the flexible and transparent electronic and photonic devices. Inspired by the exciting application of the stretchable devices in the display, sensor and energy harvesting devices, we also want to apply the flexible and transparent substrate on to the metamaterials. Applying the transparency and flexibility to the metamaterials can bring some benefits. For instance, the metamaterial on the flexible substrate enables the construction of 3D metamaterials by stacking it layer by layer, which makes the process much simpler than the conventional multiple EBL steps. The flexible metamaterials also can make the device active, which means the optical properties can be tuned by applying a strain on it. In addition, the flexible metamaterials can lower the loss of the substrate and enhance the sensing sensitivity as well. Herein, we desire to embed the metamaterials onto a very thin and flexible PDMS substrate because PDMS has excellent mechanic properties and biocompatibility.

For the fabrication of metamaterials on PDMS, we choose the transfer method to transfer the metamaterials from a rigid substrate to the PDMS by utilizing a sacrificial layer. Firstly, we proposed to make use of the SiO_2 as the sacrificial layer by fabricating the metamaterials on the commercial SiO_2/Si wafer by EBL, and then remove the SiO_2 layer with HF to make the metamaterials embedded in PDMS. However, the SiO_2 sacrificial layer cannot work for PDMS because of the deflection effect, in which the PDMS will collapse to contact the Si substrate to prevent the HF solution penetrating into the central area further. The SiO_2 cannot be etched even for a very small chip. In order to avoid this deflection effect, we use the Ni as the sacrificial layer instead. The deflection effect is completely absent if we use Ni as the sacrificial layer because the Ni layer will separate from the SiO_2 layer in the presence of water and then the HCl solution can etch the Ni layer completely to make the metamaterials embedded in PDMS. The SEM image indicates that the pattern can be transferred without any damage and break, and the transfer yield is almost 100%. What's more, the optical properties can be maintained after the transfer process.

The first application of the PDMS metamaterials is sensing. For the demonstration, we monitor the resonance shift by attaching a monolayer of the 2-naphthalenethiol, the result shows that the shift is prominent even for the monolayer with the thickness around 1 nm, suggesting the sensitivity is high. The PDMS metamaterials also have huge potential in the biosensing because PDMS is highly biocompatible. The Second application of the free standing metamaterials is in the SERS. The metamaterials embedded in PDMS can serve as a convenient SERS substrate to avoid the direct contact between the probed substance and the substrate. The SERS can be accomplished by covering the PDMS metamaterials onto the substrate with the molecules we want to detect residing on it. For the demonstration, we utilized 2-naphthalenethiol molecules residing on an Au film to achieve the SERS and many configurations were designed for comparison. We even can achieve SERS effect by covering the PDMS metamaterials on to a Si substrate to detect BBP, indicating the huge potential to detect the molecules on arbitrary surface such as the fruits and eggs. The PDMS metamaterials also can be utilized to investigate the interaction between the metamaterials and the Au film underneath by covering the PDMS onto the Au substrate. In fact, we can extend this method to any other structure and substrate. We can embed the interesting structure into PDMS with our transfer method and the cover it onto the substrate we want to learn the interaction, making it as a representative mode to study the coupling between the plasmonic or metamaterials structure and the substrate.

Chapter 4 Integration of Metamaterials to Vanadium Dioxide-Active Metamaterials

4.1 Introduction

4.1.1 Tunable and active metadevices

When we talk about metamaterials, the first thing coming to our mind is the ability to engineer the optical properties by changing the meta atoms and their spatial arrangement. Considerable progress has been made in the metamaterials research, for instance, the transform optics emerges from the metamaterials to control the light path and achieve the invisible cloak functionality, the negative index medium was invented to reflect the light in opposite direction compared with the conventional matter, chiral metamaterials were applied to engineer the polarization of the light with much higher efficiency than the naturally occurred crystal. However, the optical properties are fixed at the moment when the fabrication process is completed. We have to produce another chip with different parameters and configurations if we want to tune their properties as desired. The ability to tune the properties of the metamaterials after fabrication is essential to make the metamaterials as practical devices, forming the field of *active metamaterials* that considerable effort has been devoted to.

The most direct method to tune the optical characteristic of the metamaterials is to reconfigure the metamaterials on the same chip. The properties of the metamaterials are determined by the shape, size, material of the individual meta atoms and the interaction between the meta atoms. One strategy is to reconfigure the relative positon of the meta atoms to manipulate the coupling between the meta atom and consequently engineer the optical characteristics of the metamaterials. Microelectromechanical system (MEMS) is promising in the construction of the reconfigurable metamaterials. It was demonstrated that the optical properties of metamaterials can be tuned by fabricating the meta atoms on the MEMS driven platform. The positon of one array was fixed and then another array was fabricated on a movable platform so that it was possible to adjust the relative positon between those two arrays.[158] In addition, two arrays can be fabricated on a bimaterial cantilever whose responses to thermal stimulus are quite different, so that the relative positon of those two arrays can be adjusted by controlling the external thermal stimulus.[159] Another method to tune the properties is to utilize a polymer as will be discussed in the last chapter, the coupling strength of the adjacent meta atoms can be changed by applying a strain on the polymer to alter the gap between the meta atoms.[141] For all those reconfigurable metamaterials, it is challenging to manipulate the positon of nanoscale meta atoms accurately and the fabrication of configurable metamaterials will cost a lot of time.

Another notable strategy to obtain the tunability is to integrate the metamaterials on a semiconductor substrate. As we know, the conductivity and dielectric properties of a semiconductor can be controlled by changing the carrier density by carrier injection or depletion. The optical properties of the metamaterials rely on the surroundings environment, so that we can fabricate the metamaterials on a semiconductor substrate and tune their optical response by manipulating the dielectric properties of the substrate. The carrier injection or depletion can be achieved by different kinds of external stimuli such as electric field or light radiation, which offers us a lot of convenience to engineer the optical response of metamaterials. For instance, the transmission of the split ring resonators fabricated on a GaAs substrate can be modulated by applying an electric stimulus.[160] The applied electric signal will inject carriers in the gap region and make the gap more conductive and the substrate has the trend to short the gap to make the magnetic mode vanish. While the magnetic mode will resume once the external electric signal was remove because the carrier will redistribute without the electric stimulus. It has also been demonstrated that the carrier density of the semiconductor substrate can be manipulated by photoexcitation because the carrier density of the substrate is dependent on the power of the excitation.[161] Consequently, the response of the metamaterials can be engineered by changing the excitation wavelength and power. The main advantage of the semiconductor substrate based active metamaterials is that it is capable of controlling the response in real time and the change of the properties is reversible. In addition, the integration of metamaterials onto a semiconductor substrate offers huge potential in the application of electro-optical modulation and optical switch.

The combination of metamaterials and the phase change material (PCM) provide another promising way in making active metadevices. PCM is initiated by the structural phase change and each phase has its own characteristic properties, *i.e.*, refractive index. PCM is widely used in the disk and data storage where the optical properties (reflectivity or transmittance) and electric properties (conductivity) change dramatically after the phase transition. The phase transition can be induced by various stimuli such as light, temperature, pressure, electric and magnetic field. Whether the phase change is reversible or irreversible is dependent on what PCM we use. In analogy to the semiconductor substrate we discussed above, the huge change of the properties of PCM can also be utilized to manipulate the optical response of metamaterials. $Ge_2Sb_2Te_5$ (GST) and vanadium dioxide (VO_2) have received much interest to construct active metadevices. GST has three phases and the phase transition can be induced thermally. GST was utilized to integrate to split ring resonator to modulate the transmission.[162] In chapter 6, we will discuss how to use GST to construct a thin film perfect absorber. VO_2 has metallic and insulation phases with a phase transition temperature around 340 K. What's more, the phase of VO_2 depends on the temperature in real time, making it advantageous to construct real time controlled active metadevices. It was reported that the terahertz metamaterials was fabricated on VO_2 thin film for the memory application.[163] In this chapter, we will focus on the visible-near IR active metamaterials by using VO_2.

4.1.2 Vanadium dioxide (VO_2)

VO_2 is a typical phase change material which undergoes a first order metal-insulator transition (MIT) near 68℃. The low transition temperature makes it very attractive in the practical devices applications. Considerable efforts in both theory and experiments have been devoted in order to understand the transition mechanism. Up to now, two main transition mechanisms, which are Peierls transition and Mott transition, were recognized by the community. Peierls transition argues that MIT emerges from the instability of the lattice dynamics while Mott transition suggest that the strong electrons correlation renders the charge localization such that insulating property is resulted.[164-167] The theory of the metal-insulator transition is very rich and it is out of our focus in this thesis. VO_2 is presented as a rutile structure at high temperature (metallic phase) and a monoclinic structure in low temperature (insulating phase) as shown in figure 4-1a and 1b respectively.

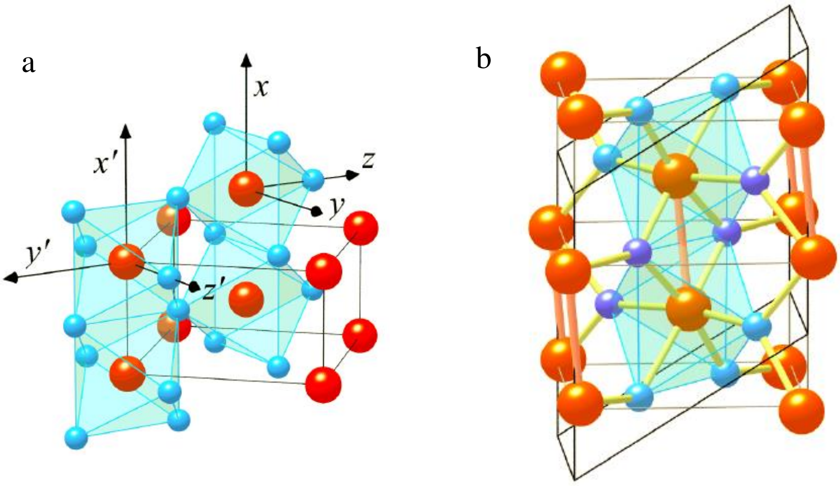

Figure 4-1 Schematic of VO_2 structure. (a) rutile structure in high temperature (metallic). (b) monoclinic structure in low temperature (insulating). Note: large and small sphere refer to the vanadium and oxygen elements respectively. Picture taken from V. Eyert[164]

VO_2 thin film is capable of transiting from the metallic phase to semiconducting at the critical temperature near 68℃. It was revealed that nanoscale metallic puddles were grown in the insulating host when temperature increased, making the material metallic.[168] The transition speed is very high with the typical time scale on the order of sub picosecond. In addition, the transition is completely reversible. With the advantages of low temperature, high speed and reversible transition, VO_2 in thin film status has considerable application in memory, optical switching devices, absorber and transparent conductor. The application of VO_2 thin film relies on the large change of the electric and optical properties during the phase transition. The conductivity increases several orders from the semiconducting phase to the metallic phase. Furthermore, the reflectivity and the transmittance vary a lot during the phase change.

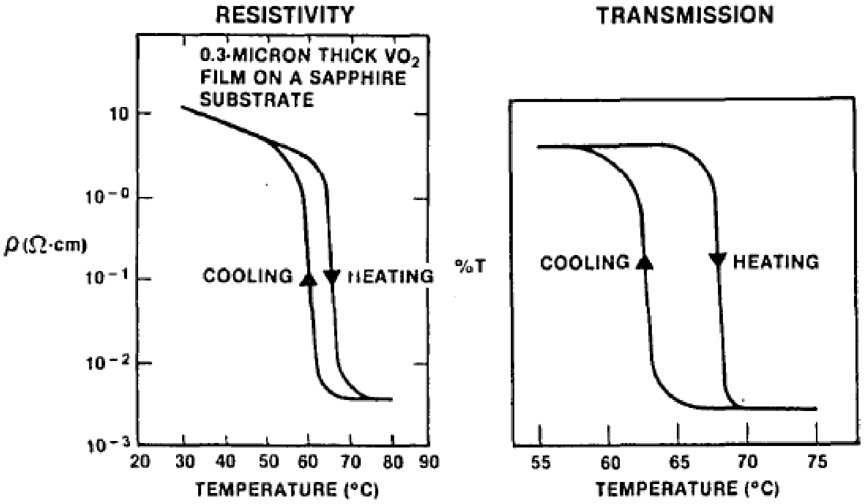

Figure 4-2 Electric and optical properties of VO_2 thin film versus temperature change. (a) resistivity in the heating the cooling circle. (b) transmission in the heating the cooling circle. Adapted from Chain, E. E.[169]

As shown in figure 4-2, the resistivity of 300 nm thick VO_2 change about four orders of magnitude near the phase transition temperature around 65℃. It is important to point out that the phase transition of VO_2 has hysteretic character as shown in figure 4-2 both for the resistivity and transmission. Hysteresis is the intrinsic property of the VO_2 phase transition. It was reported that both the transition temperature and the width of the hysteresis diagram can be tuned by changing the thin film synthesis method and the condition (like doping) of the synthesis,[170] which can broaden the applications of the VO_2 thin film. In addition, the VO_2 thickness and the preparation process (decides the purity) will also affect the absolute conductivity and transmittance value in each phase. For instance, the resistivity of 100 nm VO_2 fabricated by us has much higher resistivity in semiconducting phase.

4.2 Tunable SRR metamaterials based on VO_2 thin film

4.2.1 VO_2 thin film synthesis

The synthesis of VO_2 thin film was investigated extensively in order to integrate VO_2 to the device for the circuit application. The main challenge of the VO_2 thin film growth is the quality or purity issues. Vanadium and oxygen can form numerous stoichiometric phases, some of them are also metal-semiconductor transition materials such as V_2O_5, V_2O_3, while there are many other oxide phases which are no longer metal-semiconductor transition materials like VO, V_7O_{13}.[171] The coexistence of different oxide phases lead to the competition between the stoichiometric phase during the growth, making it challenging to achieve high purity VO_2 thin film. The growth condition is extremely critical to eliminate the x factor in VO_x. Besides the stoichiometry issues, the physical and chemical properties of VO_2 are directly dependent on the growth method and condition. For instance, the substrate used to support VO_2 will affect the crystalline properties and the morphology will also affect the transition characteristic such as the transition temperature and the hysteresis loop width.

The growth of VO_2 can be classified into two strategies, namely, reduce the vanadium compound or vanadium oxides with valence state higher than 4 into VO_2 or oxidize the metallic vanadium into VO_2. Several methods such as chemical vapor deposition (CVD), pulsed laser deposition (PLD), sol-gel method and sputtering have been developed to grow VO_2 thin film with high quality.[172] CVD is a common method to reduce the organometallic precursors such as vanadium oxychloride ($VOCl_3$) or vanadium acetylacetonate $(C_5H_7O_2)_4V$ into VO_2 by controlling the gas species and pressure.[173, 174] Sometimes the main product of the reduction is V_2O_5 and it is necessary to further reduce V_2O_5 into VO_2 by annealing it around 500-1000℃ with appropriate oxygen partial pressure. PLD is widely used in thin film deposition especially for the oxide growth, in the case of VO_2, the metallic vanadium target is ablated by a high power laser in a high vacuum chamber with the mixture gas of argon and oxygen.[175] The substrate temperature, the ratio of oxygen and the post-annealing process are critical to produce high quality VO_2 thin film. The sol-gel method is a wet chemical technique which is suitable to synthesize metal oxide in low cost, high stability and in large scale. For the VO_2 case, the precursor solution such as vanadium isopropoxide ,$VO(OC_3H_7)_3$, is spin coated on the substrate followed by a drying process to remove the solvent, and then an annealing process is applied to produce a homogeneous VO_2 thin film.[176] One advantage of the sol-gel method is that it can enable the doping of VO_2 readily.

In this thesis, we take the sputtering method to grow the VO_2 thin film on sapphire substrate. The sputtering method is similar to the PLD method that a metallic vanadium target utilized and mixture gas (Ar and O_2) is necessary. As we discuss in the Chapter 1, the target atoms are ejected by the ions bombardment. In the sputtering methods two factors decide the quality of VO_2 thin film, which are the oxygen ratio and the temperature.

It has been reported that the oxygen ratio between 10-25% was more suitable to obtain high quality. Too low oxygen content will result in the products like VO_x (x<2), while too high oxygen content will lead the over oxidation and V_2O_5 will be the dominant product.[177] The morphology of the thin film will be also influenced by the oxygen ratio because it will change the collision condition between the vanadium atoms and the ions. In addition, higher oxygen ratio will give a smaller deposition rate because an oxide layer generated on the target surface will reduce the deposition rate. Most importantly, the electrical and optical properties are dependent on the oxygen ratio. The thin film synthesized under lower oxygen content will behave more like a metal, in addition, higher refractive index n and extinction coefficient k will be present. The resistivity difference between semiconducting and metallic phase is also affected by the oxygen ratio.[177] The growth characteristic and the properties of VO_2 are also dependent on the deposition temperature.

It was reported that for VO_2 thin film sputtering, the temperature can be divided into three regions. For 350℃< T< 435℃, the thin film was presented as array of poorly defined grains with the size 0.1-0.3 μm. Additionally, the temperature is not enough to push the oxidation to VO_2 and the thin does not have the metal-semiconductor transition characteristic. Thin film deposited at 505℃< T< 570℃ has oriented grains with the size 0.3-1.0 μm. The main component of the film in this temperature range is VO_2, while the resistivity change during the phase transition is smaller than pure VO_2 and the transition temperature is usually higher than normal transition temperature 68℃. The third temperature region is 585℃< T< 620℃, the thin film in this region appear as well defined grains with larger size around 1-2 μm, the connection between the grains are better than those in lower temperature and the optical and electrical properties are optimized in the third temperature region.[178]

In this thesis, the VO_2 thin film was grown by a DC unbalanced magnetron (UBM) sputtering system (Astar, Singapore), and the target is metallic vanadium with the purity of 99.9%. The base pressure of the chamber is 7×10^{-7} mbar. The deposition temperature was 600℃ and the gas filling in the chamber is the mixture of Ar and O_2 with the ratio of 6:1. The sputtering power we used is 275 W. The pre-sputtering of the target in oxygen-free condition is necessary before each deposition in order to remove the oxide layer on the target surface. The substrate we use is commercial c-cut sapphire substrate with a 2-inch diameter and the sample holder can be rotated to make the thin film as homogenous as possible. The deposition duration is 30 mins and the thickness is around 100 nm. The orientation of the VO_2 thin film is (001).

The resistance of the thin film during the phase transition was measured to qualify the quality of the VO_2 thin film by four probe method with a physical property measurement system (PPMS) apparatus. The resistance shown in figure 4-3a indicates a large change of the conductivity during the phase transition, it is about 2 Ohms at metallic phase while 10,000 Ohms at the semiconducting phase. The difference of the resistivity is about four orders of magnitude, which suggests that the as-synthesized VO_2 thin film is of high quality. It is clearly shown that the resistance behavior of the VO_2 thin film is hysteric and the transition temperature is about 348 K. In addition, we can also observe a large change in reflectivity and transmittance, the sample seems darker and less transparent in high temperature metallic phase.

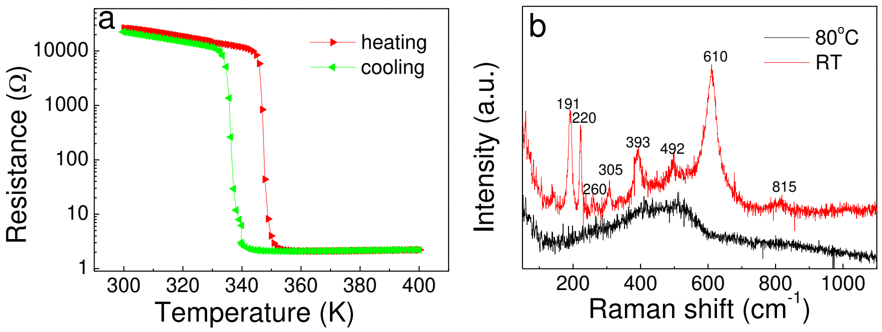

Figure 4-3 Phase transition of VO_2 thin film (a) resistance of the thin film depends on the temperature in a heating/cooling cycle. (b) Raman signal of the thin film at room temperature and 80℃.

We also conducted the Raman measurement to confirm the phase transition of VO_2 thin film with our Horiba-JY T64000 micro Raman spectrometer, with an excitation laser of 532 nm with a power of 1.25 mW. The power was carefully chosen to avoid noticeable heating due to laser irradiation. As shown in figure 4-3b, series of vibrational modes were observed in the semiconductor phase at room temperature as labelled, while those modes were absent in the metallic phase when the sample was heated up to 80℃. The Raman modes difference between the metallic and semiconductor phase suggests that the structure of VO_2 indeed change when it undergoes phase transition. VO_2 in metallic phase has the rutile structure with the space group D_{4h}^{14} while VO_2 in insulating phase has the monoclinic (distorted rutile) structure with the space group C_{2h}^{5} (subgroup of D_{4h}^{14}). Theoretically, five modes in metallic phase (A_{1g}, B_{1g}, B_{2g}, E_g) and nine A_g and nine B_g modes in insulating phase are Raman active.[179] The Raman mode in insulating phases is relatively sharp and easy to observe, however, the Raman mode in metallic phase is very broad with the full width of half maximum larger than 100 cm^{-1} and several modes mix together to make it difficult to observe directly. As shown in figure 4-3b, the broad mode 510 cm^{-1} in the high temperature (metallic phase) is attributed to the A_{1g} symmetry. All the peaks we observed such as 191, 220, 393, 610 cm^{-1} in room temperature (semiconductor phase) are attributed to the A_g mode.[180]

4.2.2 Tunable optical response

We choose the split ring resonator as the metamaterials elements to demonstrate the tunability and activity of the VO_2 based device. The electric mode of SRR resulted from the electric dipole excitation of the bar is sensitive to the refraction index of the environment in the same manner of all the plasmonic structures utilized in sensing application, while the magnetic mode resulted from the "LC" oscillating circuit is affected by both the refraction index and conductivity of the gap because the refraction index change in the gap will affect the capacitance and the conductivity change is related to the connection of the gap. In principle, the integration of SRR metamaterials can make it possible to tune the electric and magnetic mode simultaneously because the pronounced change of the optical and electric properties of VO_2 during the phase transition.

We fabricated the SRR arrays on the VO_2 thin film directly with EBL. The charge effect was absent during the EBL process because VO_2 is in semiconducting phase at the room temperature. However, compared to the conductive substrate like silicon, we should use lower dosage to obtain optimal pattern fabrication. Follow the standard EBL process as described in chapter 2 and the evaporation process, 30 nm thick SRR arrays were fabricated on the VO_2 thin film directly as shown in figure4-4.

The interaction between two adjacent SRR in the array is negligible due to the large interval distance. We scale the width *w* of SRR between 30-50 nm whose electric resonance is in the visible – near IR region. It is expected that the resonance shift in infrared range will be larger than visible range because the optical properties change dramatically in the infrared range while the change is not that prominent in the visible range. Beside the infrared region, we also want to explore the behavior of the integrated device in the visible range. As shown in figure 4-4, we use the SRR array with the bar width of 40 nm and the total area of the array is around 50 × 50 μm which large enough for the micro transmission measurement in our Craic 20 system.

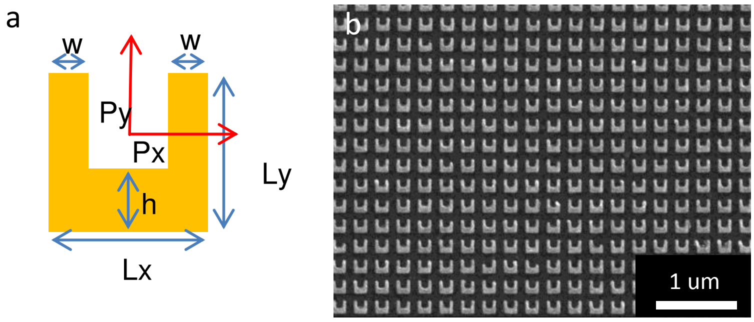

Figure 4-4 SRR array on VO_2 thin film. (a) dimension of SRR, $P_x=P_y=6w$, $L_x=L_y=4w$, $h=1.6w$. (b) SEM image of SRR on VO_2 thin film with the w=40 nm.

The transmission spectra were measured to monitor the optical response on the SRR arrays depending on the phase of VO_2. Because the transmittance of VO_2 is still pronounced in the near IR region, it is convenient for us to measure the transmission. In our experiment, the phase transition was induced thermally by integrating a heating stage and controller to the Craic 20 system as shown in figure 4-5.

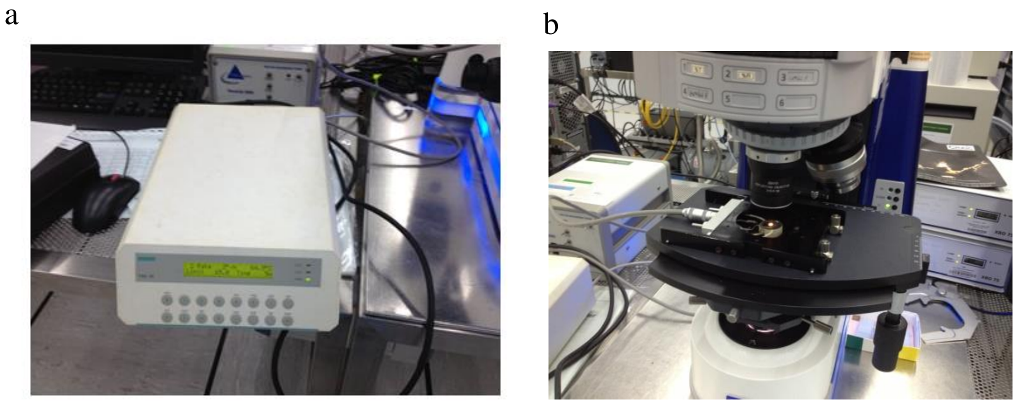

Figure 4- 5 Integration of heating stage to Craic 20 (a) heater controller (c) heating stage on Craic 20 stage

The heater controller (Linkam Scientific Instruments) is capable of controlling the temperature from room temperature up to 600℃ with an accuracy of 0.1℃.The stage was designed with a hole to allow the light pass through for the transmission measurement. The sample was placed on the stage and the area of the SRR array was aligned at the center of the hole. Transmission spectrum was measured in 400-2000 nm range with the temperature variation from 30-80℃. We measure 15 data points in each heating or cooling process and make the temperature interval smaller near the transition temperature.

In order to resolve the electric and magnetic peak as sharp as possible, we did the polarization measurement. As discussed before, both the electric and magnetic mode will be presented when the incidence polarization is parallel to the SRR gap, while only the electric mode will be observed when the incidence polarization is perpendicular to the SRR gap. In the case of parallel polarization, the transmission spectra were shown in figure 4-6a and 6b. As discussed in chapter 1, the transmission spectrum we obtain is the relative value between the sample signal and the reference (substrate) signal. In this case, the transmission of the VO_2 thin film is dependent on the temperature because of the phase transition, we need to measure the transmission of the VO_2 thin film solely at every temperature point to serve as the reference signal so that we can exclude the effects of transmission change of the substrate and make sure the transmission spectra we get can reflect the properties of SRR.

We can observe the high frequency electric resonant mode and the low frequency magnetic mode of SRR in the series of transmission measurement. The electric and magnetic resonance wavelength are 889 and 1580 nm respectively in 30℃ and the resonance wavelength has no change before the sample was heated up to 55℃. The electric mode starts blue shifting while the magnetic mode starts red shifting once the temperature is above 55℃. The shift will be saturated at 80℃ and the final electric and magnetic mode are 816 and 1706 nm respectively. During the cooling process, the electric mode starts red shifting and the magnetic mode starts blue shifting at the temperature of 70℃, consequently both the electric and magnetic resonance frequency will return to the initial status at the temperature of 30℃.

The minimum we observe in figure 4-6a and 6b around 580 nm is the high order mode of the SRR arising from the width of the bar, which is not sensitive to the surrounding environment, so that we cannot observe any shift of this high order mode although the phase transition did occur. The extracted electric and magnetic resonance wavelength at each temperature point in a whole heating/cooling were plotted in figure 4-6c and 6d respectively. We can clearly observe the hysteresis phenomenon which is consistent with the intrinsic property of the VO_2 in the phase transition cycle we observed in figure 4-3a.

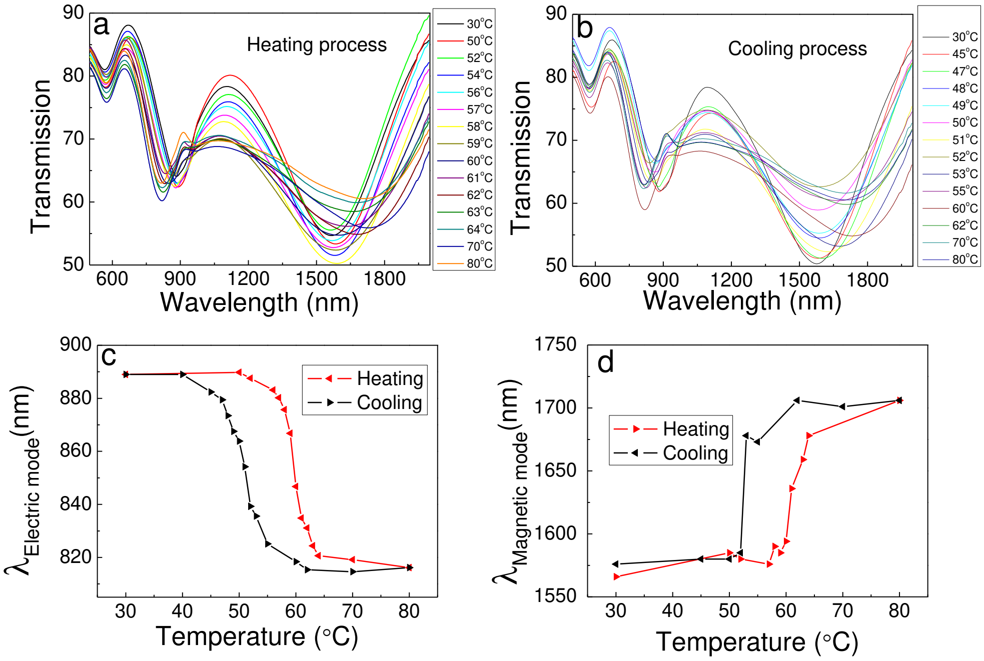

Figure 4-6 Temperature dependent transmission when incidence polarization is parallel to the SRR gap. (a) transmission spectrum in the heating process from 30℃to 80℃, electric mode blue shifts while magnetic mode red shifts (b) transmission in the cooling process from 80℃ back to 30℃,electric mode red shifts while magnetic mode blue shifts in contrary to the heating process. (c) extracted electric resonance wavelength in the heating/cooling cycle. (d) extracted magnetic resonance wavelength in the heating/cooling cycle. Note: both the electric and magnetic modes are hysteric in a phase transition cycle.

In general, both electric and magnetic modes will red shift after adding an analyte in the sensing application. However, in this SRR/VO_2 device the electric and magnetic mode shift in an opposite trend, one is blue shifted while another one is red shifted. This opposite trend can be explained by considering the refractive index and permittivity change of VO_2 during the phase transition.

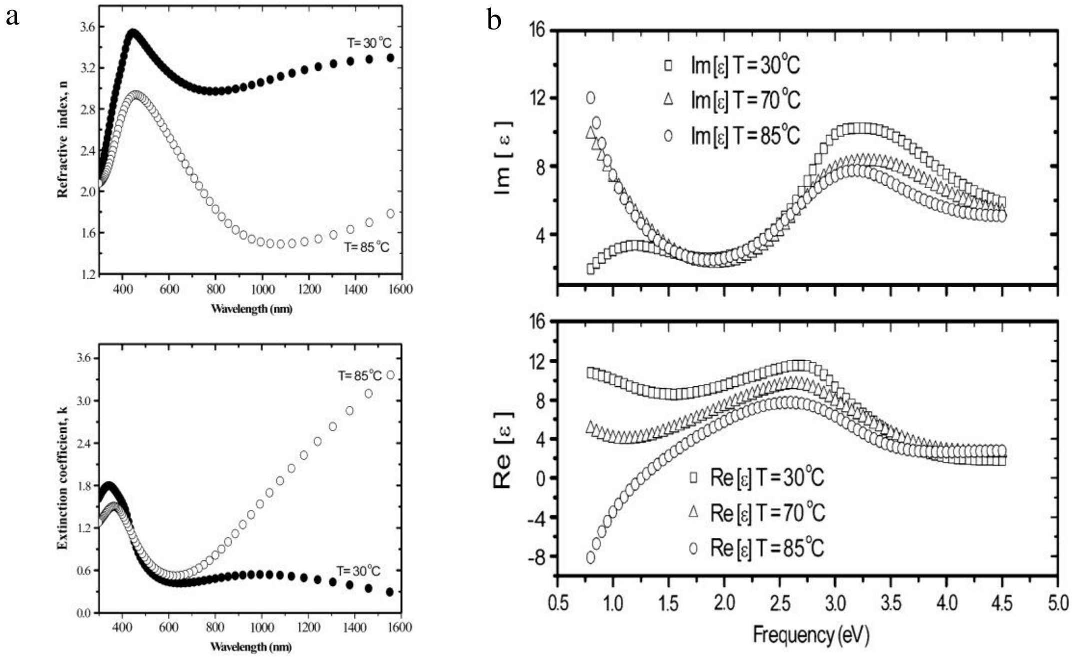

Figure 4-7 Dielectric property of VO_2 during phase transition. (a) refractive index in semiconductor and metallic phase (b) permittivity in semiconductor and metallic phase. Plot adapted from J.B. Kana Kana.[181]

All the literature showed that the magnetic mode red shift when VO_2 transit from semiconducting to metallic phase.[163, 182] The magnetic resonance frequency is proportional to $(LC)^{-1/2}$ while the capacitance of a SRR can be expressed as $C = \varepsilon_0 \varepsilon_{eff} \, {}^{wt}\!/_{d}$ based on the capacitance formula of the parallel plate capacitors[183] , here *w, t, d* are the dimensions of the SRR, ε_{eff} is the effective permittivity of the SRR gap. Usually ε_{eff} is the average of the permittivity of air and the substrate based on the distribution of the electric field in the gap. As shown in figure 4-7b by J.B. Kana *et al.*, the VO_2 thin film has larger permittivity in high temperature, so that the capacitance will increase and the resonance frequency will decrease with the increasing temperature. In terms of the electric mode, the resonance frequency behaves in the same manner with other plasmonic structures that the larger refractive index will render the resonance frequency red shift. As indicated in figure 4-7a, VO_2

thin film has smaller refractive index at high temperature in the visible-near infrared range, so that the electric resonance frequency will blue shift when the SRR/VO_2 device is heated.

Apart from the resonance frequency shift, the magnetic mode becomes broader and has the tendency to vanish with increasing temperature, which is the result of the large conductivity change during the VO_2 phase transition. The VO_2 substrate is very conducive at high temperature (figure 4-3a) and it intends to short the gap and make the SRR a closed ring. The magnetic mode of a closed ring is inactive if it is excited by a normal incidence light. No matter what the incidence polarization is, in this symmetric closed ring, the circulating current inside an arm is cancelled by the current inside the opposite arm, consequently the superposition of the circulating current is zero and no magnetic momentum will be induced. The magnetic momentum can only be presented by inducing asymmetry, for instance by creating a gap, and then excite it by a normal incidence light with the polarization parallel to the gap. In our case, the metallic substrate has the trend to connect the gap so that the magnetic resonance peak becomes broader. However, the metallic VO_2 substrate cannot connect the gap completely because the air in the gap is still there so that the magnetic mode will not disappear completely.

We also measure the transmission when the incidence polarization is perpendicular to the gap as shown in figure 4-8. As predicted, only the electric mode is presented under the perpendicular polarization. The perpendicular polarized light can only excite the dipolar momentum of the left and right arm of SRR, the coupling of the two electric dipoles give the electric mode as observed in experiment. Compared with the electric mode arising from the single bottom arm of SRR in the parallel polarization, the resonance of the two coupled dipole pairs is red shifted.[184] As observed in figure 4-8, we can only resolve an electric mode in this perpendicular polarization and the resonance wavelength is red shifted about 110 nm compared with the parallel polarization at the temperature of 30℃.The electric resonance wavelength is blue shifted from 1050 to 960 nm in the heating process from 30 to 80℃, and it red shifts back to the initial status if we cool the device from 80 to 30℃ as shown in the cooling process. The behavior of the electric resonance shift in the perpendicular polarization is in the same manner as the parallel polarization.

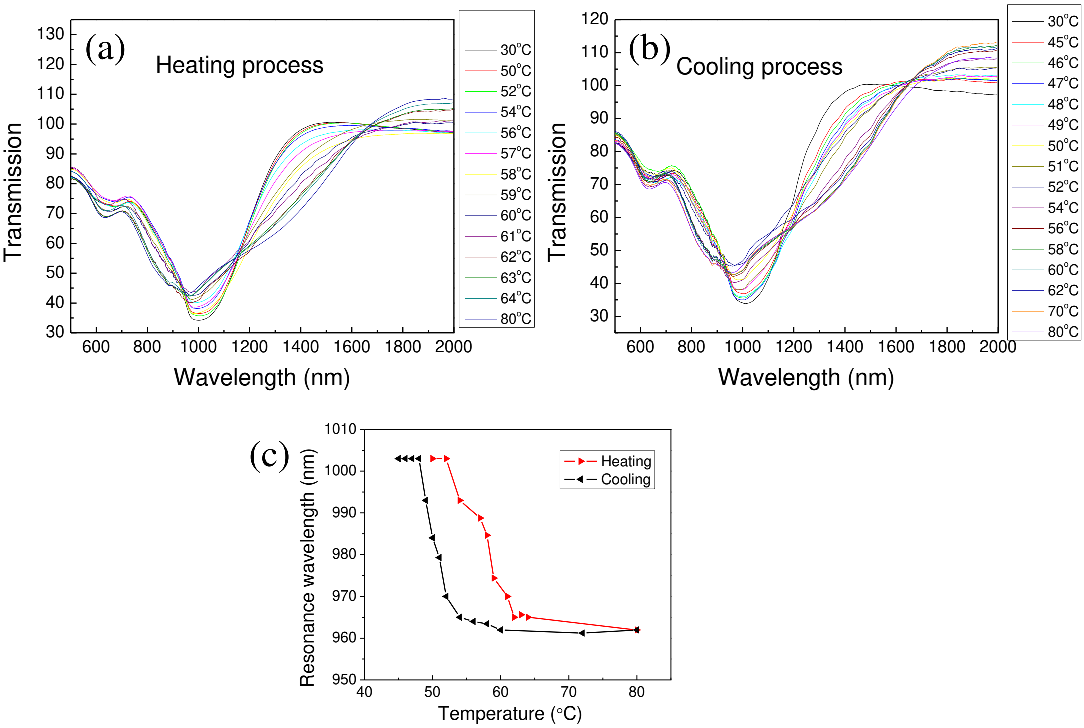

Figure 4-8 Temperature dependent transmission when incidence polarization is perpendicular to the SRR gap. (a) transmission spectrum in the heating process from 30℃to 80℃, only electric mode is presented and blue shifts (b) transmission in the cooling process from 80℃ back to 30℃,electric mode red shifts (c) extracted electric resonance wavelength in the heating/cooling cycle.

We can also observe that the electric mode peak in perpendicular polarization (*FWHM* is 273 nm) is much broader than the peak in parallel polarization (*FWHM* is 139 nm), this is because the dipole pairs are symmetrically aligned in the perpendicular polarization and their total momentum is larger, which renders the radiation damping very large, consequently we will obtain a broader resonant peak.

4.2.3 Tunable surface-enhanced Raman Scattering

Based on the SERS mechanism that the resonant structure enhances both the incident and the Raman scattered fields, we have to match the frequency of incidence light, resonant structure and Raman scattered signal to optimize the SERS intensity. However, the incidence laser wavelength is limited by the laboratory facilities and most of the time the laser we used is in a discrete line, the resonance frequency of plasmonic or metamaterials structure is fixed when the fabrication process is completed, and the Raman scattered signal is determined by the analytes to be detected. All these factors we list above will impose limitation to achieve the highest SERS intensity. Herein, the tunability of the resonance frequency in our SRR/VO_2 device provide a good platform for us to tune the matching condition between the frequency of incidence light, resonant structure and the Raman scattered signal to optimize the SERS intensity. For instance, with a fixed lase wavelength a certain Raman scattered signal, we can tune the resonance frequency of SRR to tune the SERS signal in real time.

We attach a monolayer of 2-naphthalenethiol molecules on SRR to demonstrate the tunable SERS. As we discussed in chapter 3, the electric mode of SRR is capable of enhancing the Raman signal. We use the SRR with the arm width of 30 nm and its electric resonance is 763 nm at 30℃. For the Raman measurement, we take a 785 nm solid state laser with the power of 2.5 mW as the excitation source. The SERS signal of 2-naphthalenethiol molecule at 30℃ is shown in the black curve in figure 4-9b. Here, we just show the ring-ring stretching Raman mode at 1379 cm^{-1} for the demonstration. When the sample is heated up to 80℃ , the electric resonance frequency of SRR blue shifts to 753 nm because of the phase transition of VO_2 film. The SERS intensity of 2-naphthalenethiol molecule at 80℃ is shown in the green line in figure 4-9b, and we can observe a 2.4 time lower in the SERS intensity when the sample is heated up. Once the sample was cooled back to 30℃, both the electric resonance wavelength and the Raman intensity will return to the initial status, suggesting the Raman tuning is in real time and reversible.

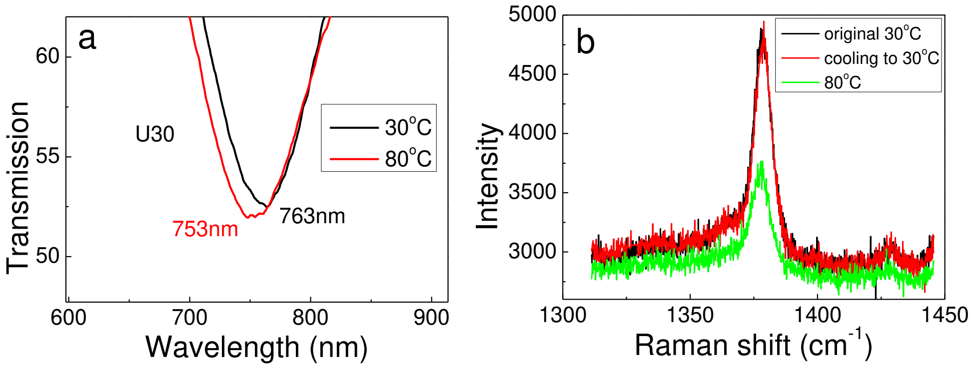

Figure 4-9 Tunable surface-enhanced Raman scattering. (a) electric resonance wavelength of SRR with the arm width of 30 nm (b) Raman intensity of 2-naphthalenethiol at different temperature. Black line is the signal in initial 30℃, the green line is the signal when heated up to 80℃ and the red line is the signal when cool it back to 30℃. Note: the excitation laser wavelength is 785 nm.

We attribute the change in Raman intensity to the change of matching condition of the laser wavelength and the electric resonance frequency. In this case, the interval between the laser wavelength and the resonance wavelength is 22 and 32 nm at 30 and 80℃ respectively. As we know the smaller gap between laser and resonance wavelength will give stronger field enhancement and higher SERS intensity as well, so that we can observe higher SERS intensity in 30℃. This case shows that the Raman intensity can be altered in real time by inducing the phase transition of VO_2 with the controlled temperature. According to the laser wavelength, we can also select a specific size for our application. For instance, we can make the resonance frequency closer to the laser frequency at high temperature to make Raman intensity higher at high temperature in contrary to what we demonstrated above. It is even possible to make the “SERS ON” at one temperature while “SERS OFF” at another temperature when the resonance frequency shift is large enough.

4.3 Summary

The tunability and activity of the properties of metamaterials are critical in the real device application. The combination of metamaterials and phase change materials is very promising in the active metamaterials construction. VO_2 is a typical phase change material which undergoes the insulator-metal transition at the temperature of 68℃. The large change of the optical and electric properties of VO_2 during the phase transition can be utilized to induce activity to metamaterials. The growth of VO_2 thin film is nontrivial because the presence of other vanadium oxide components affects the purity and quality of the thin film. In this thesis, the VO_2 thin film was grown by sputtering method and high quality VO_2 thin film on sapphire substrate can be attained by controlling the temperature and the oxygen ratio. The large change of the resistance and the clear structure change revealed by the Raman spectrum indicate the as-grow VO_2 is in high quality.

We then hybridize the SRR metamaterials on to the VO_2 thin film to attain the tunability of the optical response of SRR. We have demonstrated that both the electric and magnetic mode can be tuned by inducing the phase change of VO_2 with controlled temperature. The electric resonance frequency blue shifts while the magnetic resonance frequency red shifts during the phase transition from semiconductor to metal, and the resonance frequency will return the initial status after cooling it back to the initial temperature. We attribute the resonance shift to the refractive index and permittivity change during the phase transition. The decrease of the refractive index is responsible for the blue shift of electric mode and the increase of the permittivity is responsible for the red shift of the magnetic mode.

The tunability of the resonance frequency can be utilized to achieve tunable surface-enhanced Raman scattering. For a fixed laser wavelength, the change of the resonance wavelength can change the frequency matching condition between the incidence light and the resonance wavelength to alter the SERS intensity. We demonstrate that the SERS intensity of 2-naphthalenethiol can be changed in real time by inducing the phase change of VO_2 with different temperature. We can predict that larger resonance shift can render a larger change of SERS intensity, we can even make the SERS signal “ON” at one temperature while “OFF” at another temperature, suggesting the SRR/VO_2 active device has potential in the switch application. Apart from the metamaterials, many other plasmonic structures can be hybridized on to the VO_2 film to realize the property tunability. What's more, the phase transition stimuli is not only limited to temperature change, many other physical factors such as electric field, magnetic field and strain are possible to induce the phase transition, which broadens the application of the phase change material based active plasmonic or metamaterials devices.

Chapter 5 Magnetic Mode-based Fano Resonance in Split Ring Resonator/Disk Nanocavity

5.1 Introduction

Localized surface plasmon resonance (LSPR) was widely used in the biological and chemical sensing because the LSPR resonance frequency is sensitive to the change of refractive index of the environment. The sensitivity is one of the critical issues that motivate the community to explore different methods to pursue higher sensitivity and figure of merit (FOM). One direct strategy is to engineer the extinction intensity, spectra linewidth and the field decay length by optimizing the design of the size, shape and material component of the nanostructures. In principle, larger ratio between height and length of the nanostructure will give a higher sensitivity. For instance, structures featured with a sharp tip are usually designed to enhance the sensitivity due to higher field confinement near the tip.[185] In addition, the materials with smaller decay length and narrower linewidth are preferred to achieve higher sensitivity to local refractive index. Another notable method is to utilize the coupled structure to increase the sensitivity. As we know the coupled structure can give higher field confinement in the gap which will be responsible for the increasing sensitivity. The sensitivity can be tuned by changing the distance between two nanoparticles.[186] It has also been reported the coupled system can provide a theoretic limit of sensitivity.[187] Besides the nanostructure array, a single nanoparticle has been proposed to enhance the sensitivity. Usually a single nanoparticle has a narrow spectra linewidth. In addition, single nanoparticle can enhance the spatial resolution of detection. The drawback of the single particle is that the low signal intensity is not convenient to detect.

Recently, Fano resonance has attracted tremendous attention in the sensing application with high sensitivity and FOM. The asymmetric and ultra-narrow spectra line can enhance the sensitivity and FOM dramatically. Numerous of plasmonic or metamaterials structures have been designed to realize Fano resonance. Most of them are based on the electric-electric coupling, in this thesis we will introduce the Fano resonance based on the magnetic-electric coupling in split ring resonator/disk cavity and demonstrate the tunable Fano resonance and their application in sensing. First of all, we will introduce some basics of Fano resonance and the electric mode and magnetic mode based Fano resonance, then we will discuss our experimental and simulation results on the SRR/disk cavity.

5.2 Fano resonance

5.2.1 Basics of Fano resonance

The resonance describes the increase of the vibrating amplitude of a system when it is stimulated by an external force with a certain frequency. The resonance frequency is referred as the eigen frequency which is determined by the system itself. The resonance is a universal phenomenon which exists in many systems such as the acoustic, mechanic, optical and atomic systems. Initially, the lineshape of all the resonances can by summarized by the Lorentzian function as

$$I(w) \propto \frac{(\Gamma/2)^2}{(w-\Omega)^2 + (\Gamma/2)^2} \tag{5-1}$$

Here Ω is the eigen frequency of the system and w is the frequency of the external force, Γ describes the damping of the oscillation which determines the width of the spectra line. It is noticeable that the resonance peak under Lorentzian function is symmetric and the magnitude is in maximum when the external force frequency is identical to the eigen frequency of the system. Indeed, many resonant systems can be described by Lorentzian function successfully. However, the asymmetric lineshape observed by Beutler in the absorption of the noble gases, which made people reconsider the universality of the Lorentzian function.[188] It was Ugo Fano who firstly came up a new formula which was known as Fano formula to explain the asymmetric spectra line as observed,[189] the success of the Fano formula made this special resonance named after Ugo Fano, namely, Fano resonance. Fano interpreted that the asymmetric lineshape arised from the interference between a discrete excited state and a continuum excited state as shown in figure 5-1a. In the case of atomic system, the discrete and continuum states refers to the autoionization state (Auger effect) and ionization state respectively.

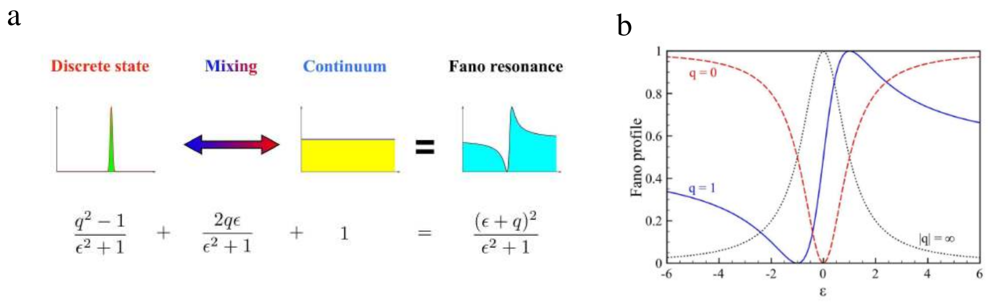

Figure 5-1 Fano formula and Fano profile (a) the symmetric Lorentzian discrete state interfere to the continuum state to create a Fano resonance. (b) the Fano lineshape for different value of asymmetry parameter q. figure adapted from Andrey E. Miroshnichenko.[190]

The Fano formula describes the scattering cross section as[190]

$$\sigma = \frac{(\varepsilon + q)^2}{\varepsilon^2 + 1} \tag{5-2}$$

here ε is the reduced energy and q is the asymmetry parameter. q is defined as the ratio of the transition probability to the discrete state and continuum state. When q is infinity, which means the transition to the discrete state is dominated and the spectra line can be represented by the Lorentzian function as shown in the gray line in figure 5-1b, so that Lorentzian resonance is a specific case of the Fano resonance with infinite q. If q is unity, the transition to discrete state and continuum state is competitive and the line shape is no longer symmetric as shown in the blue line in figure 5-1b. In the case of q is zero, it is an anti-resonance phenomenon in which the magnitude is minimized in the resonance frequency and the spectra line is presented as minimum as shown in red line in figure 5-1b. It is clear that if q is finite (nonzero), the coexistence of the transition to the discrete state and continuum sate will interfere with each other to result in a Fano resonance. Following the first discovery, numerous efforts have been dedicated in the investigation of Fano resonance and the Fano resonance was demonstrated in various systems such as the atomic, nuclear, photonic and plasmonic system.[191-193]

5.2.2 Fano resonance in plasmonics structure

Fano resonance was not only limited to the quantum systems, the first observation of Fano type asymmetric lineshape in optics was the Wood's anomaly, which opened the door of the Fano resonance in other specific systems.[194] Recently, Fano resonance exhibited in plasmonics or plasmonic element based metamaterials system has attracted tremendous attention. The collective oscillation of the electrons in plasmonics structure is in analogy to the conventional oscillators and the plasmonics structure is a typical coupled oscillator system on the nanoscale.

Over the past years, the theoretical study of the plasmonic structure has been greatly matured. The coupling behavior in a complex plasmonic structure can be revealed by plasmon hybridization method. As we know, in the molecular system, the wave function of each atomic state interacts with each other to generate a molecular orbit. Plasmon hybridization (PH) method assumes that the plasmon of the individual elements in a complex structure interact with each other in the same manner as the quantum system and the behavior of the whole complex system is reflected by the superposition of those individual plasmon.[105, 195] PH method provides an intuitive, convenient and simple picture to analyze the interaction between plasmons and evaluate the properties of a coupled plasmonic structure. For instance, the optical response of a dimer can be treated as the interaction between two dipoles sustained inside the nanoparticles. The parallel or anti-parallel alignment of the dipoles will render resonance frequency red shift or blue shift compared to the single particle. The origin of Fano resonance in plasmonic or metamaterials structure also can be explained with the PH theory, in which the weak interaction between a sub-radiant (dark) mode and a super-radiant (bright) mode produces a Fano spectra lineshape. As we know, when the size of the nanoparticle is much smaller than the incidence wavelength, only the dipole can be excited while the higher order mode is inactive. Usually the excited dipole is radiative and can strongly couple to the incidence light to produce a broad peak, which is the bright mode. On the contrary, the dark mode is non-radiative and it couples to the incident light inefficiently because of the near zero net momentum. Another characteristic of the dark mode is that the spectra peak is very narrow due to the negligible radiative damping loss. For the Fano resonance in a plasmonic structure, the dark mode with narrow spectrum serves as the discrete state and the bright mode with broad spectrum serves as the continuum state. Fano resonance in plasmonic structure will be created once the discrete state and continuum state overlap in resonance frequency energy.

Unfortunately the dark mode (like the higher mode in a nanoparticle we discussed on last paragraph) is normally inactive, a common method to render the dark mode active is by introducing the symmetry breaking to the plasmonic structure. In a symmetric configuration, the coupling between the dark mode and bright mode is forbidden and the dark mode is inactive. However, the symmetry breaking will change the point group of the nanostructure belongs to and make the dark mode possible to couple to bright mode, rendering the dark mode active and the Fano resonance observable.

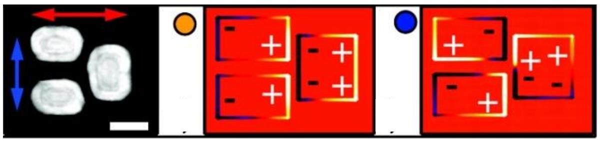

Figure 5-2 Fano resonance in a dolmen structure. Picture adapted from N.Verellen[196]

The first Fano resonance observed in plasmonic structure as shown in figure 5-2.[196] When the polarization is perpendicular to the nanowire on the right (as the red arrow indicated), the structure is still symmetric and only one broad peak can be observed. If the polarization is parallel to the nanowire on the right (as the green arrow indicated), the dolmen is no longer symmetric. The asymmetry will render dark quadrupole of the nanowire pair on the left coupling to the bright dipole mode inside the right nanowire, consequently a Fano resonance can be observed under this specific polarization. Later on, Fano resonance was demonstrated in the SRR/disk and the finite clusters.[197-199] The Fano resonance in plasmonic structure is highly dispersive, which means that a minor change in of the incidence wavelength will induce a large different in the scattering cross section. The narrow lineshape of the Fano resonance in plasmonic and metamaterials structure has considerable potential in the sensing application.

5.2.3 Magnetic mode based Fano resonance

The Fano resonance we discussed before is purely emerged from the interaction between electric modes. Usually the interaction between the electric mode and a magnetic mode in plasmonic is forbidden because they belong to different symmetry group, however, it was reported that the symmetry breaking of the structure can make the electric and magnetic mode share the same symmetry group and interact with each other.[200] The magnetic mode base Fano resonance can provide many benefits, for instance, it can generate intense and tunable optical induced magnetism and it can generate strong magnetic near field which can be utilized to detect the magnetic transition in molecule, in addition, the coupling between magnetic and electric mode make it feasible to manipulate the permittivity and permeability simultaneously to achieve a negative refractive index material.

Due to the absence of magnetism of natural materials in optical range, it is challenging to obtain optical Fano resonance with the interaction between a magnetic mode and an electric mode. As we discussed in Chapter 3, a single SRR is capable of generating a magnetic dipole. However, the resonance frequency of the magnetic dipole is far away from the frequency of the electric dipole so that the interaction cannot occur. Even if they overlap in the resonance energy, Fano resonance will not be presented because the magnetic mode in a single SRR is a bright mode while the Fano resonance requires the magnetic mode as a dark mode. Careful structure design is necessary to create a magnetic dark mode and make it weakly coupled to the bright electric mode. Too strong coupling will also render the Fano resonance disappear because the strong coupling will shift the magnetic mode out of the electric resonance frequency region so that the resonance energy will not overlap. Nanosphere clusters have been demonstrated to be promising in the realization of magnetic mode based Fano resonance.[201]

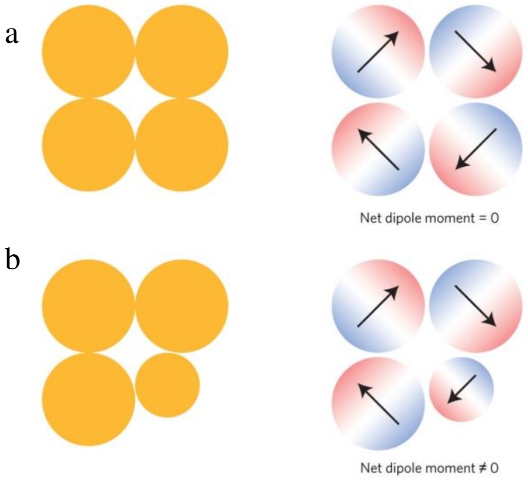

Figure 5-3 Magnetism in a nanosphere cluster. (a) the net dipole moment is zero for a symmetric structure. (b) the net dipole moment is nonzero for an asymmetric structure. Picture adapted from Peter Nordlander.[202]

As shown in figure 5-3, the assembling of the nanosphere is capable sustaining a magnetic momentum due to the circulating current inside the nanosphere.[203] When each nanosphere is identical, the magnetic momentum is zero (figure 5-3a). If we break the symmetry of the nanospheres, a weak magnetic mode can be induced and it can couple to the electric mode to generate a Fano resonance (figure 5-3b). The drawback of the nanosphere cluster is that it is difficult to control the position of the nanosphere. Usually it is controlled under an AFM tip, which is quite challenging. Herein, in this thesis we demonstrate the magnetic mode based Fano resonance in a simple split ring resonator/disk cavity.

5.3 Magnetic mode based Fano in SRR/disk cavity

5.3.1 SRR/disk cavity

Fano resonance in a disk/ring cavity has been demonstrated by moving the disk out from the center of the ring to break the symmetry. However, only the higher order electric mode can be activated in a close ring and the Fano resonance purely arises from the electric interaction. Herein, we introduce a magnetic mode by creating a gap on the ring to break the symmetry. As we discussed before, the magnetic mode will be presented when the incidence polarization is parallel to the gap. In addition to the first order magnetic mode that the circulating current is along the whole ring, many other higher order magnetic modes also can be excited.[184] The higher order magnetic modes are a good candidate to serves as a dark mode to generate a Fano resonance. In order to realize the magnetic mode based Fano resonance, it is necessary for us to make the high order magnetic mode overlap with the electric mode in energy, in this case, the magnetic mode based Fano resonance is impossible in a single split ring because the magnetic mode is always red shifted compared with the electric mode. Herein, we propose a SRR/ring cavity to obtain the magnetic mode based Fano resonance.

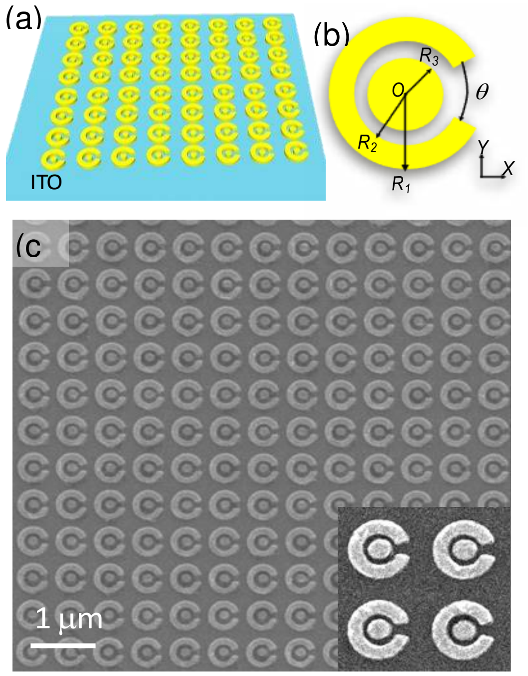

Figure 5-4 Split ring resonator/disk cavity. (a) schematic of SRR/disk array on the ITO glass (b) dimension of the SRR/disk cavity with R_1, R_2, R_3 and θ (c) SEM image of the SRR array with R_1 = 200 nm, R_2 = 110 nm, R_3 = 75 nm. θ= 15°. The thickness is 30 nm and the separation between two units is 150 nm.

The SRR array is fabricated on the ITO glass with EBL method with 50 × 50 μm^2 square as shown in figure 5-4a. The outer radius (R_1) and inner radius (R_2) are fixed at 200 and 110 nm respectively. The radius of the disk (R_3) is varied from 65 to 80 nm to engineer the interaction strength between SRR and disk. The split angle was set from 15° to 120° to change the optical response of the SRR. The representative SEM image of SRR/disk array with R_1 = 200 nm, R_2 = 110 nm, R_3 = 75 nm and θ= 15° is shown in figure 5-4c. It shows that the structure is well defined and the array is uniform and the substrate is clean. Here we want to focus on the response of a single SRR/disk cavity so that we need to exclude the interaction between the adjacent cavities. In order to evaluate the interaction effects between two adjacent SRR cavities, we measure the optical response of the array with the separation from 150 to 750 nm as shown in figure 5-5. The transmission was measured on the Craic 20 microspectrophotometer with polarized incidence light. Split angle of SRR was set as 90° and 120°, the transmission spectra were measured with the polarization parallel to the split gap. Green, blue, red and black indicate the transmission spectra of the SRR array with the interparticle separation of 750, 500, 300, 150 nm. The four spectra are almost the same with three local minimums at around 700 nm, 975 nm and 1300 nm, respectively. The amplitude of the intensity minimum arises from the different structure density per unit area. We can conclude that the interaction between adjacent SRR is negligible and the optical response is the result of the superposition of the single SRR.

In order to interpret the interaction between the disk and split ring, we check the optical properties of the disk and split ring separately first. The transmission of the disk with different diameter is shown in figure 5-6. The resonance wavelength red shifts from 713 to 787 nm with radius increasing from 65 to 80 nm and transmission minimum is the same no matter what the incidence polarization is. The response of the as-fabricated disk array is consistent with the observation in the literature. The response of the SRR will be discussed in detail in the next section.

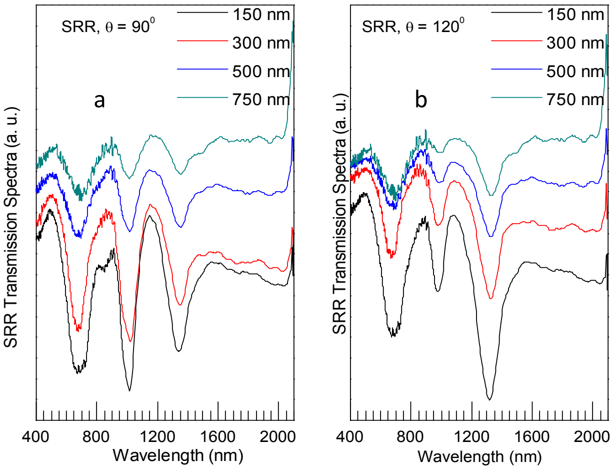

Figure 5-5 Transmission spectra of SRR array with different separation. (a) SRR with the split angle of 90º, the separation is 150, 300, 500, 750 nm (b) SRR with the split angle of 120º, the separation is 150, 300, 500, 750 nm.

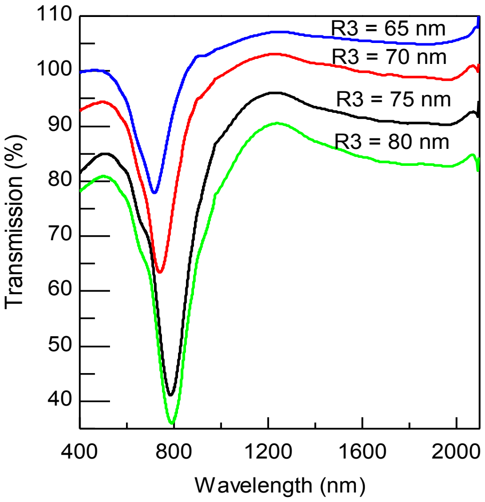

Figure 5-6 Transmission of disk with the radius from 65 to 80 nm.

5.3.2 Multiple magnetic mode based Fano resonance

The polarization dependent transmission of disk, SRR and SRR/disk are measured with Craic 20 spectrometer to investigate the plasmonic mode in each structure as shown in figure 5-7a. The red line indicates the polarization is parallel to the gap while the blue line means the polarization is perpendicular to the gap as the inserted cartoon shows in the first row in figure 5-7a. The SEM image of each as-measured structure is shown in the inserted picture on each row.

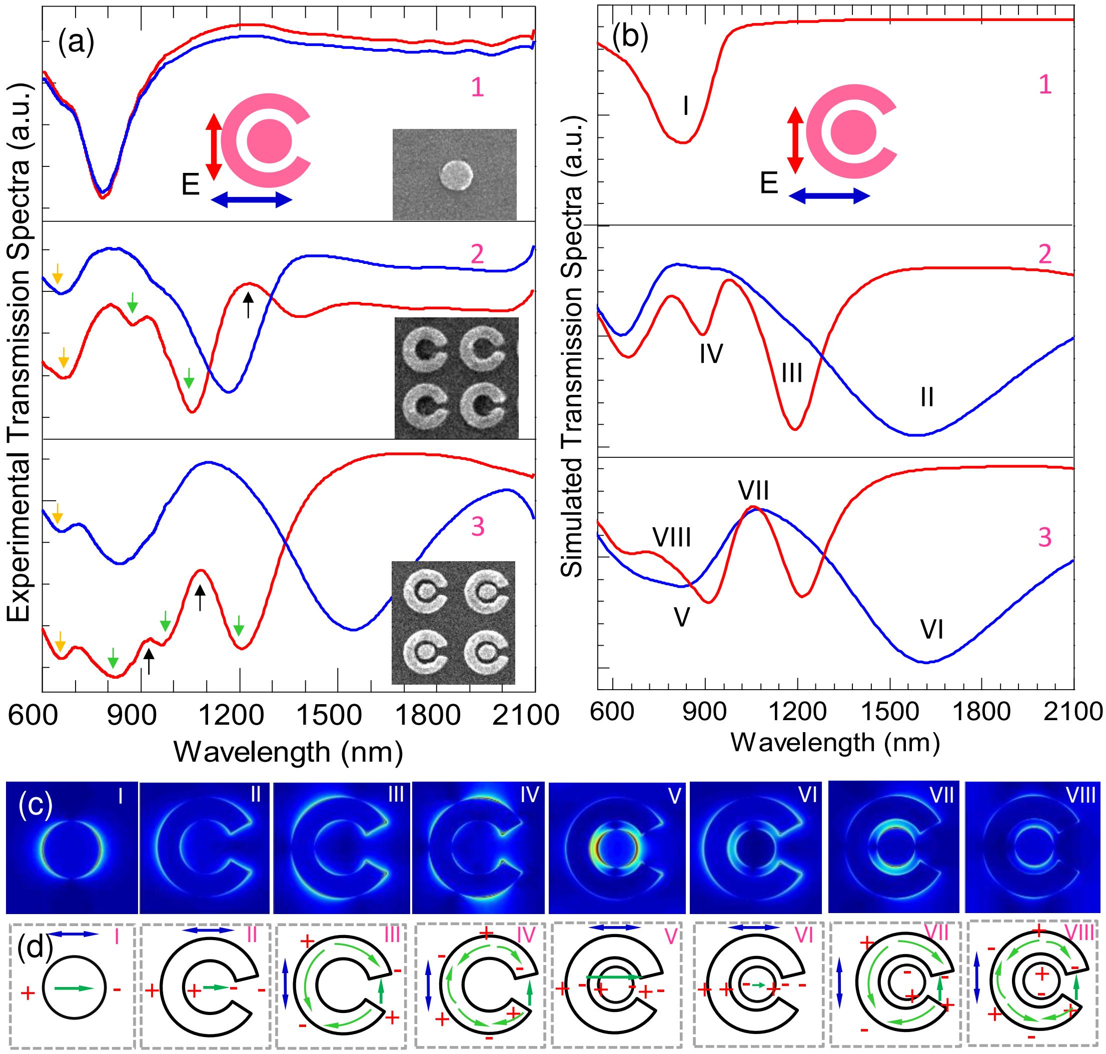

Figure 5-7 Experiment and simulated transmission and electric field distribution of disk, SRR and SRR/disk cavities. (a) and (b) are the experimental and simulated transmission spectra of disk (1), SRR (2) and SRR/disk (3) respectively. The red line is the transmission when the polarization is parallel to the gap while the blue line means the polarization is perpendicular to the gap. The SEM image is inserted in side each row and the plasmonic modes are labelled with number from I to VIII. (c) the FDTD simulated field distribution under each plasmonic mode. (d) simulated charge distribution and displacement current. I: electric dipole of disk, II: electric dipole of

SRR, III: quadrupole magnetic mode of SRR, IV: octupole magnetic mode of SRR. V: anti-bonding resonance between disk dipole and SRR dipole VI: bonding resonance between disk and SRR dipole, VII: quadrupole magnetic mode based Fano resonance arise from interaction between III and VI in SRR/disk, VIII: octupole magnetic mode based Fano resonance arises from the interaction between IV and VI in SRR/disk.

As we discussed before, only one transmission minimum will be presented under both polarization. The minimum of the disk emerges from the electric dipole induced by the excitation and it shows no polarization dependence due to the symmetry. For the SRR under the polarization perpendicular to the gap, the structure is still symmetric and only one dipole resonance can be observed as shown in the blue line in the second row. However, two minimums with the resonance wavelength of 871 and 1060 nm can be observed under the polarization parallel to the gap. In this parallel polarization, the structure is no longer symmetric and the response of the SRR is no long a simple dipole. Previous study showed that high order electric mode such as quadrupole or octupole mode can be excited inside a full ring by breaking the symmetry or using a side illumination.[198, 204] Here we tentatively assign those two peaks as high order mode initiated by the symmetry breaking when the polarization is parallel to the gap and later we will show that they are the quadrupole and octupole magnetic mode. Besides those two minimums (871 and 1064 nm), we also can observe a minimum located at 667 nm as the yellow arrow indicates. We assume this small dip comes from dipole formation due to the arm width of the SRR and it is not sensitive to the structure size. Later we will show that it will not shift with the variation of the split angle.

If the disk is introduced into the center of the SRR to form the SRR/disk cavity and we make the separation between them is short enough to enable the coupling, the disk interacts the SRR with each other via capacitive coupling. The optical response of the combined structure is not simply the superposition of the optical response of the disk and SRR, we should consider them as a group and focus on the coupling mechanism. If the polarization is perpendicular to the gap, the whole structure is symmetric and the dipole of the disk and dipole of SRR hybrid with each other in the plasmon hybridization (PH) manner as we discussed in the first section in this chapter. The hybridization of two dipoles will result in a low energy bonding resonance and a high energy anti-bonding resonance. As expected, we observe two broad dips at 834 and 1546 nm, which are corresponding to the anti-bonding and bonding resonance mode respectively (blue line, figure 5-7a). The observation of the bonding and anti-bonding mode is consistent with what observed in the full ring/disk cavity.[198] Both the bonding and anti-bonding modes observed here are bright modes with broad line width. If the polarization is parallel to the split gap, the high order modes of SRR (871 and 1064 nm) overlap with the broad antibonding mode (834 nm) in energy, so that it is possible for the high order modes weakly coupled to broad bright mode to generate a Fano resonance. In the experiment, we can observe rich spectra feature at the range from 700 to 1300 nm (red curve figure 5-7a), specifically the asymmetric peak at 916 nm is probably arise from the Fano interaction between the octupole magnetic mode (871 nm) and the broad antibonding mode (834 nm). As mentioned before, a minimum at 667 nm arising from the dipole due to the arm width is always presented in both SRR and SRR/disk cavities and appears as no shift (indicated as yellow arrow).

In order to interpret what we observed in experiment and explain the coupling mechanism, we conducted three dimensional finite-difference time–domain (FDTD) simulation to obtain the transmission spectra and the electric field distribution. The simulation is conducted on the commercial software (Lumerical Solution, Inc.) and the gold dielectric from Johnson and Christy is used in the wavelength range from 300-2000 nm.[205] Periodic boundary is adopted and the effect of the air (n=1) and substrate (n=1.54) are also included in the simulation. A plane wave with linear polarization is applied in the simulation to match the optical source in our measurement setup. All the simulation results were recorded on the cross section at the middle of the structure.

The simulated transmission spectra are shown in figure 5-7b and the red line indicates the polarization parallel to the gap while the blue line means the polarization perpendicular to the gap. The observed plasmon modes are labelled in a sequence from I to VIII. The electric field distribution of mode I, II,…VIII are displayed on figure 5-7c. The corresponding charge distribution and circulating displacement current from mode I to VIII are shown in figure 5-7d. Figure 5-7b suggests that the simulated transmission spectra agree well with the experiment transmission spectra. The minor deviation in peak wavelength may come from three factors, the first reason is the real permittivity of the gold has some shift from the data we used in the simulation. Secondly, the size and shape of the fabricated structure is slightly different from what we design in the simulation. Lastly, the roughness of the structure is not considered in the simulation, which renders the peak in the simulation sharper than the experimental observation.

The resonance of an individual disk emerges from the electric dipole resonance, as displayed as mode I in figure 5-7c and 7d, only an electric dipole can be presented no matter under what polarization. Only one minimum can be resolved when the polarization is perpendicular to the SRR (blue line, figure 5-7b-2), the electric field distribution (mode II, figure 5-7c and 7d) confirms that the resonance is purely from the electric dipole resonance. However, two resonance modes (red line, figure 5-7b-2) appear if the polarization is parallel to the split gap, the field and circulating current simulation results are shown in mode III and IV in figure 5-7c and 7d. Based on the charge distribution and the circulating displacement current shown in mode III in figure 5-7d, three partial currents along the SRR surface are resolved. These three partial circulating current cannot cancel with each other and the direct consequence is that a magnetic moment perpendicular to the SRR/disk plane will be generated. We term the magnetic moment initiated from the partial circulating current as high order magnetic mode, which was also reported in the literature.[184] For the mode sustaining three partial circulating current (mode III), we name it as quadrupole magnetic mode, while mode IV is named as octupole magnetic mode because the mode sustaining five partial circulating current (mode IV, figure 5-7d). The first order magnetic mode with the circulating current along the whole SRR at one direction is supposed to appear, however, the simulation shows that the resonance wavelength of the first order magnetic mode is around 3000 nm which is out of our measurement and we only observe the quadrupole and octupole magnetic modes in experiment.

For the SRR/disk cavity, two resonance modes (mode V and VI, blue line, figure 5-7b-3) are resolved under the polarization perpendicular to the split gap. The charge distribution displayed in figure 5-7d indicates that the dipole of the SRR and the dipole of the disk are aligned in the same direction under mode V, which means the SRR and the disk oscillate in the same phase to create an antibonding mode. While the dipole of the disk and the SRR are aligned oppositely under mode VI, which suggests mode VI is a bonding mode with an opposite oscillation phase. Considering the transvers coupling mechanism, the antibonding resonance has higher resonance energy than the bonding mode.[67] In addition, the antibonding mode has larger total electric momentum and it can couple with the incidence light efficiently and the resonance peak will be broad, however, the total momentum of the bonding mode is much smaller due to the momentum cancellation between the disk and the SRR, so that the peak of the bonding mode will be narrower. The transmission simulation that the minimum of mode V is broader than mode VI , which is consistent with our interpretation. As observed in figure 5-7a, the bonding mode (mode VI,1546 nm) is red shift compared with the dipole mode of SRR (mode II, 1170 nm), which is because the existence of the coupling make the resonance red shift. The red shift further confirm the dipole of disk and SRR coupling in a antibonding and bonding way to generate two resonance modes. When the polarization is parallel to the SRR/disk gap, we assume that the antibonding and bonding mode will be still presented because the electric dipole of the SRR is still excited though the symmetry is broken.[197, 206] However, there may be some peak shift because of the different symmetry under different polarization. In the simulated transmission spectra of SRR, we observe a dipole mode when the electric field is parallel to split gap, but the wavelength is out of our instrument measurement range. We also simulated the surface electric field distribution of SRR/D around 945 nm when the electric field is parallel to the split gap, a coupled dipole mode can be seen, as shown in figure 5-8, which confirms the formation of the antibonding mode under the polarization parallel to the gap. Under the polarization parallel to the gap, the quadrupole magnetic mode (mode III) and octupole magnetic mode (mode IV) overlap with the antibonding mode (mode V) in energy, so that the magnetic mode III and mode IV can serve as a sub-radiant (dark) mode to couple to the bright mode V to generate a Fano resonance.

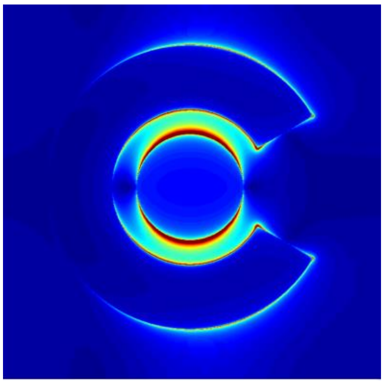

Figure 5- 8 Surface electric field distribution of SRR/disk at 945 nm when the incident electric field is parallel to the split gap.

The minimums of mode III and mode IV will be presented as peaks as Fano resonance mode VII and VIII respectively. In experiment, the quadrupole magnetic minimum (871 nm, red curve, figure 5-7a-2) and the octupole magnetic minimum (1060 nm, red curve, figure 5-7a-2) will be presented peaks in ~961 and ~1080 in the red curve in figure 5-7a-3 respectively. Though the octupole magnetic mode has the larger absorption cross section than the quadrupole, the octupole magnetic mode based Fano strength (more asymmetric as observed) is stronger than the octupole magnetic mode based Fano resonance because the octupole mode has stronger energy overlap with the antibonding mode V. The high order magnetic mode based Fano resonance formation is also supported in the figure 5-7c and 7d in mode VII and VIII, in which the partial circulating current are observable.

In order to have a close look into the electric field and the surface current in mode III, IV ,VII and VIII, we zoom in this picture respectively as shown in figure 5-9. The electric field and the direction of the surface current are clearly shown in the zoom in picture. The partial surface current on SRR generates the quadrupole and octupole magnetic mode in mode III and IV respectively. After introducing a disk to form the SRR/disk cavity, the high order magnetic mode based Fano resonance can be generated as shown in mode VII and VIII. The partial current is still presented under the Fano resonance VII and VIII.

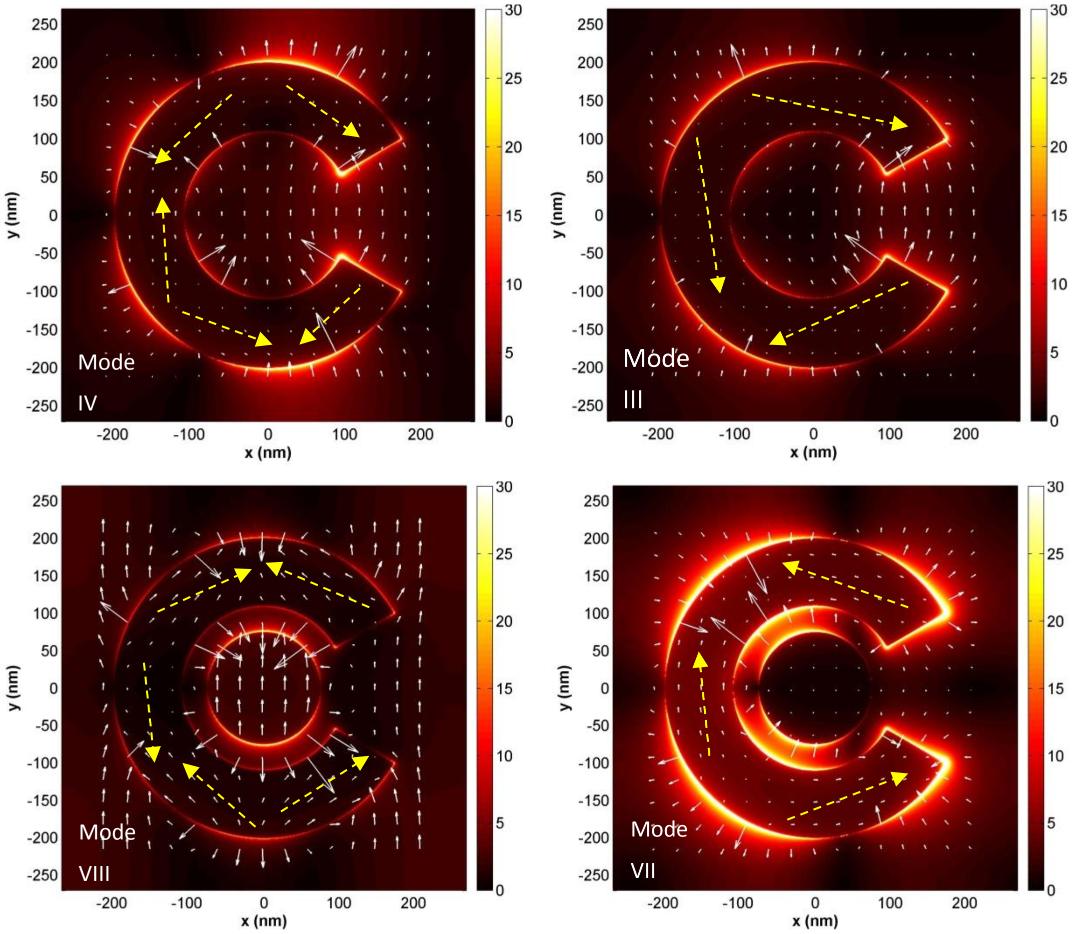

Figure 5-9 Electric field and surface current simulation of mode III, IV, VII and VIII under the polarization parallel to the gap. The white arrows indicate the electric field direction and the length of these white arrows indicate the field strength. The dish yellow arrow means the direction of the partial surface current.

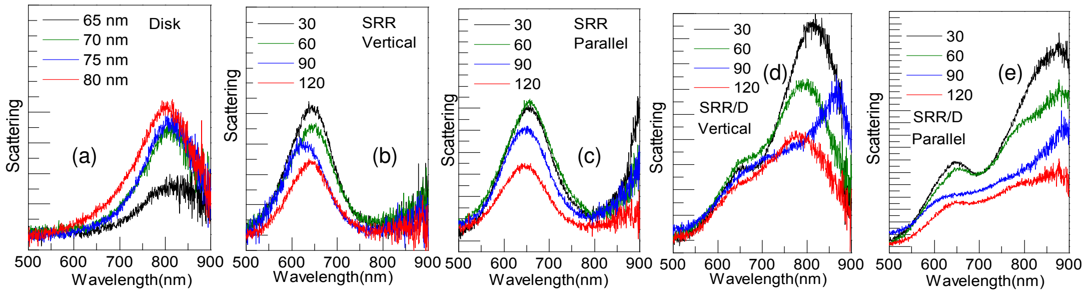

Figure 5-10 Dark scattering of individual cavity. (a) disk (b-c) SRR (d-e) SRR/disk. “Vertical” means the polarization is perpendicular to the gap, “parallel” indicates the polarization is parallel to the gap.

In addition to the transmission spectra, the dark scattering spectra of individual cavity was measured on a home-built dark-field scattering microscope.[207] An Olympus BX60 dark field scattering microscope is equipped with a CCD camera (Princeton Instruments Pixis 512B), a monochromator (Acton SpectraPro 2300i), and a quartz tungsten halogen lamp. The CCD is cooled down to -70ºC during the measurement. A 100× dark field objective with NA with 0.8 was applied for both the excitation and the collection of the scattered light. The scattered signal was corrected by subtracting the background signal from pure substrate without sample. A linear polarizer was put on the light path after the lamp source to achieve the polarization dependence measurement. In this measurement, the cavity array was fabricated with very large interval distance (5 μm) so that we can only measure the response of an individual cavity. The spectra were taken from 500 to 900 nm because of the limited detection range of the detector. The spectra shown in figure 5-10 are consistent with the transmission spectra. The minimums in the transmission will be presented as peak correspondingly in the dark-field scattering spectra. The minor deviation of the peak wavelength is mainly from the different batch of samples in the different measurement.

5.3.3 Manipulation of Fano resonance

It is essential to manipulate the Fano resonance wavelength and the Fano lineshape, which is attainable by engineering the coupling strength of the dark mode and the bright mode. The change of the cavity size and shape can alter the Fano resonance wavelength and the separation between the disk and SRR will alter the coupling strength. Herein, we firstly explore the response change with various split angle of SRR. We set the split angle as 30º, 60º, 90º and 120º for both the SRR and SRR/disk cavities and other parameters are kept same. The experimental and simulation transmission spectra of SRR are displayed in figure 5-11a and 11b, the corresponding SEM image of SRR array is shown in figure 5-11c.

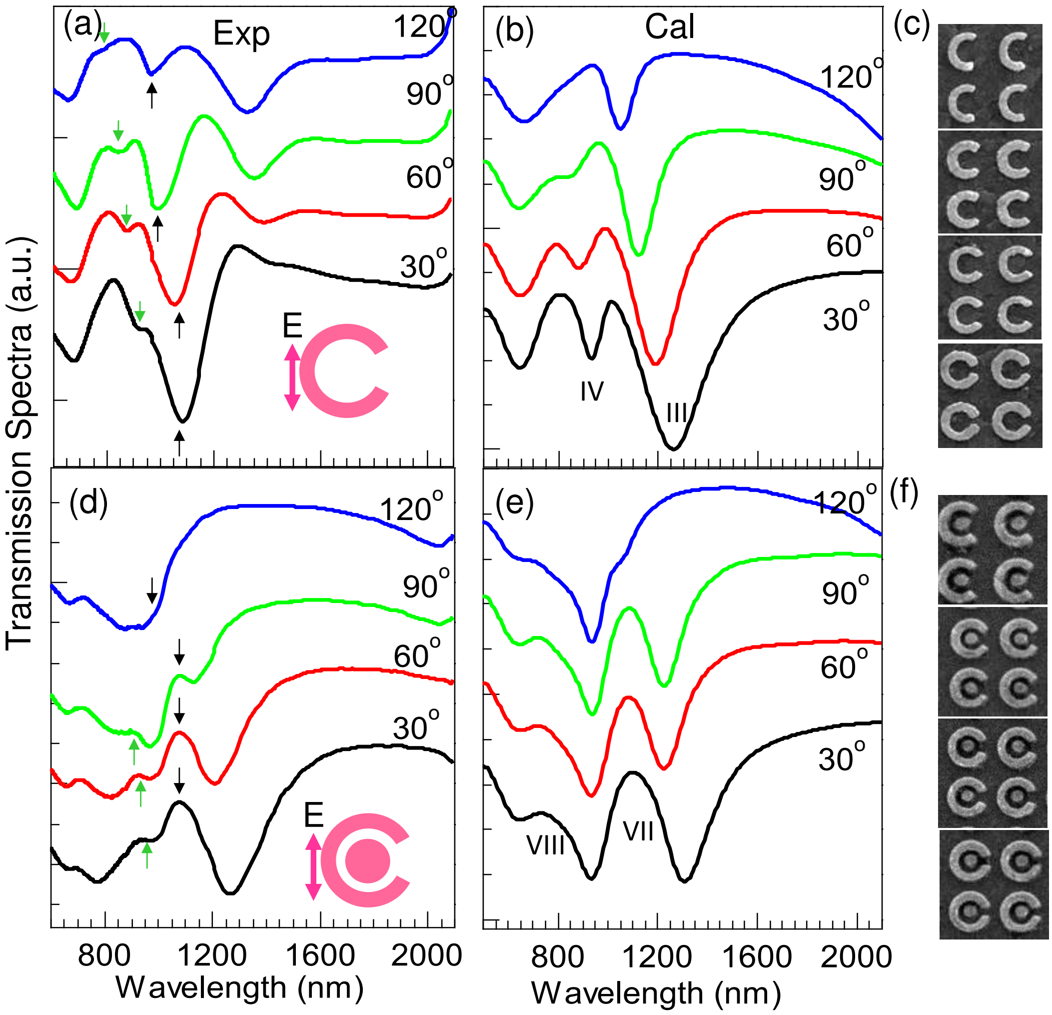

Figure 5-11 Tune Fano resonance via various split angles. (a) and (b) are experimental and simulation of SRR, respectively (c) the SEM image of SRR with split angle of 30º, 60º, 90º and 120º.(d) and (e) are experimental and simulation of SRR/disk, respectively.(f) the SEM image of SRR/disk with split angle of 30º, 60º, 90º and 120º. Here R_1=200 nm, R_2=110 nm, R_3=75 nm. The polarization is parallel to the split gap.

Here we just use the polarization parallel the spit gap to resolve the quadrupole and octupole magnetic mode. As shown in figure 5-11a, both the quadrupole (black arrows, figure5-11a) and octupole (green arrows, figure5-11a) magnetic mode of SRR are red blue shifted with the increasing split angle. The blue shift of quadrupole and octupole modes are approximately 150 and 100 nm respectively with the split angle increasing from 30º to 120º. The simulation results shown in figure 5-11b can agree with the experiment data very well. We attribute the resonance wavelength shift to the change of the capacitance between in the gap. In the U-shape SRR, it was well established that the magnetic resonance frequency is proportional to the $(LC)^{-1/2}$, in which L is the conductance of the SRR and C is the capacitance in the gap. The capacitance of SRR is inversely proportional to the gap distance d as the expression $C = \varepsilon_0 \varepsilon_{eff} {}^{wt}\!/_{d}$ indicated. In this case, increasing split angle will create a larger gap of SRR, rendering the magnetic resonance blue shift.

Besides the resonance wavelength shift, we also observed that the resonance minimum becomes weaker and weaker with increasing angle. The octupole magnetic mode almost disappeared with the split angle of 120º. We assume that the weaker resonance intensity was caused by the shorter length of SRR. As we discussed above, the magnetic modes arise from the partial circulating current along the SRR, the shorter length of SRR weaken the ability to sustain the circulating current along SRR especially for the higher order magnetic mode.

It was reasonable to observed the octupole mode almost is vanished while the quadrupole magnetic mode still present as shown in figure 5-11a. The blue shift of the magnetic modes in SRR will leads the corresponding blue shift of the magnetic modes based Fano resonance in SRR/disk cavity. As shown in figure 5-11d, both the quadrupole (black arrows, figure 5-11d) and octupole (green arrows, figure5-11d) magnetic mode based Fano resonance blue shift with the increasing spilt angle. In addition, the blue shift of the magnetic mode in SRR will affect the overlapping condition between the dark magnetic mode and the bright electric mode, which will tune the strength of Fano coupling. With increasing split angle, the resonance wavelength of the octupole magnetic mode is far and far away from the antibonding electric mode, so that we can observe the octupole magnetic mode Fano resonance becomes weaker and weaker and disappear at the angle of 120º. As a contrast, the overlapping between quadrupole magnetic mode and the antibonding mode becomes stronger with increasing angle, the Fano resonance becomes more and more pronounced. The quadrupole magnetic mode based Fano resonance (black arrows, figure 5-11d) is highly asymmetric at the angle of 90º, indicating the Fano coupling strength is strong. While, the quadrupole magnetic mode based Fano resonance at the angle of 120º is less pronounced because the intensity of the quadrupole magnetic mode itself is very weak at this angle as shown in the black arrows in figure 5-11a. In a word, the Fano resonance wavelength and the Fano strength could be tuned by changing the split angle.

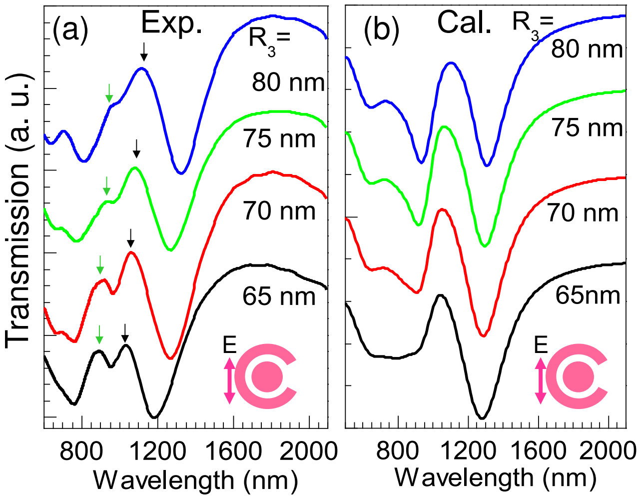

Figure 5- 12 Tune the Fano resonance via gap distance. (a) and (b) are experimental and calculated transmission with various radius (R_3) of disk. R_1=200 nm, R_2=110 nm, θ=30º.The polarization is parallel to the gap.

The Fano coupling also can be tuned by changing the distance between disk and SRR. We increase the radius of the disk from 65 to 80 nm so that the gap between disk and SRR decrease from 45 to 30 nm. The experimental and simulated transmission spectra are displayed in figure 5-12a and 12b respectively. It can be observed that the Fano resonance red shifts with decreasing gap distance, in addition, the Fano resonance becomes less and less pronounced with decreasing gap distance. It was demonstrated that the narrower gap between a disk and a ring will make the antibonding resonance blue shifts.[198] In our case, the blue shift of the antibonding mode will make the energy overlapping between magnetic mode and the antibonding mode become weaker, consequently the Fano resonance become less and less pronouncement. We can observer the peak becomes symmetric at the radius of 80 nm. Additionally, the narrower gap will render the peak of the antibonding mode sharper, further weaken the overlapping between the magnetic modes and the antibonding mode. In a word, the Fano resonance depth can be tuned by altering the gap distance between disk and SRR.

5.3.4 Sensing application of Fano resonance

It has been demonstrated that Fano resonance has huge potential in the sensing application because of its high sensitivity and figure of merit. To evaluate the sensing performance of the SRR/disk Fano resonance, we firstly conduct the refractive index sensing by measuring the transmission spectra. Glycerol, widely used in pharmaceutical formulations, whose refractive index is determined by the concentration. Glycerol dissolved in distilled water with the concentration of 10, 28, 44 and 64% gives the refractive index of 1.3448, 1.3676, 1.3897 and 1.4189 respectively. The refractive index is obtained from the handbook. The solution was dropped on the chip and a cover slip was applied to keep the solution on the substrate. The transmission was measure under the solution phase, subsequently, the chip was rinsed by distilled water heavily. The transmission was retaken to obtain an identical transmission spectrum to the chip before applying glycerol, making sure all the glycerol was removed for the next round measurement.

The measured transmission is shown in figure 5-13a, the SRR/disk cavity with the dimension R_1=200 nm, R_2=110 nm, R_3=70 nm and θ=30º is chosen. In addition to the glycerol solution, we also measured the transmission of bare SRR/disk and the water for comparison. It is clearly shown that the resonance red shifts with the increasing concentration. The arrows in figure 5-13a indicate the quadrupole mode based Fano resonance and the wavelength was extracted as shown in figure 5-13b. It is shown that the quadrupole magnetic mode based Fano resonance depends on the refractive index linearly. The sensitivity of the quadrupole mode based Fano is estimated to be ~279 nm/RIU. The figure of merit (FOM) is defined by $\delta\lambda / \lambda_{FWHM}$, here $\delta\lambda$ is the sensitivity, λ_{FWHM} is the full-width at half maximum of the corresponding mode peak. The FOM of the quadrupole magnetic mode based Fano is estimated to be 4.

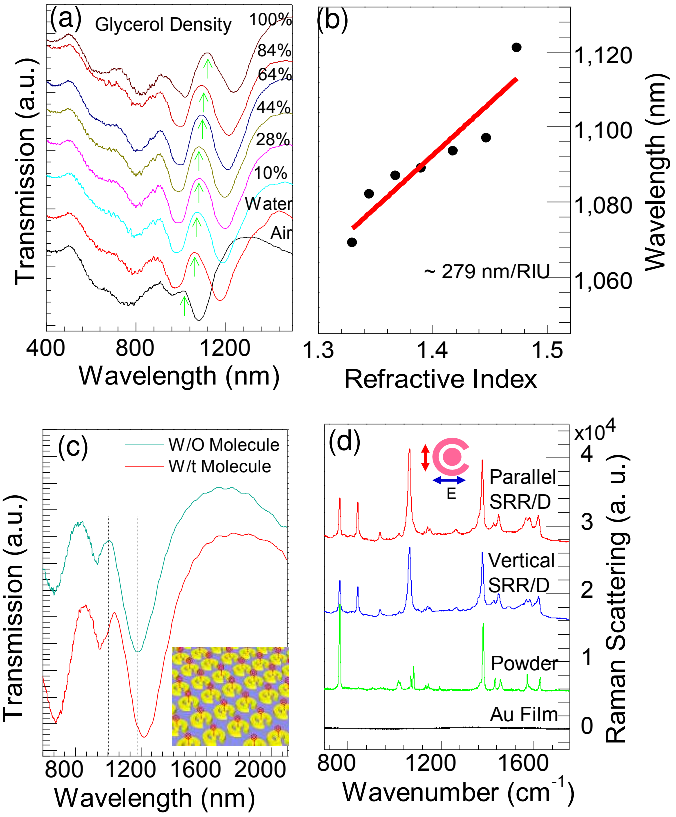

Figure 5- 13 Refractive index sensing and surface enhanced Raman scattering sensing. (a) transmission spectra of glycerol solution with various concentration. (b) extracted resonance under different refractive index. (c) Transmission of SRR/disk with and without 2-naphthalenethiol monolayer attached. (d) Raman spectra of 2-naphthalenethiol, inserted is the polarization configuration.

Previous study shows the double split-ring resonator fabricated with hole-mask method gives the sensitivity of 520 nm/RIU and the FOM of 2.9.[208] The highest EBL fabricates structure has the FOM of 5.7.[209] Our structure with the FOM of 4 is comparable with the highest FOM of the EBL fabricated structure. Furthermore, the sensitivity and the FOM can be optimized by changing the size, split angle and the interparticle distance.

In addition to the refractive index sensing, we also evaluate the surface enhanced Raman scattering of the SRR/disk cavity. We attached a monolayer of 2-naphthalenethiol molecules to the SRR, the transmission spectra with and without molecules attached are shown in figure 5-13c, a 32 nm red shift of the quadrupole mode magnetic mode based Fano resonance can be observed after the molecules attachment. The Raman scattering spectra of 2-naphthalenethiol powder and the monolayer on Au film and SRR/disk cavity are shown in figure 5-13d. A dramatic Raman enhancement is attainable in SRR/disk cavity in both polarizations. The enhancement factor is evaluated to be 1.2×10^6 for the parallel polarization.

5.4 Summary

Asymmetric Fano resonance is distinguished from symmetric Lorentz resonance in the lineshape. The study of the Fano resonance in a quantum system reveals that Fano resonance arises from the interaction between a discrete state and a continuum state. The lineshape of the Fano resonance can be describe by the Fano equation. Besides the Fano resonance in a quantum system, Fano resonance also can be realized in a plasmonic system. Plasmonics structure provides a platform to manipulate the oscillator in nanoscale. In plasmonic structure, the sub-radiant (dark) mode serves as a discrete state while the super-radiant (bright) mode serves as a continuum state, the weak coupling between the dark and bright mode generate a Fano resonance. The common strategy to generate a Fano resonance in a plasmonic structure is to break the symmetry to make the dark mode active. However, almost all the Fano resonance demonstrated in plasmonic structure arise from the purely electric interaction. The magnetic mode based Fano resonance in which the magnetic mode serves as a dark mode and the electric mode serves as a bright mode is of great interesting. The magnetic mode based Fano resonance can generate strong magnetism with optical excitation. In addition, the magnetic mode based Fano resonance has the potential to be a negative refractive index material with the negative permeability.

In this chapter, we demonstrated the high order magnetic mode based Fano resonance in a split ring resonator/disk cavity. The SRR is capable of sustaining a magnetic mode due to the partial circulating current along the SRR. The circulating current can be induced when the symmetry is broken with the polarization parallel to the split gap. Experiment and simulation show that both the quadrupole and octupole magnetic mode of SRR can be excited with the polarization parallel to the split gap, here the high order magnetic mode can serve as the dark mode and couple to a bright electric mode to generate a Fano resonance. The magnetic mode based Fano resonance can be tuned by changing the split angle. The Fano resonance wavelength blue shifts with the increasing split angle. We attribute the blue shift of the Fano resonance to decreasing capacitance in the gap. In addition, the blue shift of the magnetic mode changing the energy overlapping between the magnetic mode and the electric mode, which can be utilized to tune the Fano depth.

We also demonstrated the distance between the disk and the SRR can be used to tune the Fano resonance. Fano resonance will red shift and becomes weaker with decreasing distance. The refractive index sensing was conducted with SRR/disk cavity, the sensitivity and figure of merit is comparable with the other EBL fabricated structure.

Chapter 6 Perfect Absorber based on Ultrathin Phase Change Material $Ge_2Sb_2Te_5$ and the Coupling to Plasmonic Structure

6.1 Introduction

Sufficient absorption is essential for the photovoltaic cells, thermophotovoltaic cells and thermal emitters. Especially for the energy harvesting devices, it will benefit greatly if we can enhance the absorption of the active semiconductor layer. Over the past years, different kinds of absorbers have been demonstrated. Plasmonic and metamaterials structure based absorber have attracted tremendous attention because they are capable of achieving unity absorption. Intuitively, metals are mainly reflective in the visible to infrared frequency. However, plasmonics or metamaterials provides a platform to manipulate the permittivity and permeability of the structure at nanoscale. The well designed structure is possible to absorb the electric and magnetic components of the light simultaneously, resulting in a high absorption.

For plasmonics or metamaterials based perfect absorber, the structure is usually a sandwiched configuration, which consists of the metallic components at the top and bottom and a dielectric layer in the middle. The main purpose of the underneath metal is to reflect the light and exclude the transmission. The metal on the top are the plasmonics of metamaterials structures which couple to the underneath metal layer to confine the light in the middle dielectric layer to obtain high absorption. The antiparallel current on the top and bottom metallic components can generate a magnetic momentum and an electric mode is sustained on the plasmonic or metamaterials structures on the top. The plasmonics or metamaterials absorber can be treated as a continuous media with the complex permittivity $\varepsilon = \varepsilon_1 + i\varepsilon_2$ and complex permeability $\mu = \mu_1 + i\mu_2$. Theoretically unity absorption is possible if we tune the permittivity and permeability to make the impedance-matched to the free space.[210]

The plasmonics perfect absorber was demonstrated successfully in grating, disk and cubic nanoantenna.[211-213] The metamaterials based perfect absorber was obtained from the frequency from microwave, terahertz, infrared to visible.[210, 214, 215] Though plasmonics or metamaterials based absorber can achieve unity absorption, the performance is highly sensitive to the incidence angle and polarization. The high absorption under a critical condition reduces the potential of those devices in practical applications. In addition, the absorption band of the plasmonic and metamaterials absorber is very narrow. The plasmonic or metamaterials absorber is not convenient to integrate to the active semiconductor to enhance the absorption of the photovoltaic device. Absorber based on a thin film is another good candidate to enhance the absorption and it is easier to be hybridized to a solar cell device.

6.2 Thin film based absorber

Interference effect of a thin film with the thickness of the order of the incidence wavelength is widely observed in the nature such as the color of the oil on the water. The light reflected on the air/oil and oil/water interfaces interfere with each other to make light with a specific wavelength constructively reflected in a specific angle. Thin film interference is also widely used in the optical coating to realize the anti-reflection, high reflection and beam splitting. The common optics in laboratory such as the objectives, lenses and mirrors are almost associated with the thin film coating. In the conventional optical coating, a lossless dielectric with the minimum thickness of quarter wavelength is coated on a reflecting substrate as shown in figure 6-1a.

Both reflection and refraction processes undergo when the incidence light strike the air/dielectric interface, the reflective light r_0 has phase variation of π when the light pass from a low index medium to a high index medium. The phase accumulation before the refractive light hitting the dielectric/substrate is $\pi/2$ and another π phase variation will be added upon the reflection on the dielectric/substrate interface, subsequently another π/2 phase accumulation will be induced before it strikes the air/dielectric interface, so that the partial wave r_1 has no different phase compared with the incidence light. In the same manner as r_1, another partial waves r_2, r_3,....r_n has the same phase as the incidence light. The phase diagram of the conventional optical coating is shown in figure 6-1b, r_0 interfere with other partial waves r_1, r_2, r_3,....r_n destructively and a specific wavelength light cannot be reflected by the system.

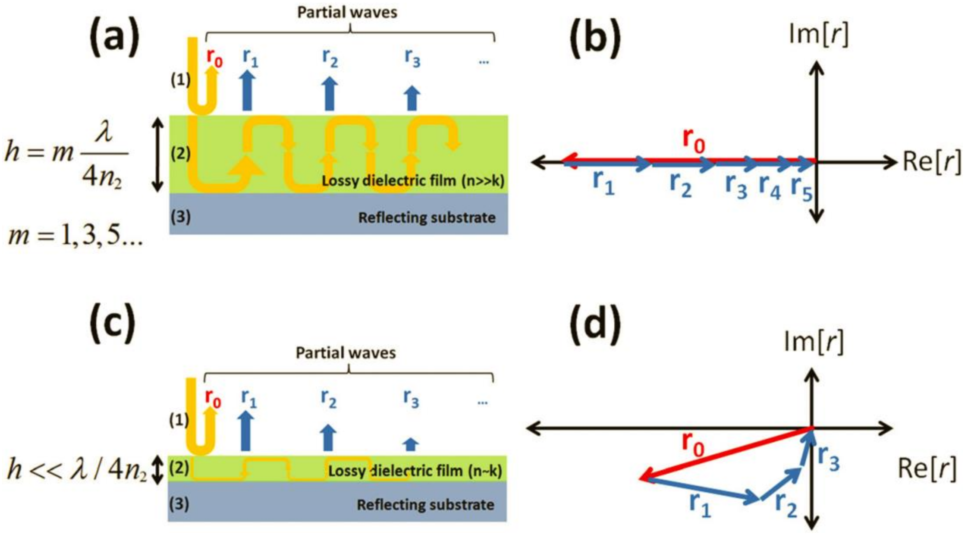

Figure 6-1 Interference effect of thin film. (a) schematic of the conventional optical coating with a lossless dielectric. (b) phase diagram in the configuration (a). (c) schematic of the interference of a ultrathin lossy material. (d) phase diagram in the configuration (c). Figures are adapted from Kats, M. A.[216]

The phase accumulation during the propagation of the light in the dielectric depends on the thickness, refractive index of the dielectric and the incidence angle, the minimum thickness required to obtain a destructive interference effect should be quarter wavelength $\lambda/4n$ (n is the refractive index of dielectric). It was believed that a lossy material is not comparable with the interference effect because light will dissipate very rapidly inside the absorbing material. However, later it was demonstrated that an absorbing layer was capable of sustaining the interference effect once make the layer very thin as shown in figure 6-1c.[217] Based on the Fresnel reflection coefficient $r_{12} = (\tilde{n}_1 - \tilde{n}_2)/(\tilde{n}_1 + \tilde{n}_2)$, where $\tilde{n} = n + ik$ is the complex refractive index and the light encounters medium 2 from medium 1, the reflection on a general interface ($n>>k$), the phase variation is π or 0, while the phase variation is no longer π or 0 when one side is a lossy layer (with n~k). Consequently, interference condition can be met even though the thickness is less than a quarter wavelength. Because the lossy film is very thin, the attenuation of the light inside the dielectric is limited and the intensity of the partial waves r_1,r_2, $r_3,....r_n$ are still efficient to interfere with r_0 destructively. Figure 6-1d shows the nontrivial phase diagram when an absorbing material is involved. The light that cannot be reflected by the system is absorbed because no transmission is allowed due to the presence of the reflecting substrate underneath, suggesting that thin film coating can serve as a good absorber.

Previously, a Fabry-Pérot (FP) cavity was widely used to enhance the performance of the optoelectronic and photonic devices by placing the device in the middle of the cavity. The field enhancement inside the cavity can be utilized to manipulate the device performance.[218, 219] One drawback of the FP cavity is that the absorption is highly dependent on the incidence angle. In addition, the thicker multiple layer structure makes it not suitable for the energy harvesting cells. As we know, there is a trade-off between the thickness of the semiconductor layer and the light absorption. A thinner layer is preferred in order to achieve excellent carrier generation, injection and extraction. However, a thinner layer will result in insufficient light absorption. In this case, an ultrathin layer material with high absorption is desired to be hybridized to the energy harvesting cells. As we discussed above, an ultrathin lossy material can be applied to accomplish the interference effect and consequently achieve a high absorption. It has been demonstrated a thin iron oxide (α-Fe_2O_3) with the thickness of 26 nm was applied on a metallic substrate to enhance the efficiency of the water splitting.[220] A vanadium dioxide layer was combined with a sapphire substrate to realize a perfect absorber in the far infrared range by controlling the phase or vanadium dioxide.[216] In this thesis, we demonstrate a perfect absorber with a unity absorption in the visible-near IR range by utilizing a phase change material $Ge_2Sb_2Te_5$. The absorption band can be engineered by changing the thickness of the phase change material. The absorber can obtain an efficient absorption in a broad incidence angle.

In addition, the performance of the absorber can be tuned by inducing a phase transition of $Ge_2Sb_2Te_5$.

Apart from a homogeneous film on the metal reflector, we have also fabricated a plasmonic array on the GST film. The combination of the plasmonic structure and the thin film gives a broader absorption band. In this configuration, GST thin film is sandwiched between the plasmonic array and the underneath metal film. The coupling of the plasmonic array and the metal film will result in broader absorption band compared to the sole thin film absorber.

6.3 Visible-near IR perfect absorber based on $Ge_2Sb_2Te_5$ thin film

6.3.1 Properties of $Ge_2Sb_2Te_5$ thin film

Germanium-antimony-tellurium (GeSbTe) system is typical phase change materials which are widely used in rewritable optical data storage and phase change memory. The nanosecond recrystallization time and the large change of the optical and electric properties during phase transition make it an excellent data storage material. In the application of optical data storage, the whole chip is initialed to a crystalline state with a low intensity focused laser radiation, the data is recorded on the amorphous spots which are produced by melting the material with high power laser and then cool down rapidly. The data can be read by scanning the chip with a laser and measure the reflectivity. Erasing is completed by converting those amorphous spots back to the crystalline state with a low power laser. For the application of phase change memory, the phase transition is induced by applying an electric pulse and the resistivity difference of amorphous and crystalline state are utilized to set the “0” and “1” state in the logic.

Several alloys of GeSbTe system were proven to be an effective data storage material such as $GeTe\text{-}Sb_2Te_3$, $Ge_{15}Sb_{85}$ and $Sb_{70}Te_{30}$.[221] Three factors should be considered to judge whether it is suitable for the data storage, which are the melting point, the recrystallization speed and the activation energy. For instance, alloy Sb_2Te_3 has a fast recrystallization speed but it is not stable because of the low activation energy, on the contrary, a stable alloy with high activation energy usually has a slow recrystallization speed. $Ge_2Sb_2Te_5$ has appropriate recrystallization speed and stability which makes it suitable for the data storage application. Over the past years, $Ge_2Sb_2Te_5$ has received considerable research interests. $Ge_2Sb_2Te_5$ has three phases including one amorphous phase and two crystalline phases. $Ge_2Sb_2Te_5$ will transit from amorphous to the rock salt structure (*Fm3m*) near the temperature of 140℃, it will further come to the hexagonal structure when increasing the temperature to 370℃. The crystalline state will return to amorphous state if the alloy is melt and cool down rapidly.

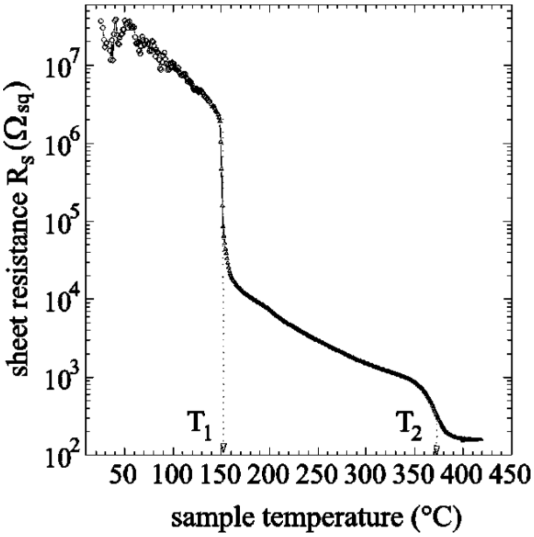

Figure 6-2 Resistance of $Ge_2Sb_2Te_5$ at different phase induced by a temperature variation. Picture adapted from Friedrich, I.[222]

It was reported that the resistivity will drop dramatically during the phase transition at the temperature near T_1 and T_2 as shown in the figure 6-2, confirming the phase transition did occur. In our experiment, the $Ge_2Sb_2Te_5$ thin film is deposited with a magnetron sputter. The thickness can be controlled precisely by controlling the deposition time and rate. The as-deposited thin film is in amorphous phase, and the phase transition is induced with a rapid annealing process. The chip is annealed at 170 ℃ for 10 mins to make the transition from amorphous to rock salt structure, and further annealing at 380℃ for 10 mins make it transit to the hexagonal structure.

The XRD and Raman are measured to confirm the phase transition as shown in figure 6-3. Figure 6-3a, 3b and 3c show the XRD of the as-deposited, after 170℃ annealing and after 380℃annealing respectively. No XRD can be detected at the room temperature, suggesting that the as-deposited film is amorphous. The XRD peaks confirms that the film is in rock salt structure after 170℃ annealing and hexagonal structure after 380℃ annealing.[222] Furthermore, we measure the Raman signal of the GST film at different phases as shown in figure 6-3d. The Raman measurement was conducted on the Horiba JY T64000 under the 532 nm excitation laser with the power of 0.24 mW, we use the low power laser to guarantee that the phase transition cannot be induced by the heating from the laser radiation.

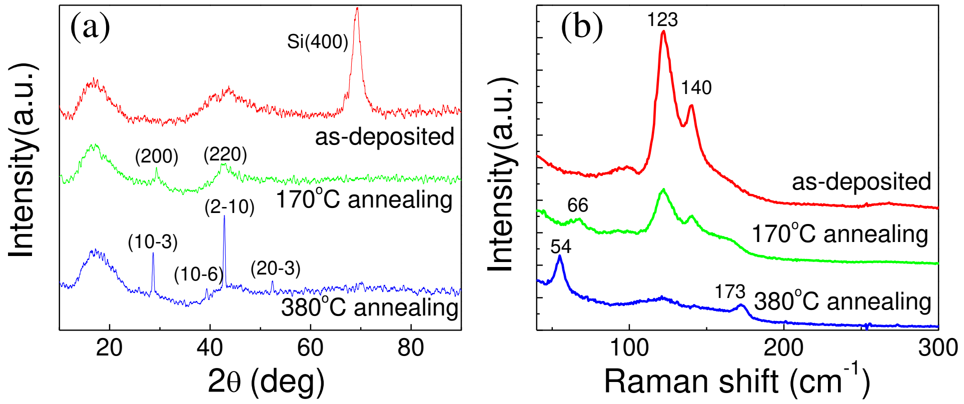

Figure 6-3 Phase transition of $Ge_2Sb_2Te_5$ induced by heating. (a) XRD of the thin film under different phases. (b) Raman of the $Ge_2Sb_2Te_5$ under different phases.

Two vibrational modes with the Raman shift of 123 and 140 cm^{-1} at the room temperature were also observed in the sputtering GST film by other researcher, they assigned the 123 cm^{-1} shift to A_1 mode of $GeTe_4$ tetrahedral and shift of 140 cm^{-1} is attributed to A_1 mode of disordered helical Te chains.[223] Based on the first principle calculation, the shift of 54 cm^{-1} shift is the E_g mode of the hexagonal structure and the 173 cm^{-1} shift is the A_{1g} mode of the hexagonal structure, suggesting the GST is in the hexagonal structure after 380℃ annealing. In a word, the GST thin film was deposited by a sputtering system and the phase transition can be triggered by heating it. The XRD and Raman measurement confirm that the transition from amorphous to rock salt and further to hexagonal structure does undergo upon heating at 170 and 380℃ respectively.

6.3.2 Perfect absorption based on $Ge_2Sb_2Te_5$ thin film

Inspired by the interference effect in an ultrathin lossy material, we intend to construct a perfect absorber with the absorption band in visible-near IR range. Based on the measured dielectric constant, the imaginary part $\varepsilon_2(w)$ is about 5-15 in the visible to near IR range,[224] which makes it a suitable absorbing material to construct a ultrathin film based absorber. Previously, simulation shows that the GST film sandwiched between the metal film and plasmonic structure can result in a broad absorption band in visible range, in which the GST serves as a spacer layer.[225] A novel display was also demonstrated by a GST film coating, in which the GST was sandwiched by the transparent electrodes indium tin oxide (ITO). The interference effect is responsible for the color difference of the chip with different GST and ITO thickness.[226]

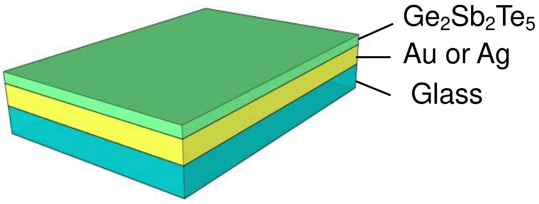

Figure 6-4 Schematic of the GST based perfect absorber.

Here, we construct the perfect absorber simply by depositing a GST thin film on a reflecting substrate as shown in figure 6-4. 150 nm Au or Ag is deposited on the glass substrate directly by the thermal evaporation. Subsequently, the GST layer is grown by the magnetron sputtering system, the deposition rate is about 7 nm/s by applying the RF source with the power of 50 Watts. The thickness of GST is varied from 10 to 70 nm by controlling the deposition time and the as-deposited GST is in amorphous phase. Because 150 nm metal layer is sufficient to block the light in visible-near IR range and there is no transmission here, thus we can estimate the absorption of the structure by measuring the reflection. The absolute reflection can be measured in our UV/Vis/NIR spectrometer (Lambda 950, PerkinElmer) under the two beam configuration.

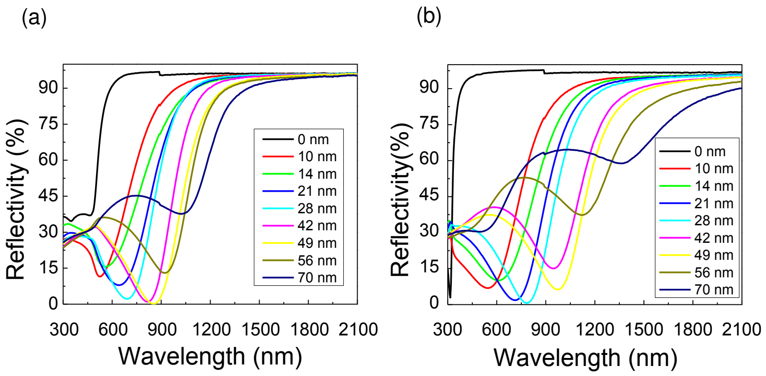

Figure 6-5 Reflectivity of the GST thin film absorber. (a) reflectivity of the absorber with various GST thickness on Au substrate. (b) reflectivity of the absorber with various GST thickness on Ag substrate.

Figure 6-5 shows the absolute reflectivity of the absorber based on Au and Ag reflecting substrates with various GST thicknesses. Figure 6-5a shows the reflectivity as the GST thickness is varied, using Au as the reflecting substrate. The black curve is the intrinsic behavior of the Au film with the thickness of 150 nm. It is clearly seen that 95% of the light will be reflected by the Au film at the wavelength longer than 600 nm. The reflectivity drops dramatically after adding 10 nm GST on the top and its minimum is 11.5% at the wavelength of 524 nm. The reflection minimum red shifts with the increasing GST thickness. Typically when the thickness is 28, 42 and 49 nm, the attainable minimum reflectivity is about 2.2%, 1.0% and 0.2% at the wavelength of 692, 816 and 853 nm respectively.

From the GST thickness we can see that the thickness required to achieve high absorption is less than the quarter wavelength. For instance, when the GST is 28 nm thick, $h\sim\lambda/11n$, refractive index n of GST film is about 2.2 at 692 nm.[227] Considering that the light cannot be reflected is absorbed, we can achieve nearly unity absorption. For instance, for the 49 nm GST, 5% light is absorbed by the Au film the rest 95% is absorbed by the GST thin film. The fact that most of the light is absorbed by the ultrathin semiconductor layer highlights the huge potential of the thin film absorber in the application of energy harvesting, which can overcome the trade-off between the thickness of semiconductor layer and the light absorption efficiency.

Figure 6-5 also shows that the absorption band depends on the GST thickness, which makes it possible for us to select the absorption wavelength at will by controlling the GST thickness. In addition, the width of the absorption band (the width of the reflectivity minimum) is quite broad. For example, in the 49 nm GST case, the width of the absorption band with the absorption larger than 90% is about 200 nm, from 736 to 936 nm.

Figure 6-5b shows the reflectivity at various GST thickness using Ag as the substrate, the performance is similar with those of the Au substrate and an unity absorption is achieved. The absorption is as high as 99.3% at the wavelength of 784 nm when a 28 nm GST is deposited on Ag. One advantage of the Ag substrate over Au substrate is that the intrinsic absorption of Ag is much lower in the visible range because its interband transition is located at UV range as shown in the black line in figure 6-5b. The lower intrinsic absorption in visible range guarantees that most of the light in visible range is absorbed by the GST layer instead of the metallic substrate.

We attribute the perfect absorption to the interference effect inside the absorbing GST layer. Because the metal in the visible-near IR is not a perfect electric conductor and has a complex dielectric constant, the reflection in the GST/metal interface is nontrivial (the phase variation is not 0 or π). The nontrivial reflection on the air/GST and GST/metal interfaces makes the interference effect feasible even when the GST thickness is much less than the quarter wavelength.

6.3.3 Incidence angle dependent absorption

As we know, the absorption Fabry-Pérot (FP) cavity is sensitive to the incidence angle. Because the dielectric layer in the FP cavity is very thick, the minor change of the incidence angle will lead to a considerable difference of the optical path inside the dielectric and the phase accumulation is quite different, consequently the resonant wavelength is highly sensitive to the incidence angle. However, a stable absorption performance within a broad incidence angle is desired to capture more light from different incidence angles. In the ultrathin film based Fano resonance, we expect that the phase accumulation difference due to the change of incidence angle is not that significant.

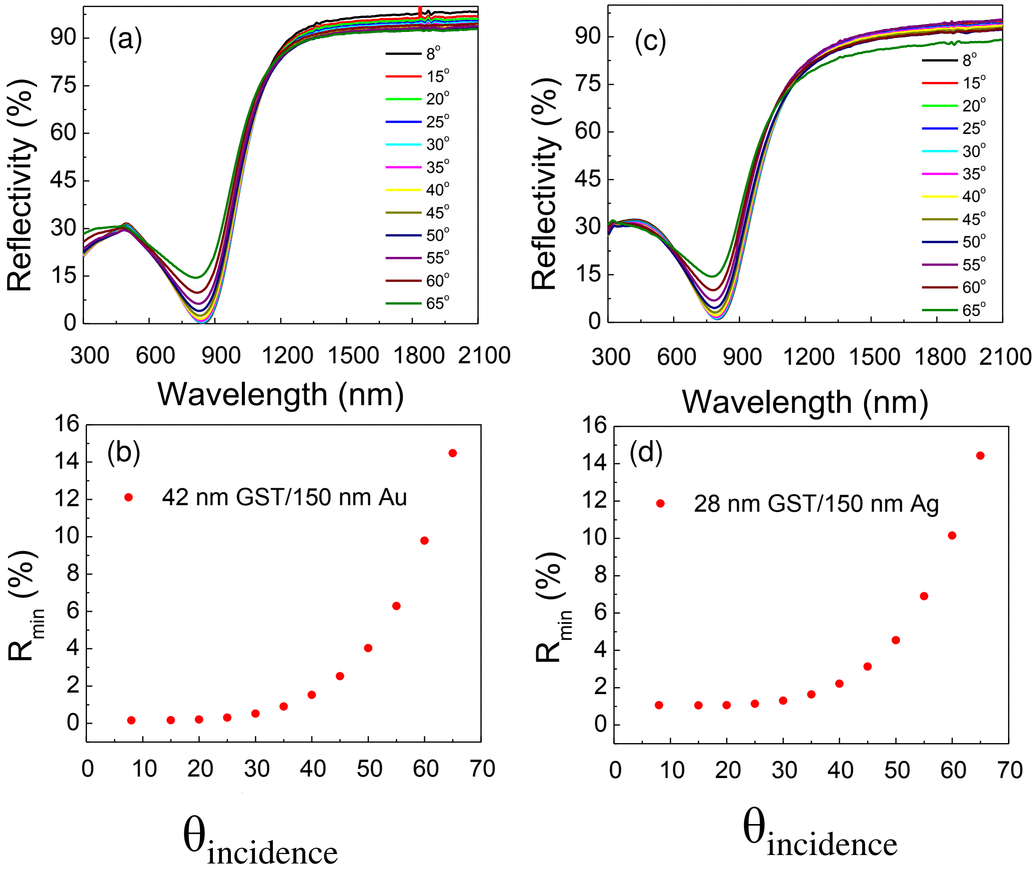

Figure 6-6 Incidence angle dependent reflectivity. (a) Reflectivity of 42 nm GST on 150 nm Au with different incidence angle. (b) Extracted reflectivity minimum in each incidence angle corresponding to (a). (c) Reflectivity of 28 nm GST on 150 nm Ag with different incidence angle. (d) Extracted reflectivity minimum in each incidence angle corresponding to (c).

In the experiment, we examine the incidence angle dependent absorption by measuring the absolute reflectivity by varying the incidence angle from 8 to 65° and the result is shown in figure 6-6. Figure 6-6a shows the angle dependent reflectivity of 42 nm GST on 150 nm Au from 8° to 65°. The reflectivity minimum of each incidence angle was extracted and shown in Figure 6-6b. The reflectivity minimum almost remains unchanged with the incidence angle below 30º and reflectivity increases when the angle is larger than 30º. However, the reflectivity minimum remains in relatively low value within the range from 0-55º. Figure 6-6c and 6d plot the reflectivity and the minimum reflectivity versus incidence angle, respectively, for the case of 28 nm GST on 150 nm Ag. The performance is similar to the case where Au was used as the reflector. The GST thin film based absorber can perform well within a broad incidence angle, which is a great advantage over the conventional FP resonator and exhibits advantages for solar harvesting applications.

6.3.4 Tune the absorption with phase transition of $Ge_2Sb_2Te_5$

It was reported that the phase transition of GST was utilized to construct an optical switch.[162] The large difference of the optical property of GST at amorphous and crystalline phases also can be used to tune the performance of the thin film perfect absorber. The reflectivity of GST in rock salt structure after 10 mins annealing at 170℃ was shown in figure 6-7a, for comparison we put the reflectivity of the GST in amorphous in figure 6-7b (which is the same as figure 6-5a).

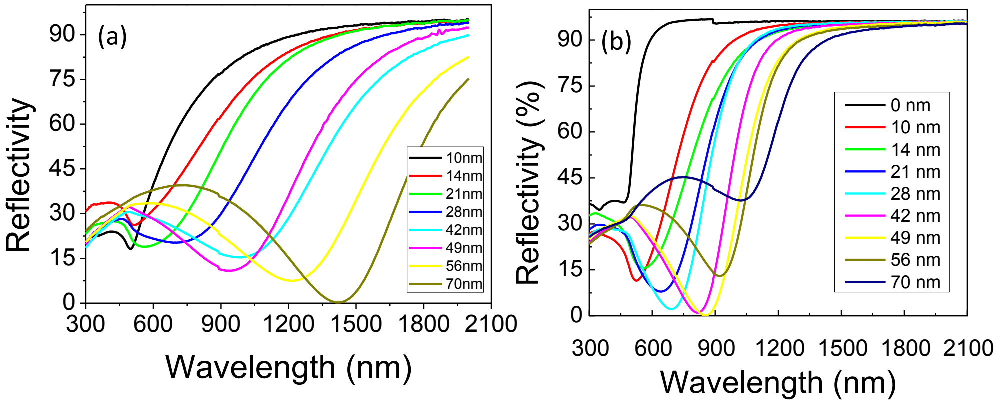

Figure 6-7 Reflectivity of thin film absorber under crystalline and amorphous GST. (a) reflectivity of crystalline (rock salt structure) GST with different thickness. (b) reflectivity of amorphous (as-deposited) GST with different thickness.

The samples used in figure 6-7a is obtained by annealing the amorphous sample used in figure 6-7b. The reflectivity of GST with the same thickness under amorphous and crystalline is quite different. For example, the 70 nm GST in amorphous phase has very a poor absorption, while the 70 nm GST in crystalline phase has unity absorption at the wavelength of 1400 nm. The 49 nm GST in amorphous phase has unity absorption at the wavelength of 853 nm. However, the absorption of 49 nm crystalline GST is reduced significantly. In addition, the reflectivity minimum of crystalline GST red shifts compared with the amorphous GST, and the absorption band in crystalline phase is much broader. For better analysis, we plot the reflectivity of GST with the same thickness but different phases individually as shown in figure 6-8. We compare the reflectivity of the amorphous and crystalline GST at the thickness of 70, 56, 49 and 42 nm.

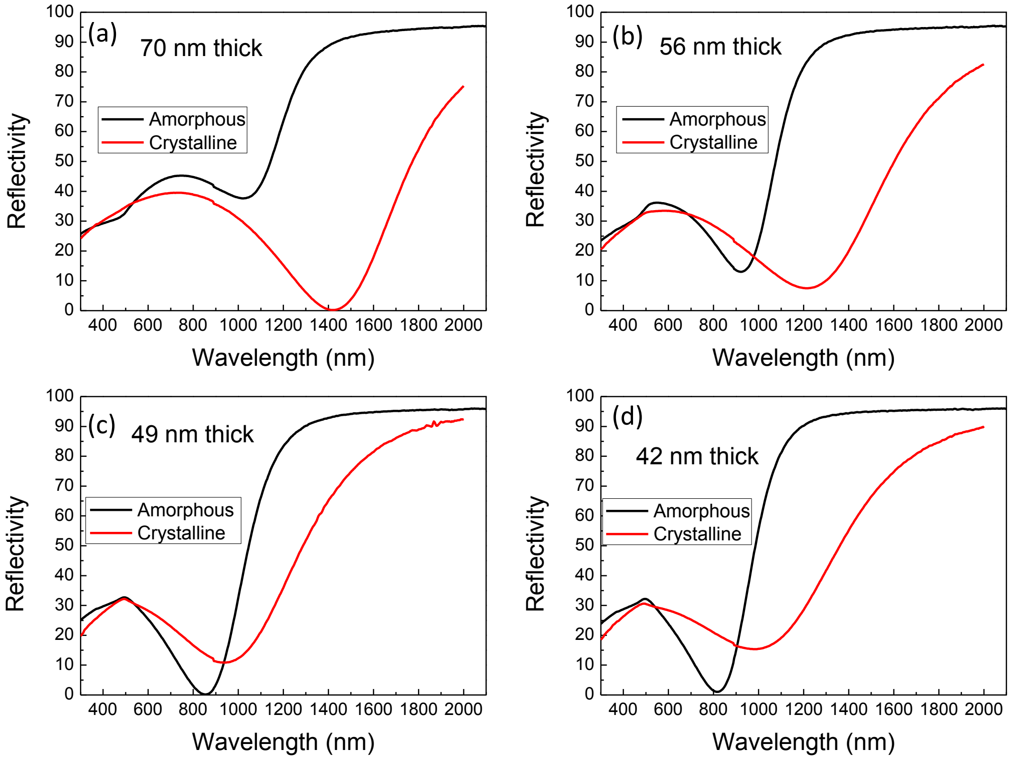

Figure 6-8 Reflectivity of amorphous and crystalline GST. (a)-(d) are the GST with the thickness of 70, 56, 49 and 42 nm respectively.

The different reflectivity of GST under amorphous and crystalline phase suggests that the absorption behavior can be engineered by controlling the phase transition. The large reflectivity difference under different makes the GST thin film based absorber has huge potential in the optical switch application. Figure 6-9 shows the plot of the contrast ratio of the 70, 56, 49 and 42 nm GST. The contrast ratio is defined by the equation $contrast = (R_{crystalline} - R_{amorphous}) / R_{amorphous}$ or $(R_{amorphous} - R_{crystalline}) / R_{crystalline}$ based on which phase has the lower reflectivity. The contrast ratio is as large as 400 for 70 nm GST. The high contrast ratio arise from the near zero reflectivity at the specific wavelength. It was reported that the optical switch constructed by combining GST and metamaterials has the optical ratio of 4,[162] the contrast ratio of our perfect absorber is much higher. In addition, the wavelength band with high contrast ratio can be tuned by changing the thickness, highlighting the considerable potential in the tunable optical switch application. For instance, the absorber with the GST thickness of 70, 56, 49 and 42 nm has high contrast ratio near the wavelength of 1400, 1200, 850 and 820 nm respectively as shown in figure 6-9. In addition, the high optical contrast can be used in rewritable disk application, the performance will be better with higher contrast than the pure GST film.

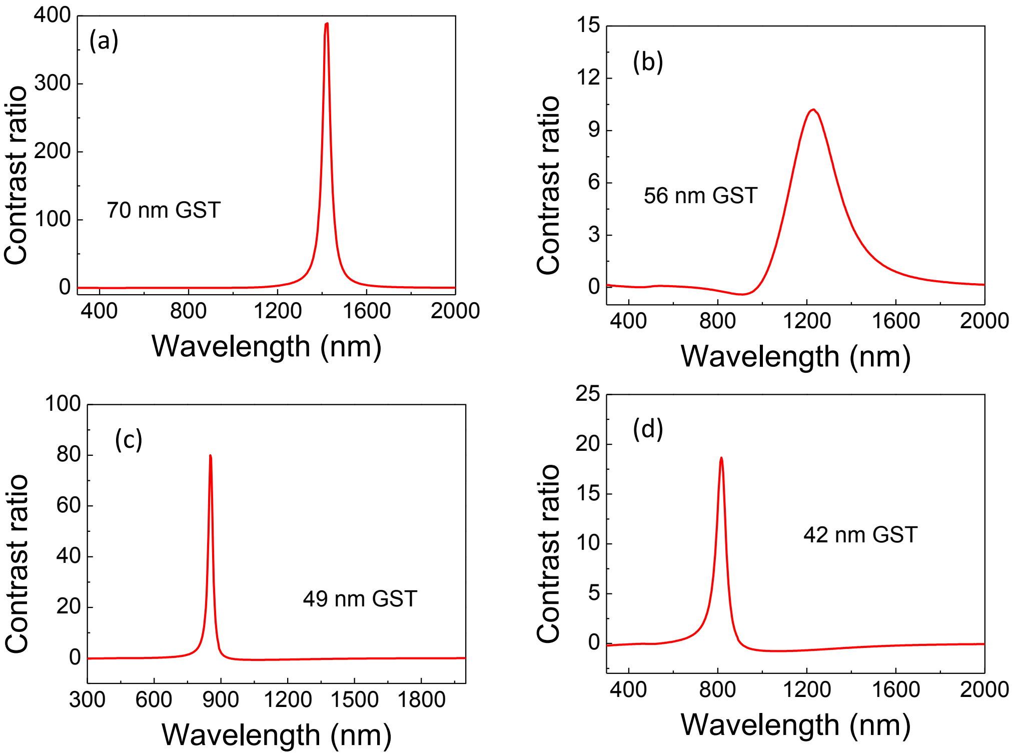

Figure 6-9 Contrast ratio of GST with the thickness of 70 nm (a) , 56 nm (b), 49 nm GST (b) and 42 nm (d).

6.4 Integration of $Ge_2Sb_2Te_5$ thin film absorber to plasmonic structure

It is relevant to explore whether the absorption band can be tuned to be even broader. Plasmonics have attracted a lot of attention due to its application in sensing, lasing and absorber [228-232]. The simulation shows that it is possible to accomplish a broadband absorber by combining plasmonic structure with the GST thin film absorber [15]. Experimentally, we fabricate a nano square array on the top of GST with EBL as shown in the cartoon in Figure 6-10(a), the SEM image is also shown in Figure 6-10 (c), the width of the square is 140 nm and its thickness is 30 nm, the GST thickness here is 24 nm. Because the area of EBL pattern (50×50 μm^2) is too small to be compatible with the measurement of Lambda 950, we firstly measure the relative reflectivity referring to the bare Au film using a microspectrophotometer (Craic 20) and then multiply the absolute reflectivity of the bare Au film to obtain the absolute reflectivity of the absorber. As shown in Figure 6-10 (d), the absorption band is broader after adding the nano square array (green line) compared with the GST/Au absorber (red line). The absorbance is enhanced significantly in visible range which is consistent with the simulation in reference [225]. As discussed in the reference [225], the broader band absorption is attributed to the coupling of the square and the underlying Au film, which can concentrate the electromagnetic field further between the gaps. Unfortunately, the reflectivity minimum increases after adding the square array. We suspect that this may be due to the scattering effect of the square arrays due to the surface roughness. As such we coat a PMMA layer with a thickness of ~ 20 nm to smoothen the absorber as shown in the cartoon in Figure 6-10 (c). After smoothing the surface, the performance is enhanced further as shown in the blue line in Figure 6-10 (d), the absorption band become broader and can cover the whole visible range.

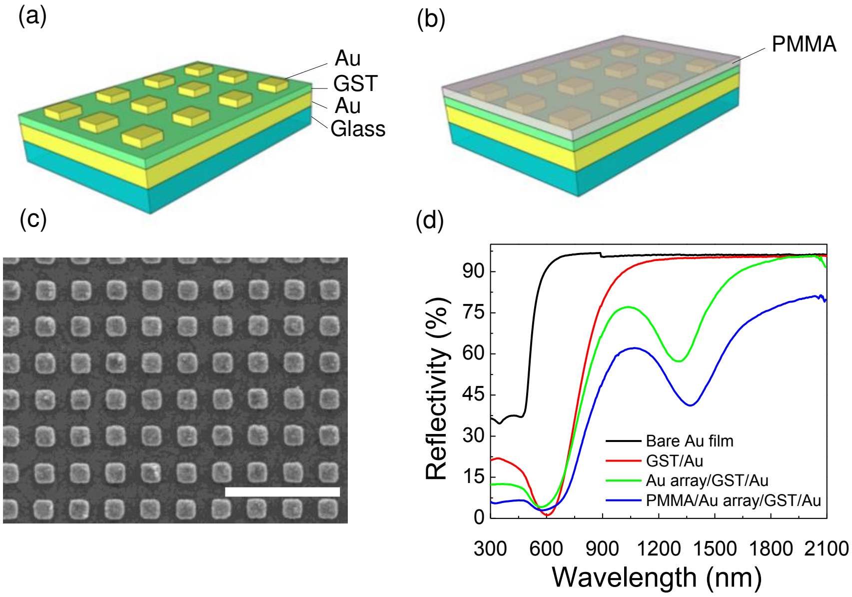

Figure 6-10 (a) Schematic of square array on GST. (b) A PMMA layer is coated on the top to smoother the surface. (c) SEM image of the square array, the scale bar is 1 μm. (d) Reflectivity of absorber with different configurations.

6.5 Summary

The dielectric thickness required to obtain interference effect in conventional optical coating is quarter wavelength. However, it has been demonstrated that interference effect also occurs on an ultrathin absorbing layer. The fact that the reflection phase variation is no longer 0 or π on the interface of lossy material is responsible for the interference effect inside the materials with the thickness less than quarter wavelength. The interference effect in an ultrathin film can be utilized to enhance the light absorption of a thin layer, which will be essential in the energy harvesting devices. The efficient absorption in a thin semiconductor layer can overcome the trade-off between the light absorption and material thickness. Herein, we have demonstrated a perfect absorber with unity absorption in near infrared range by simply coating a GST thin layer on the metallic substrate. The absorption band can be tuned by changing the GST thickness. The performance of the absorber is not sensitive to the incidence angle, the absorption is pronounced even when the incidence angle is as large as 50º.

Importantly, the absorption band can be tuned by inducing the phase transition of GST. The attainable optical contrast ratio is as high as 400, which is the highest among the literature reports. The large difference in reflectivity under different GST phase makes it promising in the optical switch application and rewritable disk. In addition, by combining this GST thin film absorber with the plasmonics array, we can make the absorption band broader and the absorbance is remarkable in the whole visible range.

Chapter 7 Conclusions and Future work

7.1 Conclusions

In this dissertation, by utilizing split ring resonators as a basic metamaterials and plasmonics component, we explore the fabrication, properties characterization and the application of the flexible and tunable metamaterials. Moreover, the magnetic mode based Fano resonance inside the split ring resonators is investigated. At last, a phase change thin film based perfect absorber is constructed and the coupling to a plasmonic structure is studied.

We successfully integrated the metamaterials onto a polymer to generate a flexible metamaterials. We invented a nickel sacrificial layer assisted transfer method to embed the nano structure onto PDMS. The deflection effect is absent in our method and the whole structure array can be transferred from a rigid substrate to PDMS with 100% yield. Both the morphology and the optical response can be maintained after the transfer process. The application of metaflex in chemical sensing is demonstrated, it shows that it is capable of sensing a monolayer molecules. More importantly, a convenient SERS substrate is invented with the flexible metamaterials. We successfully detected the molecules residing on Au film by covering the PDMS-meta on the Au film top and then measure the Raman signal. The PDMS-meta SERS substrate can avoid the direct contact between the probed substance and the substrate. We experimentally and theoretically show that the coupling between the metamaterials and the underneath metal film is responsible for the field enhancement, suggesting the PDMS metamaterials can serve as a representative model to investigate the interaction between nano structure and the metal film.

SRR metamaterials are integrated to a phase change VO_2 film to realize a tunable metamaterials. Firstly, we fabricated a high quality VO_2 thin film by controlling the temperature and the oxygen ratio. The resistance and the Raman measurement during the phase transition show the quality of VO_2 meet our requirement. We demonstrate that both the electric and magnetic resonance wavelength can be tuned by inducing the phase transition of VO_2. The magnetic mode red shifts while the electric mode blue shifts during the transition from the semiconductor phase to the metallic phase. The resonance wavelength shift is reversible and it can be controlled in real time. Furthermore, a tunable SERS device is demonstrated by utilizing the tunable metamaterials as the SERS substrate. We show that the SERS intensity can be engineered by controlling the electric resonance wavelength, suggesting that the tunable metamaterials response possesses considerable potential in sensing application.

Magnetic mode based Fano resonance is revealed inside the split ring resonator/disk (SRR/D) resonators. SRR/D array with high uniformity is fabricated with electron beam lithography. Polarization dependent transmission spectra are resolved in disk, SRR and SRR/D structure respectively. The observed asymmetric spectra are attributed to the Fano resonance. The electromagnetic field simulation reveals that the Fano resonance arises from the interaction between high order magnetic modes and electric dipole. The Fano resonance can be tuned by changing the size and shape of the cavity. The Fano resonance red shifts with the increasing of split angle. In addition, the Fano resonance red shifts and becomes weaker when the gap between disk and ring decreases. At last, we demonstrate that the magnetic based Fano resonance is sensitive to the refractive index change and a FOM of 4 is attainable.

GST thin film based perfect absorber with unity absorption is constructed. We demonstrated that the interference effect can be sustained inside the ultrathin lossy phase change film. The absorption can be as high as unity at the resonance wavelength and the absorption band can be tuned by changing the GST film thickness. Moreover, the absorber performance is not sensitive to the incidence angle and the absorption is pronounced even when the angle is as large as 55º. The reflectivity can be altered by inducing the phase transition of GST, the difference reflectivity at amorphous and crystalline phase result in a contrast ratio as high as 400. The high contrast ratio highlights the potential in the application of optical switch and rewritable data storage. Furthermore, we show that the combination of thin film absorber with plasmonic structure can make the absorption band broader.

7.2 Future work

(1) Magnetic modes enhanced emission

Both SRR and SRR/D cavity we discussed in this thesis have strong magnetic response. It was well established that the resonance of electric dipole can give a localization of the field and consequently modify the emission of the quantum emitters. However, the resonance of the magnetic mode also can modify the emission. Until now, the research on the magnetic modes resonance enhanced emission is not sufficient and the mechanism is still not well understood.

For specificity, it is of great interest to investigate the competition between electric mode and magnetic mode enhanced emission when both modes are presented. We are also curious about that whether it is possible for both electric and magnetic modes enhanced the emission simultaneously. Those enhancements probably help to engineer the loss of the plasmonic structure. What's more, the theoretical study shows that the resonant magnetic mode can enhance the magnetic dipole emitter.[233] Magnetic dipole transition is usually much weaker than electric dipole transition, so that it is nontrivial to observe magnetic dipole emission. It is interesting to experimentally investigate how the magnetic mode modifies the emission of a magnetic dipole emitter.

(2) Ultraviolet plasmonics

Until now, most of the plasmonic structures perform at visible-near IR range and the common plasmonics materials are gold and silver. It is challenging to extend the operation range to ultraviolet because Au and Ag cannot access to UV range. Limited by the bulk plasmon frequency, dielectric constant and the interband transition, Au and Ag structures perform very poor at the wavelength shorter than 550 nm and 400 nm respectively. However, it is of great importance to explore the plasmonics structures with the resonance frequency at UV range. UV plasmonic has increasing interest application in biological detection, recognization and analysis. For example, UV SERS possesses great potential in the biological molecule detection because those molecules have higher absorption of UV light and can attain resonant Raman.

Al is a promising UV plasmonic material with the bulk plasmon frequency of 13 eV. The performance of Al nanostructure has been examined experimentally and theoretically.[234, 235] One drawback of Al is that it oxides very rapidly and the Al_2O_3 layer will reduce the performance of Al structure, introducing difficulties for the realization of a stable device. It was theoretically predicted that other materials such as gallium (Ga), indium (In), titanium (Ti), chromium (Cr) palladium (Pd), copper (Cu), platinum (Pt) have potential as the candidate of UV plasmonic materials.[236]

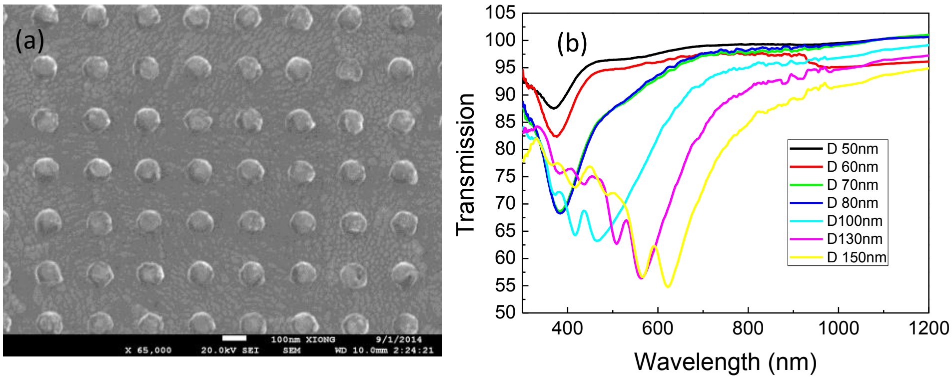

Figure 7- 1 (a) SEM image of In disk with the diameter of 100 nm, (b) transmission of In array with different diameter.

We have conducted some preliminary experiment of the plasmonics response of indium. Indium array was successfully fabricated on glass substrate with Au and Cr adhesion layer (figure 7-1a), the transmission (figure 7-1b) shows that the resonance of indium disk is in UV range. We can observe several transmission minimum for each indium array, which may probably arise from the high order mode excitation of indium disk.[237] More simulation should be done to understand the mechanism of UV resonance. In addition, structures with other shape such as squares, wires can be studied to gain the understanding of the UV response of indium. At last, the sensing application can be developed with indium plasmonic materials.

References

1. Barnes, W. L. *et al.* "Surface plasmon subwavelength optics". *Nature* **424**, 824-830,(2003).
2. Knoll, W. "Interfaces and thin films as seen by bound electromagnetic waves". *Annu. Rev. Phys. Chem.* **49**, 569-638,(1998).
3. Brockman, J. M. *et al.* "Surface plasmon resonance imaging measurements of ultrathin organic films". *Annu. Rev. Phys. Chem.* **51**, 41-63,(2000).
4. Kelly, K. L. *et al.* "The optical properties of metal nanoparticles: The influence of size, shape, and dielectric environment". *J. Phys. Chem. B* **107**, 668-677,(2003).
5. Hutter, E.; Fendler, J. H. "Exploitation of localized surface plasmon resonance". *Adv. Mater.* **16**, 1685-1706,(2004).
6. Haes, A. J.; Van Duyne, R. P. "A unified view of propagating and localized surface plasmon resonance biosensors". *Anal. Bioanal. Chem.* **379**, 920-930,(2004).
7. Halas, N. J. "Plasmonics: an emerging field fostered by Nano Letters". *Nano Lett.* **10**, 3816-22,(2010).
8. Oulton, R. F. *et al.* "A hybrid plasmonic waveguide for subwavelength confinement and long-range propagation". *Nat. Photonics* **2**, 496-500,(2008).
9. Stockman, M. I. "Nanofocusing of optical energy in tapered plasmonic waveguides". *Phys. Rev. Lett.* **93**, 137404,(2004).
10. Dai, D.; He, S. "A silicon-based hybrid plasmonic waveguide with a metal cap for a nano-scale light confinement". *Opt. Express* **17**, 16646-16653,(2009).
11. Atwater, H. A. "The promise of plasmonics". *Sci. Am.* **296**, 56-63,(2007).
12. Maier, S. A. "Plasmonics: The promise of highly integrated optical devices". *IEEE J. Sel. Top. Quantum Electron.* **12**, 1671-1677,(2006).
13. Maier, S. A. *et al.* "Plasmonics—a route to nanoscale optical devices". *Adv. Mater.* **13**, 1501-1505,(2001).
14. Ozbay, E. "Plasmonics: merging photonics and electronics at nanoscale dimensions". *Science* **311**, 189-193,(2006).
15. Willets, K. A.; Van Duyne, R. P. "Localized surface plasmon resonance spectroscopy and sensing". *Annu. Rev. Phys. Chem.* **58**, 267-97,(2007).
16. Stewart, M. E. *et al.* "Nanostructured plasmonic sensors". *Chem. Rev.* **108**, 494-521,(2008).
17. Lopatynskyi, A. M. *et al.* "Localized Surface Plasmon Resonance Biosensor-Part I: Theoretical Study of Sensitivity-Extended Mie Approach". *IEEE Sens. J.* **11**, 361-369,(2011).
18. Zhao, J. *et al.* "Localized surface plasmon resonance biosensors". *Nanomedicine-Uk* **1**, 219-228,(2006).
19. Anker, J. N. *et al.* "Biosensing with plasmonic nanosensors". *Nat. Mater.* **7**, 442-453,(2008).
20. Moskovits, M. "Surface-Enhanced Spectroscopy". *Rev. Mod. Phys.* **57**, 783-826,(1985).
21. Tanaka, K. *et al.* "Multifold Enhancement of Quantum Dot Luminescence in Plasmonic Metamaterials". *Phys. Rev. Lett.* **105**,(2010).
22. Bakker, R. M. *et al.* "Enhanced localized fluorescence in plasmonic nanoantennae". *Appl. Phys. Lett.* **92**, 043101,(2008).
23. Lakowicz, J. R. "Plasmonics in biology and plasmon-controlled fluorescence". *Plasmonics* **1**, 5-33,(2006).

24. Dragoman, M.; Dragoman, D. "Plasmonics: Applications to nanoscale terahertz and optical devices". *Prog. Quantum Electron.* **32**, 1-41,(2008).
25. Yu, F. "Surface plasmon fluorescence spectroscopy and surface plasmon diffraction in biomolecular interaction studies". *Max-Planck-Institute für Polymerforschung, Johannes Gutenberg-Universität, Mainz. Doktor der Naturwissenschaft*,(2004).
26. Kneipp, K. *et al. Surface-enhanced Raman scattering: physics and applications*. Springer Science & Business Media: (2006); Vol. 103.
27. Maier, S. A. *Plasmonics: fundamentals and applications: fundamentals and applications*. Springer Science & Business Media: (2007).
28. Bohren, C. F.; Huffman, D. R. *Absorption and scattering of light by small particles*. John Wiley & Sons: (2008).
29. Paul, T. *et al.* "Advanced optical metamaterials". *Adv. Mater.* **22**, 2354-7,(2010).
30. Grzegorczyk, T. M.; Kong, J. A. "Review of left-handed metamaterials: Evolution from theoretical and numerical studies to potential applications". *J. Electromagnet. Wave.* **20**, 2053-2064,(2006).
31. Pendry, J. B. "Negative refraction makes a perfect lens". *Phys. Rev. Lett.* **85**, 3966-3969,(2000).
32. Zhang, S. *et al.* "Experimental demonstration of near-infrared negative-index metamaterials". *Phys. Rev. Lett.* **95**,(2005).
33. Smith, D. R. *et al.* "Metamaterials and negative refractive index". *Science* **305**, 788-792,(2004).
34. Zheludev, N. I. "The Road Ahead for Metamaterials". *Science* **328**, 582-583,(2010).
35. Joannopoulos, J. D. *et al. Photonic crystals: molding the flow of light*. Princeton university press: (2011).
36. Joannopoulos, J. D. *et al.* "Photonic crystals: putting a new twist on light". *Nature* **386**, 143-149,(1997).
37. Noda, S. *et al.* "Full three-dimensional photonic bandgap crystals at near-infrared wavelengths". *Science* **289**, 604-606,(2000).
38. Yablonovitch, E. *et al.* "Photonic Band-Structure - the Face-Centered-Cubic Case Employing Nonspherical Atoms". *Phys. Rev. Lett.* **67**, 2295-2298,(1991).
39. Campbell, M. *et al.* "Fabrication of photonic crystals for the visible spectrum by holographic lithography". *Nature* **404**, 53-56,(2000).
40. Liu, Y.; Zhang, X. "Metamaterials: a new frontier of science and technology". *Chem. Soc. Rev.* **40**, 2494-507,(2011).
41. Lezec, H. J. *et al.* "Negative refraction at visible frequencies". *Science* **316**, 430-432,(2007).
42. Shelby, R. A. *et al.* "Experimental verification of a negative index of refraction". *Science* **292**, 77-79,(2001).
43. Smith, D. R. *et al.* "Metamaterials and negative refractive index". *Science* **305**, 788-792,(2004).
44. Pendry, J. B. *et al.* "Magnetism from conductors and enhanced nonlinear phenomena". *IEEE Trans. Microwave Theory Tech.* **47**, 2075-2084,(1999).
45. Kafesaki, M. *et al.* "Left-handed metamaterials: The fishnet structure and its variations". *Phys. Rev. B* **75**, 235114,(2007).
46. Menzel, C. *et al.* "Validity of effective material parameters for optical fishnet metamaterials". *Phys. Rev. B* **81**, 035320,(2010).
47. Kabashin, A. *et al.* "Plasmonic nanorod metamaterials for biosensing". *Nat. Mater.* **8**, 867-871,(2009).
48. Liu, Q. *et al.* "Self-alignment of plasmonic gold nanorods in reconfigurable anisotropic fluids for

tunable bulk metamaterial applications". *Nano Lett.* **10**, 1347-1353,(2010).

49. Linden, S. *et al.* "Magnetic response of metamaterials at 100 terahertz". *Science* **306**, 1351-1353,(2004).
50. Schurig, D. *et al.* "Metamaterial electromagnetic cloak at microwave frequencies". *Science* **314**, 977-980,(2006).
51. Xu, X. L. *et al.* "Flexible Visible-Infrared Metamaterials and Their Applications in Highly Sensitive Chemical and Biological Sensing". *Nano Lett.* **11**, 3232-3238,(2011).
52. Enkrich, C. *et al.* "Magnetic metamaterials at telecommunication and visible frequencies". *Phys. Rev. Lett.* **95**, 203901,(2005).
53. Burgos, S. P. *et al.* "A single-layer wide-angle negative-index metamaterial at visible frequencies". *Nat. Mater.* **9**, 407-412,(2010).
54. Zhang, S. *et al.* "Near-infrared double negative metamaterials". *Opt. Express* **13**, 4922-4930,(2005).
55. Tobing, L. Y. M. *et al.* "Sub-100-nm Sized Silver Split Ring Resonator Metamaterials with Fundamental Magnetic Resonance in the Middle Visible Spectrum". *Adv. Opt. Mater.* **2**, 280-285,(2014).
56. Liu, N. *et al.* "Three-dimensional photonic metamaterials at optical frequencies". *Nat. Mater.* **7**, 31-37,(2008).
57. Chanda, D. *et al.* "Large-area flexible 3D optical negative index metamaterial formed by nanotransfer printing". *Nat. Nanotechnol.* **6**, 402-407,(2011).
58. Yu, N.; Capasso, F. "Flat optics with designer metasurfaces". *Nat. Mater.* **13**, 139-150,(2014).
59. Falcone, F. *et al.* "Babinet principle applied to the design of metasurfaces and metamaterials". *Phys. Rev. Lett.* **93**, 197401,(2004).
60. Zhao, Y.; Alu, A. "Manipulating light polarization with ultrathin plasmonic metasurfaces". *Phys. Rev. B* **84**, 205428,(2011).
61. Auguie, B.; Barnes, W. L. "Collective resonances in gold nanoparticle arrays". *Phys. Rev. Lett.* **101**,(2008).
62. Chu, Y. Z. *et al.* "Experimental observation of narrow surface plasmon resonances in gold nanoparticle arrays". *Appl. Phys. Lett.* **93**,(2008).
63. Kravets, V. G. *et al.* "Extremely narrow plasmon resonances based on diffraction coupling of localized plasmons in arrays of metallic nanoparticles". *Phys. Rev. Lett.* **101**,(2008).
64. Schokker, A. H.; Koenderink, A. F. "Lasing at the band edges of plasmonic lattices". *Phys. Rev. B* **90**,(2014).
65. Yu, N. F. *et al.* "Light Propagation with Phase Discontinuities: Generalized Laws of Reflection and Refraction". *Science* **334**, 333-337,(2011).
66. Huang, L. L. *et al.* "Dispersionless Phase Discontinuities for Controlling Light Propagation". *Nano Lett.* **12**, 5750-5755,(2012).
67. Liu, N.; Giessen, H. "Coupling effects in optical metamaterials". *Angew. Chem. Int. Ed.* **49**, 9838-52,(2010).
68. Rayleigh. "On the scattering of light by a cloud of similar small particles of any shape and oriented at random.". *Philos. Mag.* **35**, 373-381,(1918).
69. Young, A. T. "Rayleigh-Scattering". *Appl. Opt.* **20**, 533-535,(1981).
70. Placzek, G. *The Rayleigh and Raman Scattering*. Lawrence Radiation Laboratory: (1959); Vol. 526.
71. Raman, C. V.; Krishnan, K. S. "A new type of secondary radiation". *Nature* **121**, 501-502,(1928).

72. Singh, R. "C. V. Raman and the discovery of the Raman effect". *Phys Perspect* **4**, 399-420,(2002).
73. Pringsheim, P. "The Raman effect, a new radiation effect developed by C.V. Raman.". *Naturwiss.* **16**, 597-606,(1928).
74. Ruf, T. *et al.* "Resonant Magneto-Raman Scattering in Gaas". *Phys. Rev. B* **41**, 3039-3047,(1990).
75. Parker, J. C. "Raman-Scattering from Vo2 Single-Crystals - a Study of the Effects of Surface Oxidation". *Phys. Rev. B* **42**, 3164-3166,(1990).
76. Ciepielewski, P. *et al.* "Raman-Scattering in Cdf2-in Crystals". *Phys. Rev. B* **42**, 11665-11669,(1990).
77. Sobocinski, R. L. *et al.* "Surface Raman-Scattering of Methanol, 1-Propanol, 1-Pentanol, and 1-Butanethiol on Insitu and Emersed Silver Electrodes". *J. Am. Chem. Soc.* **112**, 6177-6183,(1990).
78. Pan, J. H. *et al.* "Raman-Scattering of Cds Microcrystals in Organic Media". *J. Lumin.* **45**, 45-47,(1990).
79. Landsberg, G.; Mandelstam, L. "A new occurrence in the light diffusion of crystals.". *Naturwiss.* **16**, 557-558,(1928).
80. Schlucker, S. "SERS microscopy: nanoparticle probes and biomedical applications". *Chemphyschem* **10**, 1344-54,(2009).
81. Graham, D. *et al.* "Control of enhanced Raman scattering using a DNA-based assembly process of dye-coded nanoparticles". *Nat. Nanotechnol.* **3**, 548-551,(2008).
82. Kneipp, K. *et al.* "Single molecule detection using surface-enhanced Raman scattering (SERS)". *Phys. Rev. Lett.* **78**, 1667-1670,(1997).
83. Nie, S. M.; Emery, S. R. "Probing single molecules and single nanoparticles by surface-enhanced Raman scattering". *Science* **275**, 1102-1106,(1997).
84. Fleischm.M *et al.* "Raman-Spectra of Pyridine Adsorbed at a Silver Electrode". *Chem. Phys. Lett.* **26**, 163-166,(1974).
85. Jeanmaire, D. L.; Vanduyne, R. P. "Surface Raman Spectroelectrochemistry .1. Heterocyclic, Aromatic, and Aliphatic-Amines Adsorbed on Anodized Silver Electrode". *J. Electroanal. Chem.* **84**, 1-20,(1977).
86. Moskovits, M. "Surface-Roughness and Enhanced Intensity of Raman-Scattering by Molecules Adsorbed on Metals". *J. Chem. Phys.* **69**, 4159-4161,(1978).
87. You, H. *et al.* "Interface synthesis of gold mesocrystals with highly roughened surfaces for surface-enhanced Raman spectroscopy". *J. Mater. Chem.* **22**, 1998,(2012).
88. Hu, M. *et al.* "Gold Nanofingers for Molecule Trapping and Detection". *J. Am. Chem. Soc.* **132**, 12820-12822,(2010).
89. Yoon, I. *et al.* "Single Nanowire on a Film as an Efficient SERS-Active Platform". *J. Am. Chem. Soc.* **131**, 758-762,(2009).
90. Fang, J. X. *et al.* "Gold Mesostructures with Tailored Surface Topography and Their Self-Assembly Arrays for Surface-Enhanced Raman Spectroscopy". *Nano Lett.* **10**, 5006-5013,(2010).
91. Li, L. *et al.* "Metal oxide nanoparticle mediated enhanced Raman scattering and its use in direct monitoring of interfacial chemical reactions". *Nano Lett.* **12**, 4242-6,(2012).
92. Li, J. F. *et al.* "Shell-isolated nanoparticle-enhanced Raman spectroscopy". *Nature* **464**, 392-395,(2010).
93. Mccall, S. L.; Platzman, P. M. "Raman-Scattering from Chemisorbed Molecules at Surfaces". *Phys. Rev. B* **22**, 1660-1662,(1980).
94. Mccall, S. L. *et al.* "Surface Enhanced Raman-Scattering". *Phys. Lett. A* **77**, 381-383,(1980).

95. Kerker, M. *et al.* "Surface Enhanced Raman-Scattering (Sers) by Molecules Adsorbed at Spherical-Particles". *Appl. Opt.* **19**, 4159-4174,(1980).
96. Kerker, M. "Resonances in Electromagnetic Scattering by Objects with Negative Absorption". *Appl. Opt.* **18**, 1180-1189,(1979).
97. Kerker, M. *et al.* "Effect of Aggregates on Extinction and Surface-Enhanced Raman-Scattering Spectra of Colloidal Silver". *J. Phys. Chem.* **88**, 3168-3170,(1984).
98. Stockman, M. I. "Inhomogeneous eigenmode localization, chaos, and correlations in large disordered clusters". *Phys. Rev. E* **56**, 6494-6507,(1997).
99. Gresillon, S. *et al.* "Experimental observation of localized optical excitations in random metal-dielectric films". *Phys. Rev. Lett.* **82**, 4520-4523,(1999).
100. Billot, L. *et al.* "Surface enhanced Raman scattering on gold nanowire arrays: Evidence of strong multipolar surface plasmon resonance enhancement". *Chem. Phys. Lett.* **422**, 303-307,(2006).
101. Gersten, J.; Nitzan, A. "Electromagnetic Theory of Enhanced Raman-Scattering by Molecules Adsorbed on Rough Surfaces". *J. Chem. Phys.* **73**, 3023-3037,(1980).
102. Liao, P. F.; Wokaun, A. "Lightning Rod Effect in Surface Enhanced Raman-Scattering". *J. Chem. Phys.* **76**, 751-752,(1982).
103. Lombardi, J. R. *et al.* "Charge-Transfer Theory of Surface Enhanced Raman-Spectroscopy - Herzberg-Teller Contributions". *J. Chem. Phys.* **84**, 4174-4180,(1986).
104. Lombardi, J. R.; Birke, R. L. "A unified approach to surface-enhanced Raman spectroscopy". *J. Phys. Chem. C* **112**, 5605-5617,(2008).
105. Prodan, E. *et al.* "A hybridization model for the plasmon response of complex nanostructures". *Science* **302**, 419-422,(2003).
106. Xu, H. X. *et al.* "Spectroscopy of single hemoglobin molecules by surface enhanced Raman scattering". *Phys. Rev. Lett.* **83**, 4357-4360,(1999).
107. Ciraci, C. *et al.* "Probing the ultimate limits of plasmonic enhancement". *Science* **337**, 1072-4,(2012).
108. Stockle, R. M. *et al.* "Nanoscale chemical analysis by tip-enhanced Raman spectroscopy". *Chem. Phys. Lett.* **318**, 131-136,(2000).
109. Zhang, R. *et al.* "Chemical mapping of a single molecule by plasmon-enhanced Raman scattering". *Nature* **498**, 82-86,(2013).
110. Maidecchi, G. *et al.* "Deep Ultraviolet Plasmon Resonance in Aluminum Nanoparticle Arrays". *Acs Nano* **7**, 5834-5841,(2013).
111. Kumamoto, Y. *et al.* "Indium for Deep-Ultraviolet Surface-Enhanced Resonance Raman Scattering". *Acs Photonics* **1**, 598-603,(2014).
112. Vieu, C. *et al.* "Electron beam lithography: resolution limits and applications". *Appl. Surf. Sci.* **164**, 111-117,(2000).
113. Escovitz, W. *et al.* "Scanning transmission ion microscope with a field ion source". *PNAS* **72**, 1826-1828,(1975).
114. Wong, A. K.-K. *Resolution enhancement techniques in optical lithography*. SPIE press: (2001); Vol. 47.
115. Smith, H. I.; Craighead, H. G. "Nanofabrication". *Phys. Today* **43**, 24-30,(2008).
116. Melngailis, J. *et al.* "Instrumentation for Conformable Photomask Lithography". *IEEE Trans. Electron Devices* **Ed22**, 496-498,(1975).
117. Lasagni, A. *et al.* "Periodic pattern formation of intermetallic phases with long range order by

laser interference metallurgy". *Adv. Eng. Mater.* **7**, 487-492,(2005).

118. Haynes, C. L.; Van Duyne, R. P. "Nanosphere lithography: A versatile nanofabrication tool for studies of size-dependent nanoparticle optics". *J. Phys. Chem. B* **105**, 5599-5611,(2001).
119. Hulteen, J. C.; Vanduyne, R. P. "Nanosphere Lithography - a Materials General Fabrication Process for Periodic Particle Array Surfaces". *J. Vac. Sci. Technol., A* **13**, 1553-1558,(1995).
120. Chen, Y.; Pepin, A. "Nanofabrication: Conventional and nonconventional methods". *Electrophoresis* **22**, 187-207,(2001).
121. Tseng, A. A. *Nanofabrication: fundamentals and applications*. World Scientific Singapore: (2008).
122. Pfeiffer, H. C. "Variable Spot Shaping for Electron-Beam Lithography". *J. Vac. Sci. Technol.* **15**, 887-890,(1978).
123. Yamazaki, K.; Namatsu, H. "5-nm-order electron-beam lithography for nanodevice fabrication". *Japanese Journal of Applied Physics Part 1-Regular Papers Brief Communications & Review Papers* **43**, 3767-3771,(2004).
124. Chang, T. "Proximity effect in electron ‐ beam lithography". *J. Vac. Sci. Technol.* **12**, 1271-1275,(1975).
125. Parikh, M. "Corrections to proximity effects in electron beam lithography. I. Theory". *J. Appl. Phys.* **50**, 4371-4377,(1979).
126. Owen, G.; Rissman, P. "Proximity effect correction for electron beam lithography by equalization of background dose". *J. Appl. Phys.* **54**, 3573-3581,(1983).
127. Parikh, M. "Self-Consistent Proximity Effect Correction Technique for Resist Exposure (Specter)". *J. Vac. Sci. Technol.* **15**, 931-933,(1978).
128. Owen, G.; Rissman, P. "Proximity Effect Correction for Electron-Beam Lithography by Equalization of Background Dose". *J. Appl. Phys.* **54**, 3573-3581,(1983).
129. Cumming, D. R. S. *et al.* "Fabrication of 3 nm wires using 100 keV electron beam lithography and poly(methyl methacrylate) resist". *Appl. Phys. Lett.* **68**, 322-324,(1996).
130. Namatsu, H. *et al.* "Nano-patterning of a hydrogen silsesquioxane resist with reduced linewidth fluctuations". *Microelectron. Eng.* **41**, 331-334,(1998).
131. Faraday, M. "The Bakerian lecture: experimental relations of gold (and other metals) to light". *Philos. Trans. R. Soc. London* **147**, 145-181,(1857).
132. Kundt, A. "Über die Brechungsexponenten der Metalle (About refractive indices of metals)". *Ann Physik* **34**, 469-489,(1888).
133. Maissel, L. I.; Glang, R. "Handbook of thin film technology".(1995).
134. www.micromagnetics.com.
135. Fan, Z. *et al.* "Three-dimensional nanopillar-array photovoltaics on low-cost and flexible substrates". *Nat. Mater.* **8**, 648-653,(2009).
136. Gelinck, G. H. *et al.* "Flexible active-matrix displays and shift registers based on solution-processed organic transistors". *Nat. Mater.* **3**, 106-110,(2004).
137. McAlpine, M. C. *et al.* "Highly ordered nanowire arrays on plastic substrates for ultrasensitive flexible chemical sensors". *Nat. Mater.* **6**, 379-384,(2007).
138. Takei, K. *et al.* "Nanowire active-matrix circuitry for low-voltage macroscale artificial skin". *Nat. Mater.* **9**, 821-826,(2010).
139. Han, N. R. *et al.* "Broadband multi-layer terahertz metamaterials fabrication and characterization on flexible substrates". *Opt. Express* **19**, 6990-6998,(2011).
140. Pryce, I. M. *et al.* "Compliant Metamaterials for Resonantly Enhanced Infrared Absorption

Spectroscopy and Refractive Index Sensing". *ACS Nano* **5**, 8167-8174,(2011).

141. Pryce, I. M. *et al.* "Highly Strained Compliant Optical Metamaterials with Large Frequency Tunability". *Nano Lett.* **10**, 4222-4227,(2010).
142. Tao, H. *et al.* "Silk‐Based Conformal, Adhesive, Edible Food Sensors". *Adv. Mater.* **24**, 1067-1072,(2012).
143. Tao, H. *et al.* "Terahertz metamaterials on free-standing highly-flexible polyimide substrates". *J. Phys. D Appl. Phys.* **41**, 232004,(2008).
144. Fan, Z. *et al.* "Toward the Development of Printable Nanowire Electronics and Sensors". *Adv. Mater.* **21**, 3730-3743,(2009).
145. Luo, C. *et al.* "Releasing SU-8 structures using polystyrene as a sacrificial material". *Sens. Actuators, A* **114**, 123-128,(2004).
146. Kersey, L. *et al.* "The effect of adhesion promoter on the adhesion of PDMS to different substrate materials". *Lab Chip* **9**, 1002-1004,(2009).
147. Lee, C. H. *et al.* "Fabrication of Nanowire Electronics on Nonconventional Substrates by Water-Assisted Transfer Printing Method". *Nano Lett.* **11**, 3435-3439,(2011).
148. O'Hara, J. F. *et al.* "Thin-film sensing with planar terahertz metamaterials: sensitivity and limitations". *Opt. Express* **16**, 1786-1795,(2008).
149. Driscoll, T. *et al.* "Tuned permeability in terahertz split-ring resonators for devices and sensors". *Appl. Phys. Lett.* **91**,(2007).
150. Kennedy, B. J. *et al.* "Determination of the distance dependence and experimental effects for modified SERS substrates based on self-assembled monolayers formed using alkanethiols". *J. Phys. Chem. B* **103**, 3640-3646,(1999).
151. Park, S. *et al.* "Transition metal-coated nanoparticle films: vibrational characterization with surface-enhanced Raman scattering". *J. Am. Chem. Soc.* **124**, 2428-2429,(2002).
152. Tian, Z. Q. *et al.* "Surface-enhanced Raman scattering from transition metals with special surface morphology and nanoparticle shape". *Faraday Discuss.* **132**, 159-170,(2006).
153. Lu, G. *et al.* "Nanoparticle-coated PDMS elastomers for enhancement of Raman scattering". *Chem. Commun.* **47**, 8560-8562,(2011).
154. Alvarez-Puebla, R. *et al.* "Surface-enhanced Raman scattering for ultrasensitive chemical analysis of 1 and 2-naphthalenethiols". *Analyst* **129**, 1251-1256,(2004).
155. Bae, S. C. *et al.* "Chemical imaging in a surface forces apparatus: confocal Raman spectroscopy of confined poly (dimethylsiloxane)". *Langmuir* **21**, 5685-5688,(2005).
156. Leveque, G.; Martin, O. J. F. "Optical interactions in a plasmonic particle coupled to a metallic film". *Opt. Express* **14**, 9971-9981,(2006).
157. Mock, J. J. *et al.* "Distance-dependent plasmon resonant coupling between a gold nanoparticle and gold film". *Nano Lett.* **8**, 2245-2252,(2008).
158. Fu, Y. H. *et al.* "A Micromachined Reconfigurable Metamaterial via Reconfiguration of Asymmetric Split-Ring Resonators". *Adv. Funct. Mater.* **21**, 3589-3594,(2011).
159. Tao, H. *et al.* "Reconfigurable Terahertz Metamaterials". *Phys. Rev. Lett.* **103**,(2009).
160. Chen, H. T. *et al.* "Active terahertz metamaterial devices". *Nature* **444**, 597-600,(2006).
161. Chen, H. T. *et al.* "Experimental demonstration of frequency-agile terahertz metamaterials". *Nat. Photonics* **2**, 295-298,(2008).
162. Gholipour, B. *et al.* "An all-optical, non-volatile, bidirectional, phase-change meta-switch". *Adv. Mater.* **25**, 3050-4,(2013).

163. Driscoll, T. *et al.* "Memory metamaterials". *Science* **325**, 1518-21,(2009).
164. Eyert, V. "The metal-insulator transitions of VO2: a band theoretical approach". *Ann. Phys.* **11**, 650-702,(2002).
165. Zylbersztejn, A.; Mott, N. F. "Metal-Insulator Transition in Vanadium Dioxide". *Phys. Rev. B* **11**, 4383-4395,(1975).
166. Biermann, S. *et al.* "Dynamical singlets and correlation-assisted peierls transition in VO2". *Phys. Rev. Lett.* **94**,(2005).
167. Wentzcovitch, R. M. *et al.* "Vo2 - Peierls or Mott-Hubbard - a View from Band Theory". *Phys. Rev. Lett.* **72**, 3389-3392,(1994).
168. Qazilbash, M. M. *et al.* "Mott transition in VO2 revealed by infrared spectroscopy and nano-imaging". *Science* **318**, 1750-3,(2007).
169. Chain, E. E. "Optical-Properties of Vanadium Dioxide and Vanadium Pentoxide Thin-Films". *Appl. Opt.* **30**, 2782-2787,(1991).
170. Appavoo, K.; Haglund, R. F. "Detecting nanoscale size dependence in VO2 phase transition using a split-ring resonator metamaterial". *Nano Lett.* **11**, 1025-31,(2011).
171. Griffith.Ch; Eastwood, H. K. "Influence of Stoichiometry on Metal-Semiconductor Transition in Vanadium Dioxide". *J. Appl. Phys.* **45**, 2201-2206,(1974).
172. Nag, J.; Haglund, R. F. "Synthesis of vanadium dioxide thin films and nanoparticles". *J. Phys.: Condens. Matter* **20**,(2008).
173. Koide, S.; Takei, H. "Epitaxial Growth of Vo2 Single Crystals and Their Anisotropic Properties in Electrical Resistivities". *J. Phys. Soc. Jpn.* **22**, 946-&,(1967).
174. Ryabova, L. A. *et al.* "Preparation and Properties of Pyrolysis of Vanadium Oxide-Films". *J. Electrochem. Soc.* **119**, 427-&,(1972).
175. Eason, R. *Pulsed laser deposition of thin films: applications-led growth of functional materials*. John Wiley & Sons: (2007).
176. Greenberg, C. B. "Undoped and Doped Vo2 Films Grown from Vo(Oc3h7)3". *Thin Solid Films* **110**, 73-82,(1983).
177. Chain, E. E. "Effects of Oxygen in Ion-Beam Sputter Deposition of Vanadium-Oxide". *J. Vac. Sci. Technol., A* **5**, 1836-1839,(1987).
178. Chain, E. E. "The Influence of Deposition Temperature on the Structure and Optical-Properties of Vanadium-Oxide Films". *J. Vac. Sci. Technol., A* **4**, 432-435,(1986).
179. Schilbe, P. "Raman scattering in VO2". *Physica B* **316**, 600-602,(2002).
180. Petrov, G. I. *et al.* "Raman microscopy analysis of phase transformation mechanisms in vanadium dioxide". *Appl. Phys. Lett.* **81**, 1023,(2002).
181. Kana Kana, J. B. *et al.* "Thermally tunable optical constants of vanadium dioxide thin films measured by spectroscopic ellipsometry". *Opt. Commun.* **284**, 807-812,(2011).
182. Liu, M. *et al.* "Terahertz-field-induced insulator-to-metal transition in vanadium dioxide metamaterial". *Nature* **487**, 345-8,(2012).
183. Guo, H. *et al.* "Thickness dependence of the optical properties of split-ring resonator metamaterials". *physica status solidi (b)* **244**, 1256-1261,(2007).
184. Enkrich, C. *et al.* "Magnetic metamaterials at telecommunication and visible frequencies". *Phys. Rev. Lett.* **95**,(2005).
185. Haes, A. J. *et al.* "Nanoscale optical biosensor: Short range distance dependence of the localized surface plasmon resonance of noble metal nanoparticles". *J. Phys. Chem. B* **108**,

6961-6968,(2004).
186. Ingber, D. E. "Cellular mechanotransduction: putting all the pieces together again". *Faseb J.* **20**, 811-827,(2006).
187. Shen, Y. *et al.* "Plasmonic gold mushroom arrays with refractive index sensing figures of merit approaching the theoretical limit". *Nat. Commun.* **4**,(2013).
188. Beutler, H. "Über Absorptionsserien von Argon, Krypton und Xenon zu Termen zwischen den beiden Ionisierungsgrenzen2 P 3 2/0 und2 P 1 2/0". *Z. Angew. Phys.* **93**, 177-196,(1935).
189. Fano, U. "Sullo spettro di assorbimento dei gas nobili presso il limite dello spettro d'arco". *Il Nuovo Cimento* **12**, 154-161,(1935).
190. Miroshnichenko, A. E. *et al.* "Fano resonances in nanoscale structures". *Rev. Mod. Phys.* **82**, 2257-2298,(2010).
191. Luo, H. G. *et al.* "Fano resonance for Anderson impurity systems". *Phys. Rev. Lett.* **92**,(2004).
192. Tribelsky, M. I. *et al.* "Light scattering by a finite obstacle and fano resonances". *Phys. Rev. Lett.* **100**,(2008).
193. Christ, A. *et al.* "Optical properties of planar metallic photonic crystal structures: Experiment and theory". *Phys. Rev. B* **70**,(2004).
194. Hessel, A.; Oliner, A. A. "A New Theory of Woods Anomalies on Optical Gratings". *Appl. Opt.* **4**, 1275-&,(1965).
195. Halas, N. J. *et al.* "Plasmons in strongly coupled metallic nanostructures". *Chem. Rev.* **111**, 3913-61,(2011).
196. Verellen, N. *et al.* "Fano Resonances in Individual Coherent Plasmonic Nanocavities". *Nano Lett.* **9**, 1663-1667,(2009).
197. Liu, S. D. *et al.* "Multiple Fano Resonances in Plasmonic Heptamer Clusters Composed of Split Nanorings". *Acs Nano* **6**, 6260-6271,(2012).
198. Hao, F. *et al.* "Symmetry Breaking in Plasmonic Nanocavities: Subradiant LSPR Sensing and a Tunable Fano Resonance". *Nano Lett.* **8**, 3983-3988,(2008).
199. Fan, J. A. *et al.* "Self-Assembled Plasmonic Nanoparticle Clusters". *Science* **328**, 1135-1138,(2010).
200. Sheikholeslami, S. N. *et al.* "Controlling the interplay of electric and magnetic modes via Fano-like plasmon resonances". *Nano Lett.* **11**, 3927-34,(2011).
201. Shafiei, F. *et al.* "A subwavelength plasmonic metamolecule exhibiting magnetic-based optical Fano resonance". *Nat. Nanotechnol.* **8**, 95-99,(2013).
202. Nordlander, P. "Plasmonics: The dark side of the ring". *Nat. Nanotechnol.* **8**, 76-7,(2013).
203. Alù, A.; Engheta, N. "Dynamical theory of artificial optical magnetism produced by rings of plasmonic nanoparticles". *Phys. Rev. B* **78**,(2008).
204. Sonnefraud, Y. *et al.* "Experimental Realization of Subradiant, Superradiant, and Fano Resonances in Ring/Disk Plasmonic Nanocavities". *Acs Nano* **4**, 1664-1670,(2010).
205. Johnson, P. B.; Christy, R.-W. "Optical constants of the noble metals". *Phys. Rev. B* **6**, 4370,(1972).
206. Liu, S. D. *et al.* "Plasmonic-induced optical transparency in the near-infrared and visible range with double split nanoring cavity". *Opt. Express* **19**, 15363-15370,(2011).
207. Chen, H. *et al.* "Observation of the Fano resonance in gold nanorods supported on high-dielectric-constant substrates". *Acs Nano* **5**, 6754-6763,(2011).
208. Zhao, J. *et al.* "Large-Area Low-Cost Plasmonic Nanostructures in the NIR for Fano Resonant Sensing". *Adv. Mater.* **24**, Op247-Op252,(2012).
209. Lassiter, J. B. *et al.* "Fano Resonances in Plasmonic Nanoclusters: Geometrical and Chemical

Tunability". *Nano Lett.* **10**, 3184-3189,(2010).

210. Landy, N. *et al.* "Perfect Metamaterial Absorber". *Phys. Rev. Lett.* **100**,(2008).
211. Liu, N. *et al.* "Infrared perfect absorber and its application as plasmonic sensor". *Nano Lett.* **10**, 2342-8,(2010).
212. Moreau, A. *et al.* "Controlled-reflectance surfaces with film-coupled colloidal nanoantennas". *Nature* **492**, 86-9,(2012).
213. Aydin, K. *et al.* "Broadband polarization-independent resonant light absorption using ultrathin plasmonic super absorbers". *Nat. Commun.* **2**, 517,(2011).
214. Hedayati, M. K. *et al.* "Design of a perfect black absorber at visible frequencies using plasmonic metamaterials". *Adv. Mater.* **23**, 5410-4,(2011).
215. Tao, H. *et al.* "A metamaterial absorber for the terahertz regime: Design, fabrication and characterization". *Opt. Express* **16**, 7181-7188,(2008).
216. Kats, M. A. *et al.* "Ultra-thin perfect absorber employing a tunable phase change material". *Appl. Phys. Lett.* **101**,(2012).
217. Kats, M. A. *et al.* "Nanometre optical coatings based on strong interference effects in highly absorbing media". *Nat. Mater.* **12**, 20-24,(2013).
218. Kim, J. Y. *et al.* "New architecture for high-efficiency polymer photovoltaic cells using solution-based titanium oxide as an optical spacer". *Adv. Mater.* **18**, 572-+,(2006).
219. Mann, S. A.; Garnett, E. C. "Extreme Light Absorption in Thin Semiconductor Films Wrapped around Metal Nanowires". *Nano Lett.* **13**, 3173-3178,(2013).
220. Dotan, H. *et al.* "Resonant light trapping in ultrathin films for water splitting". *Nat. Mater.* **12**, 158-164,(2013).
221. Wuttig, M.; Yamada, N. "Phase-change materials for rewriteable data storage". *Nat. Mater.* **6**, 824-832,(2007).
222. Friedrich, I. *et al.* "Structural transformations of Ge[sub 2]Sb[sub 2]Te[sub 5] films studied by electrical resistance measurements". *J. Appl. Phys.* **87**, 4130,(2000).
223. Forst, M. *et al.* "Phase change in Ge 2 Sb 2 Te 5 films investigated by coherent phonon spectroscopy". *Appl. Phys. Lett.* **77**, 1964-1966,(2000).
224. Shportko, K. *et al.* "Resonant bonding in crystalline phase-change materials". *Nat Mater* **7**, 653-8,(2008).
225. Cao, T. *et al.* "Broadband polarization-independent perfect absorber using a phase-change metamaterial at visible frequencies". *Sci. Rep.* **4**, 3955,(2014).
226. Hosseini, P. *et al.* "An optoelectronic framework enabled by low-dimensional phase-change films". *Nature* **511**, 206-11,(2014).
227. Tsafack, T. *et al.* "Electronic, optical and thermal properties of the hexagonal and rocksalt-like Ge2Sb2Te5 chalcogenide from first-principle calculations". *J. Appl. Phys.* **110**, 063716,(2011).
228. Zhang, Q. *et al.* "Multiple Magnetic Mode-Based Fano Resonance in Split-Ring Resonator/Disk Nanocavities". *ACS Nano* **7**, 11071-11078,(2013).
229. Zhang, Q. *et al.* "Scattering focusing and localized surface plasmons in a single Ag nanoring". *Appl. Phys. Lett.* **97**,(2010).
230. Zhang, Q. *et al.* "Modulating Resonance Modes and Q Value of a CdS Nanowire Cavity by Single Ag Nanoparticles". *Nano Lett.* **11**, 4270-4274,(2011).
231. Wen, X. L. *et al.* "Transparent free-standing metamaterials and their applications in surface-enhanced Raman scattering". *Nanoscale* **6**, 132-139,(2014).

232. Wen, X. L. *et al.* "Near-infrared active metamaterials and their applications in tunable surface-enhanced Raman scattering". *Opt. Express* **22**, 2989-2995,(2014).
233. Hein, S. M.; Giessen, H. "Tailoring Magnetic Dipole Emission with Plasmonic Split-Ring Resonators". *Phys. Rev. Lett.* **111**,(2013).
234. Knight, M. W. *et al.* "Aluminum for plasmonics". *ACS nano* **8**, 834-840,(2013).
235. Knight, M. W. *et al.* "Aluminum plasmonic nanoantennas". *Nano Lett.* **12**, 6000-6004,(2012).
236. Sanz, J. *et al.* "Uv plasmonic behavior of various metal nanoparticles in the near-and far-field regimes: Geometry and substrate effects". *J. Phys. Chem. C* **117**, 19606-19615,(2013).
237. McMahon, J. M. *et al.* "Plasmonics in the ultraviolet with the poor metals Al, Ga, In, Sn, Tl, Pb, and Bi". *Phys. Chem. Chem. Phys.* **15**, 5415-5423,(2013).

Publication List

1. **X. L. Wen**, G. Y. Li, J. Zhang, Q. Zhang, B. Peng, L. M. Wong, S. J. Wang, and Q. H. Xiong, "Transparent free-standing metamaterials and their applications in surface-enhanced Raman scattering," ***Nanoscale*** **6**, 132-139 (2014).

2. Q. Zhang, **X. L. Wen**, G. Y. Li, Q. F. Ruan, J. F. Wang, and Q. H. Xiong, "Multiple Magnetic Mode-Based Fano Resonance in Split-Ring Resonator/Disk Nanocavities," ***ACS Nano*** **7**, 11071-11078 (2013). (co-first author)

3. **X. L. Wen**, Q. Zhang, J. W. Chai, L. M. Wong, S. J. Wang, and Q. H. Xiong, "Near-infrared active metamaterials and their applications in tunable surface-enhanced Raman scattering," ***Opt. Express*** **22**, 2989-2995 (2014).

4. C. Cao, J. Zhang, **X. L. Wen**, S. L. Dodson, N. T. Dao, L. M. Wong, S. J. Wang, S. Z. Li, A. T. Phan, and Q. H. Xiong, "Metamaterials-Based Label-Free Nanosensor for Conformation and Affinity Biosensing," ***ACS Nano*** **7**, 7583-7591 (2013).

5. Y. Y. Zhao, M. de la Mata, R. L. J. Qiu, J. Zhang, **X. L. Wen**, C. Magen, X. P. A. Gao, J. Arbiol, and Q. H. Xiong, "Te-seeded growth of few-quintuple layer Bi_2Te_3 nanoplates," ***Nano Res.*** **7**, 1243-1253 (2014).

6. X. F. Liu, Q. Zhang, W. K. Chong, J. N. Yip, **X. L. Wen**, Z. P. Li, F. X. Wei, G. N. Yu, Q. H. Xiong, and T. C. Sum, "Cooperative Enhancement of Second-Harmonic Generation from a Single CdS Nanobelt-Hybrid Plasmonic Structure," ***ACS Nano*** **9**, 5018-5026 (2015).

7. L. L. Zhang, Y. W. Yuan, **X. L. Wen**, Y. Li, C. Cao, and Q. H. Xiong, "A coordination and ligand replacement based three-input colorimetric logic gate sensing platform for melamine, mercury ions, and cysteine," ***RSC Adv.*** **5**, 59106-59113 (2015).

8. **X. L. Wen** and Q. H. Xiong, "A visible-near infrared perfect absorber based on a phase change material ($Ge_2Sb_2Te_5$) thin film," ***Submitted***